A structural and biochemical comparison of wild-type and recombinant propanediol utilising bacterial microcompartments

A thesis submitted to the University of Kent for the degree of Ph.D. in the Faculty of Sciences.

2015

by

Matthias J. Mayer, MSc

Declaration

Name: Matthias J. Mayer, MSc

Degree: PhD-Biochemistry

Title: A structural and biochemical comparison of wild type and recombinant propanediol utilising bacterial microcompartments

No part of this thesis has been submitted in support of an application for any degree or other qualification of the University of Kent, or any other University or Institution of learning.

Abstract

Bacterial microcompartments (BMCs) likely represent the largest protein complex found in bacterial cells (estimated 18,000 subunits). BMCs are associated with specific metabolic processes such as carbon fixation in the case of carboxysomes or carbon utilisation in the case of the 1,2-propanediol utilisation metabolosome. With all BMCs there is still much to learn about the structure and function of these supramolecular assemblies.

In this project the structure and function of the Pdu BMC has been studied through a combination of recombinant DNA technology, proteomics, fluorescence microscopy, transmission electron microscopy (TEM) and atomic force microscopy (AFM). Initially, wild type *Citrobacter freundii* (*C. freundii*) Pdu BMCs were compared to recombinant BMCs that had been produced in *Escherichia coli* (*E. coli*). These were found to have very similar profiles in terms of BMC shell composition, size (120-130 nm on average) and shape. However, recombinant empty BMCs (eBMCs), generated by the coexpression of the genes for just the shell proteins, were found to be distinctly different in that they incorporated more of the first shell protein of the operon, PduA, and were also significantly smaller (55-80 nm on average) than the complete BMCs. This work provides the first recorded application of AFM for the study of BMCs and revealed that the eBMCs were stiffer and less flexible than complete BMCs and it is unclear if differences in shell protein composition or the lack of the internal scaffold is causing the reported biophysical differences.

One key property of the BMCs is their ability to absorb substrate and cofactor molecules to allow the internalised metabolic pathway to operate. Adenosylcobalamin (Ado-B_{12}) is required as a coenzyme for the diol dehydratase conversion of 1,2-propanediol (1,2-PD), but the uptake of cobalamin into the BMC was not shown. By feeding cells exogenous cobalamin, it was possible to demonstrate that cobalamin is specifically partitioned from the cytoplasm into the BMC. Moreover the synthesis of fluorescently labelled versions of cobalamin allowed this partitioning to be followed *ex-vivo* with purified BMCs.

Publications

Moore, Simon J., **Matthias J. Mayer**, Rebekka Biedendieck, Evelyne Deery, and Martin J. Warren. "Towards a cell factory for vitamin B_{12} production in *Bacillus megaterium*: by passing of the cobalamin riboswitch control elements."*New biotechnology* 31, no. 6 (2014): 553-561.

Acknowledgments

This thesis is dedicated to Mag. Frieda Moser, who encouraged me to not study Biology.

First of all I want to thank my supervisors Prof. Martin Warren and Prof. Mark Smales. They allowed this thesis to be my own work but guided me in the right direction, when needed.

Thanks to Florian Widner for telling me about the position at UKC and countless hours of running or drinking “Schnaps”. You brought bit of Austria to Kent.

This dissertation would not be possible in this form without the supervision and encouragement of Stefanie Frank. Your ambition about research was infectious and motivating. I will be forever grateful for your support!

Thanks to David Palmer and several other members of the Warren group for proof reading and deaustrifying this dissertation and a paper manuscript!

Special thanks to: Rokas Juodeikis for the collaboration on TEM work, Andrew Lawrence for glowing B_{12}-analogue synthesis, Evelyne Deery for molecular biology related help and Susanne Schroeder for coffee.

I want to thank Dan Mulvihill, Kevin Howland, Ian Brown, Dave Beal, Catherine Hogwood and Wei-Feng Xue for their support within the department, proving that a PhD dissertation is more than the achievement of a single person.

Last but not least I want to thank my friends and family back home in Tyrol/Austria that gave me the necessary physical and mental distance to this work by providing a safe harbour of rest and support.

Contents

Table of Figures

Chapter 1 – Introduction

Chapter 2 – Materials and methods

Chapter 3 – Proteomic comparison of Pdu BMCs

Chapter 4 – Structural comparison of Pdu BMCs

Chapter 5 – Uptake and accumulation of cobalamin in a BMC

Chapter 6 – Final discussion and conclusions

Table of Tables

Chapter 2- Materials and methods

Chapter 3 – Proteomic analysis of Pdu BMCs

Chapter 5- Uptake and accumulation of cobalamin in a BMC

Chapter 7- Appendix

Abbreviations

1,2-PD	1,2-Propanediol
2D	Two dimensional
3D	Three dimensional
Å	Ångstrom
Ab	Antibody
Ado	Adenosyl
AFM	Atomic force microscopy
APS	Ammonium persulphate
ATP	Adenosine triphosphate
BMC	Bacterial microcompartment
eBMC	Empty microcompartment
rBMC	Recombinant bacterial microcompartment
BSA	Bovine serum albumin
CA	Carbonic anhydrase
cAMP	Cyclic adenosine monophosphate
CCM	Carbon concentrating mechanism
CDI	1,1'-carbonyldiimidazole
CN	Cyano
Co	Cobalt
CoA	Coenzyme A
CO_2	Carbon dioxide
CRP	Cyclic AMP receptor protein
Cso	Carboxysome structure
Da	Dalton
dH_2O	Distilled water
ddH_2O	Double distilled water
DMB	5,6`-Dimethylbenzimidazole
DMSO	Dimethylsulfoxide
DNA	Deoxyribonucleic acid

dNTP	Deoxyribonucleotide triphosphate
DTT	Dithiothreitol
EDTA	Ethylene Diamine Tetraacetic acid
e.g.	*Exempli gratia* (for example)
EM	Electron microscopy
ESI	Electrospray ionisation
ETA	Ethanolamine
Eut	Ethanolamine utilisation
FAD	Flavin adenine dinucleotide (oxidised form)
Fe	Iron
Fe-S	Iron-sulphur
FMN	Flavin mononucleotide (oxidised form)
FPLC	Fast protein liquid chromatography
HCCA	α-Cyano-4-hydroxycinnamic acid
HCl	Hydrochloric acid
His	Histidine
HEPES	4-(2-Hydroxyethyl)piperazine-1-piperazineethanesulfonic acid
HPLC	High performance liquid chromatography
IEF	Isoelectric focussing
IPTG	Isopropyl-β-D-thiogalactopyranoside
k	Kilo
kb	Kilobase
LB	Luria-Bertani
MALDI	Matrix-assisted laser desorption/ionisation
Me	Methyl
Mg	Magnesium
Mowse	Molecular weight search
MS	Mass spectrometry
mV	Millivolt

NAD^+	Nicotinamide adenine dinucleotide (oxidised form)
NADH	Nicotinamide adenine dinucleotide (reduced form)
Ni	Nickel
nm	Nanometre
NMR	Nuclear magnetic resonance
OH	Hydroxyl
OD	Optical density
PAGE	Polyacrylamide gel electrophoresis
PBS	Phosphate buffer saline
Pdu	Propanediol utilisation
PO_4^{3-}	Phosphate
QNM	Quantitative nano-mechanical mapping
PZT	Piezoelectric
RNA	Ribonucleic acid
RuBisCO	D-ribulose-1,5-bisphosphate carboxylase/ oxygenase
SDS	Sodium dodecyl sulphate
SH	Thiol
TA30	30:70[v/v] acetonitrile: 0.1% TFA
TAE	Tris acetate EDTA
TCA	Trichloroacetic acid
TEM	Transmission electron microscopy
TFA	Trifluoroacetic acid
TEMED	Tetramethylenediamine
TOF	Time of flight
Tris	2-Amino-2-hydroxymethyl-propane-1,3-diol
UV	Ultra violet
Vis	Visible

Chapter 1

Introduction to functional and structural aspects of protein based bacterial microcompartments

1.1 Historical Context

Up until relatively recently it was generally believed that compartmentalisation of cellular processes was a property restricted to eukaryotic life (Yeates *et al.*, 2008). Compartmentalisation within eukaryotic cells was reported as early as the late 19th century by light microscopy studies (Alberts, 1998). Eukaryotic systems achieve compartmentalisation via various membrane-bound organelles including the mitochondria, chloroplasts, lysosomes and Golgi. Some of these organelles are thought to have arisen from endosymbiotic events with proteobacteria (mitochondria) or plastids (cyanobacteria). However, more recently some bacteria have been shown to contain subcellular structures called bacterial microcompartments (BMCs) (Kerfeld *et al.*, 2005; Yeates *et al.*, 2008)).

These proteinaceous inclusion bodies, which have a regular polygonal appearance, were initially described in the cyanobacterium *Phormidium uncinatum* in 1956 by electron microscopy (Drews; Niklowitz, 1956; Shively *et al.*, 1973; Yeates *et al.*, 2008). Over the next 20 years similar polyhedral inclusions (in general 100-200 nm in diameter) were reported in various other cyanobacteria and were initially thought to correspond to viral capsids. The extraction and isolation of these intracellular polyhedral inclusions was achieved by sucrose gradient centrifugation. Electron microscopy of the isolated polyhedral structures suggested that they contained a proteinaceous envelope. The biochemical characterisation of these polyhedral structures revealed that the capsid encapsulates most of the cellular ribulose-1,5-biphosphate carboxylase/oxygenase (RuBisCO), which plays a major role in global carbon fixation (Beudeker *et al.*, 1980; Cannon; Shively, 1983; Turpin *et al.*, 1984; Cannon *et al.*, 1991; Bobik *et al.*, 1999). Consequently these intracellular polyhedral bodies were named carboxysomes. In subsequent years carbonic anhydrase (CA) was also identified as a component of the carboxysomes (Price; Badger, 1989a). In the last decade of the 20th century, a second type of carboxysome genes was identified, isolated and characterised, which differentiate in genetic organisation (Price *et al.*, 1992). The functional and structural role of carboxysome shell proteins was validated

using knock out strains (English *et al.*, 1994; English *et al.*, 1995). Shell protein knock-outs showed that the carboxysome shell is essential for the function of the organelle. The isolation of the carboxysome allowed the characterisation of the shell and interior proteins, as well as the determination of the overall structure, function and biogenesis of some carboxysomes (Schmid *et al.*, 2006; Iancu *et al.*, 2007; Long *et al.*, 2007; Kinney *et al.*, 2012; Cameron *et al.*, 2013; Chen *et al.*, 2013).

Up until 1994 the protein based compartmentalisation system of the carboxysomes was thought to be a one-off phenomenon in prokaryotic cell biology (Chen *et al.*, 1994; Havemann *et al.*, 2002; Chowdhury *et al.*, 2014). However, a comparison of genomic sequences led to the identification of a carboxysomal shell protein gene (*ccmK*) homologue in an operon associated with Ado-B_{12} dependent 1,2-propanediol (1,2-PD) utilisation (Pdu) in *Salmonella enterica* (*S. enterica*). Subsequently, *S. enterica* was shown to form similar sized structures (100-150 nm) to carboxysomes in the presence of exogenous 1,2-PD (Bobik *et al.*, 1999). This demonstrated that protein based microcompartments are involved in both anabolic processes such as carbon fixation, as well as catabolic processes such as Pdu (Yeates *et al.*, 2008; Abdul-Rahman *et al.*, 2013; Axen *et al.*, 2014; Giessen; Silver, 2015).

1.2. Carboxysomes

Despite the discovery of a wide variety of bacterial protein based organelles in recent years, carboxysomes remain the best characterised BMC system regarding structure and function (Frank *et al.*, 2013; Rae *et al.*, 2013; Chowdhury *et al.*, 2014). Carboxysomes are ubiquitous in that they are found in all bacteria using the Calvin cycle for CO_2 fixation, including photoautotrophic cyanobacteria (a diverse group of photosynthetic bacteria living in fresh-water and marine ecosystems) and some chemoautotrophs (a diverse group of organisms using inorganic energy sources as *e.g.* hydrogen sulphide, sulphur or ferrous iron) (Kerfeld *et al.*, 2010; Rae *et al.*, 2013; Frank *et al.*, 2013; Chowdhury *et al.*, 2014).

1.2.1. Why compartmentalise RuBisCO?

RuBisCO has a low turnover rate of 1-13 s^{-1} for its substrates ribulose-1,5-biphosphate and CO_2, which results in the formation of two molecules of 3-phosphoglycerate (Price *et al.*, 2008). In addition to the low turnover of the enzyme, RuBisCO can use O_2 as a substrate instead of CO_2 in an energy wasteful oxygenation reaction called photorespiration. The use of O_2 instead of CO_2 leads to the formation of one molecule of 3-phosphoglycerate and one molecule of phosphoglycolate. Thus, the produced amount of 3-phosphoglycerate is reduced. Phosphoglycolate cannot be used in the Calvin cycle and therefore phosphoglycolate needs to be recycled in a series of reactions called photorespiration (Leegood, 2007). This results in a re-release of CO_2 and a direct cost of one ATP and one NAD(P)H molecule. The compartmentalisation of RuBisCO is in general thought to counteract this inborn inefficiency by enhancing the concentration of CO_2 and reducing the concentration of O_2.

1.2.2. The functional role of carboxysomes to sequester the volatile CO_2 and to form a protein scaffold

Photosynthetic cyanobacteria require carbon uptake for carbon fixation (Rae *et al.*, 2013). Both HCO_3^- transporters and CO_2-transporters were reported to mediate the uptake of inorganic carbon into the cytoplasm of cyanobacteria. This elevates the level of cellular HCO_3^- and CO_2. At physiological conditions in the cytoplasm (pH 6.5) HCO_3^- is the more abundant species.

The general suggested function of carboxysomes is outlined in Figure 1.1. The carboxysomal shell, which encapsulates RuBisCO and CA, which catalyses the conversion of HCO_3^-, is thought to be a selectively permeable layer (Tanaka *et al.*, 2008; Yeates *et al.*, 2008; Kerfeld *et al.*, 2010; Rae *et al.*, 2013). It does this by acting as a diffusion barrier to limit CO_2 efflux and O_2 influx but yet permits the import of

ribulose-1,5-biphosphate, HCO_3^- and CO_2, and export of 3-phosphoglycerate between the carboxysome and the cellular cytoplasm. How this is achieved remains mainly unknown but carboxysome mutants unable to form intact shells require increased CO_2 levels for growth.

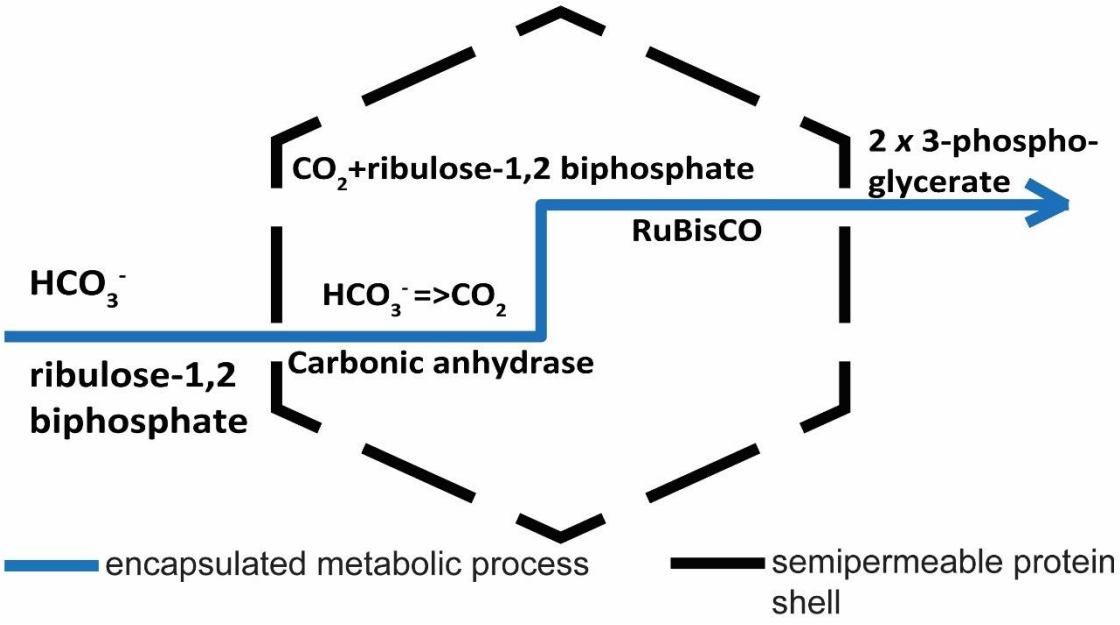

Figure 1.1. The functional role of carboxysomes.

RuBisCO acts to fix the volatile CO_2 into 3-keto-2-carboxyarabinitol-1,5-bisphosphate. The reaction product then decays spontaneously into two molecules of 3-phosphoglycerate. In addition to forming a diffusion barrier, the carboxysome was suggested to act as a protein scaffold to encapsulate the enzymes CA and RuBisCO. In so doing the CA elevates the local CO_2 levels in proximity of RuBisCO, promoting the efficiency of RuBisCO.

1.2.3. Two types of carboxysomes

Carboxysomes can be divided into two distinct types based on the associated RuBisCO and operon organisation (Yeates *et al.*, 2008; Rae *et al.*, 2013). Carboxysomes of the α-type (carboxysome operon, *cso*) are found in α-cyanobacteria. Organisms with α-carboxysomes contain type 1A RuBisCO and their carboxysome genes are arranged into a single operon. Carboxysomes of the β-type (carbon concentrating mechanism, *ccm*) are found in β-cyanobacteria and contain type 1B RuBisCO. Type 1B RuBisCO differs from 1A phylogenetically, as do both α-carboxysomes and β-carboxysomes differ in their distinct protein sets. Atypical for BMC operons, β-carboxysome genes are usually spread out over multiple gene clusters.

1.2.4. The structure of α-carboxysomes

1.2.4.1. BMC shell proteins form the shell of α-carboxysomes

The shell of the α-carboxysome is composed mostly of CsoS1 proteins, which are called CsoS1A, B, C and D (Heinhorst *et al.*, 2006; Kerfeld *et al.*, 2010; Kinney *et al.*, 2011). These proteins make up the facet or faces of the structure. As well as the CsoS1 proteins the shell also requires the proteins CsoS4A and CsoS4B, which form the vertices of the structure.

The CsoS1A-C proteins are comparatively small with a molecular mass of 10-11 kDa. CsoS1A-C contain the characteristic bacterial microcompartment (BMC) motif (pfam00936) (Tanaka *et al.*, 2009; Kerfeld *et al.*, 2010; Kinney *et al.*, 2011; Yeates *et al.*, 2011). Crystal structures of CsoS1A (PDB code: 2G13) and CsoS1C (PDB code: 3H8Y) tile up to form a flat regular hexamer as shown in Figure 1.2. An important feature of BMC protein hexamers are central pores of a defined size and charge distribution. It was proposed that the positively charged pores of CsoS1A and CsoS1C might promote the passage of negatively charged molecules such as HCO_3^- and limit the import of uncharged O_2 and efflux of CO_2, but substrate bound structures are not available.

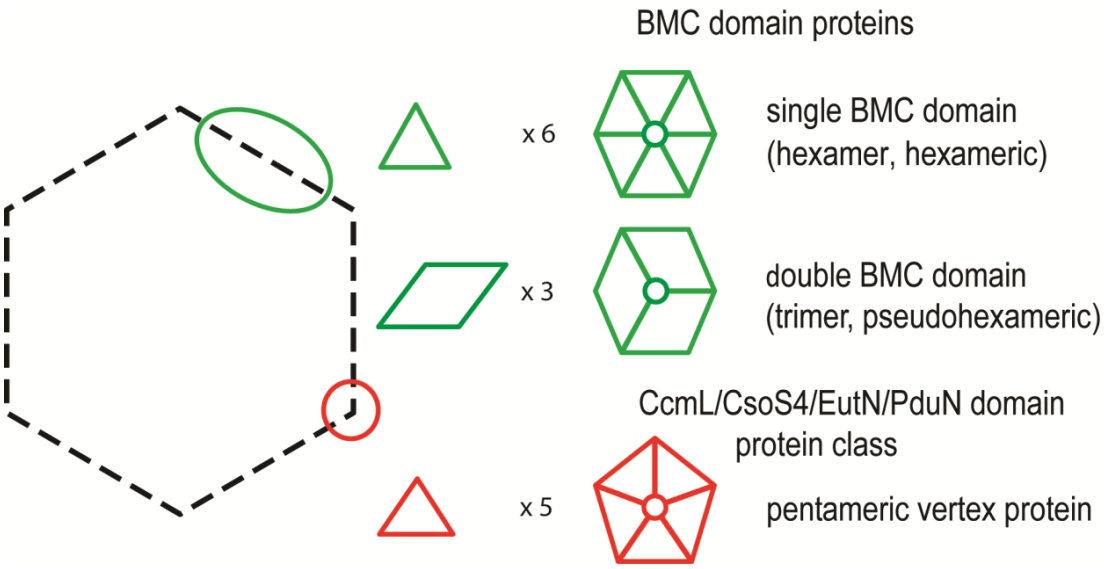

Figure 1.2. The BMC shell. Single and double BMC domain proteins (green) form the facets of the structure. Pentameric vertex proteins (red) form the vertices of the structure.

In addition to single BMC proteins, so called double (tandem) BMC proteins such as CsoS1D (PDB code: 3F56) form flat trimeric structures with a pseudohexameric symmetry (Yeates *et al.*, 2008; Rae *et al.*, 2013). Furthermore, X-ray crystallography of CsoS1D revealed that the central pore could adopt conformations representing a closed and open pore structure (Klein *et al.*, 2009; Rae *et al.*, 2013). The interchange between these conformations could gate the entry and exit of the relatively large RuBisCO substrate ribulose-1,2 biphosphate, without compromising the semipermeable nature of the shell.

The geometry of the BMC shell of carboxysomes requires a specialised protein to fill the gaps at the vertices (Tanaka *et al.*, 2008; Cai *et al.*, 2009; Rae *et al.*, 2013). In α-carboxysomes this is achieved by CsoS4A and CsoS4B, which belong to a class of distinct vertex proteins (CcmL/CsoS4/ EutN/PduN BMC motif, pfam: 03319). CsoS4A and CsoS4B form pyramidal pentamers in crystal structures (Tanaka *et al.*, 2008). Both proteins were shown to be necessary for shell closure and function of the carboxysomes in double knock out mutants of *csoS4AB* (Cai *et al.*, 2009).

1.2.4.2. The overall structure of α-carboxysomes

Carboxysomes from the α-type form regular polyhedral structures. Such icosahedral structures as assigned for carboxysomes consist of 20 triangular faces (Johnson; Speir, 1997; Schmid *et al.*, 2006; Rae *et al.*, 2013). Five faces meet around each of the 12 vertices. The formation of such regular structures was suggested in 1974 after visualisation of negatively stained samples by TEM (Bock *et al.*, 1974). However it was not until 2006 that 2D cryo-tomographs of isolated α-carboxysomes from *Halothiobacillus neapolitanus* (*H. neapolitanus*) were reconstructed into a regular icosahedral 3D model, which is shown in Figure 1.3.

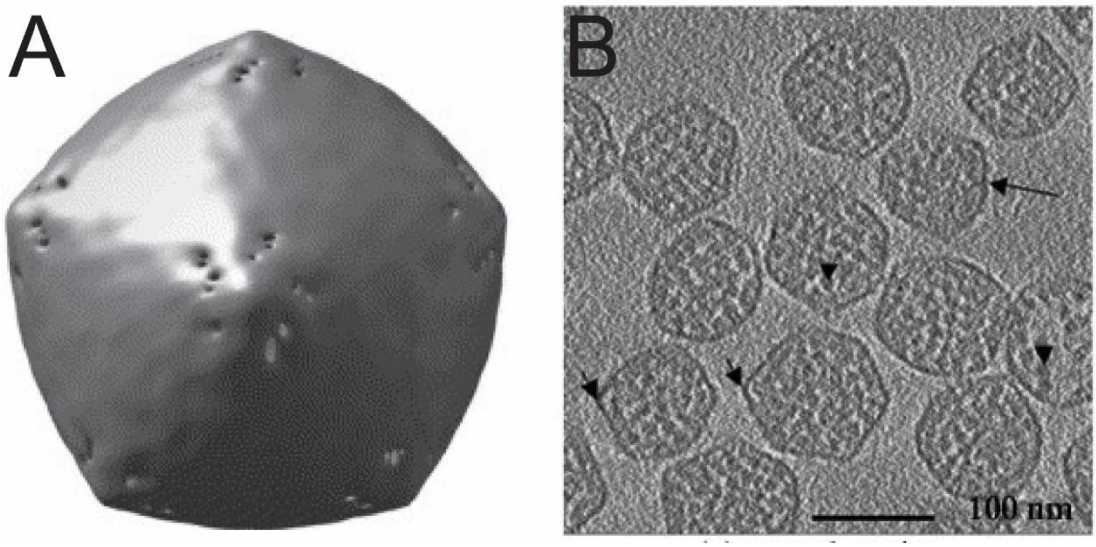

Figure 1.3. The regular icosahedral nature of α-carboxysomes from *H. neapolitanus*. **A.** Icosahedral model of a reconstructed α-carboxysome. **B.** Cryo-tomographic slice through the centre of isolated α-carboxysomes (Schmid *et al.*, 2006).

The model highlights a regular icosahedral shape of isolated α-carboxysomes, similar to many viral capsids, which have common structural features but are phylogenetically unrelated to BMCs (Caspar; Klug, 1962; Johnson; Speir, 1997; Schmid *et al.*, 2006; Tanaka *et al.*, 2010). The regular nature of α-carboxysomes is supported by single particle analysis that determined a homologous size (100 ± 10 nm) for isolated α-carboxysomes from *H. neapolitanus*. Interestingly,

though, α-carboxysomes from *Prochlorococcus marinus* form smaller structures of about 90 nm and α-carboxysomes of *Nitrobacter agilis* were reported to form structures with an average diameter of 120 nm (Shively *et al.*, 1977; Van Eykelenburg, 1980; Roberts *et al.*, 2012; Rae *et al.*, 2012; Rae *et al.*, 2013). Functional roles associated with these size differences are not reported and the driving forces of these structural changes are widely unknown. Size differences of α-carboxysomes are discussed in Section 1.3 with respect to β-carboxysomes.

1.2.4.3. The internal organisation of α-carboxysomes

CsoS2 has been suggested to play a central role for the internal organisation of α-carboxysomes (Rae *et al.*, 2013). The *csoS2* gene codes for a full-length protein (CsoS2A, 130 kDa) and a shorter protein (CsoS2B, 85 kDa) in *H. neapolitanus* (Heinhorst *et al.*, 2006). CsoS2 contains two protein domains with unknown functions but was shown to interact with several carboxysome proteins (Baker *et al.*, 1999; Cannon *et al.*, 2003; So *et al.*, 2004; Gonzales *et al.*, 2005; Rae *et al.*, 2013). The rough 1:1 stochiometry of RuBisCO to CsoS2 suggested a role in recruiting RuBisCO directly to the carboxysomes shell (Heinhorst *et al.*, 2006). This would suggest a shell centred structure for α-carboxysomes. This hypothesis is supported by electron microscopy data reporting on α-carboxysomes with loose central packing (Baker *et al.*, 1998; Menon *et al.*, 2008; Rae *et al.*, 2013). To conclude, the current view on the internal organisation of α-carboxysomes suggests a shell-centred structure, which recruits CA directly and RuBisCO via CsoS2 but requires the elucidation of the functional role of CsoS2 in more detail.

1.2.4.3. Simultaneous assembly of α-carboxysomal shell and lumen

The biogenesis of α-carboxysomes has not been studied directly but a model was hypothesised from structural observations, regarding the potential interaction of CsoS2 with shell proteins, carboxysomal CA and RuBisCO (Price; Badger, 1989b; Price;

Badger, 1991; Rae *et al.*, 2013). This model suggests the simultaneous formation of the encased enzymes and shell assembly.

1.2.5. The structure of β-carboxysomes

1.2.5.1. BMC shell building blocks of β-carboxysomes

As for α-carboxysomes, the majority of the β-carboxysomal shell is formed of single BMC proteins (CcmK2-4, PDB: 2A1B, 2A10), which form hexameric tiles, and the tandem BMC shell proteins CcmO and CcmP (PDB code: 4HT5), forming trimeric pseudohexameric structures (Kerfeld *et al.*, 2005; Samborska; Kimber, 2012; Rae *et al.*, 2012; Rae *et al.*, 2013). The pentameric vertex protein CcmL (PDB code: 2QW7) plays a more specialised role in closing the structure at the vertices (Tanaka *et al.*, 2008).

1.2.5.2. The overall structure of β-carboxysomes

As with the α-carboxysomes of *H. neapolitanus,* a similar cryo-electron tomography approach led to the structure of isolated β-carboxysomes from *Synechococcus* strain WH8102 (Schmid *et al.*, 2006; Iancu *et al.*, 2007). The β-carboxysome was found to have an icosahedral structural topology with a size of 120 ± 10 nm in diameter, which reflects the regular icosahedral nature of carboxysomes. The internal organisation of RuBiscO suggested a tight para-crystalline packing of RuBisCO in the lumen of the β-carboxysomes, in contrast to the loose central packing of RuBisCO suggested for α-carboxysomes (Iancu *et al.*, 2007; Rae *et al.*, 2013).

Interestingly, the average diameter of β-carboxysomes appears to be more variable in comparison to α-carboxysomes (90-120 nm; Figure 1.3; Section 1.2.4) (Rae *et al.*, 2013). The diameter of β-carboxysomes can range from approximately 120 nm in *Synechococcus* strain WH8102, to about 175 nm in *Synechococcus elongatus* or more than 500 nm in *Spirulina platensis*. This difference in size range between α- and β-

carboxysomes is thought to reflect differences in assembly and structure of the two BMCs.

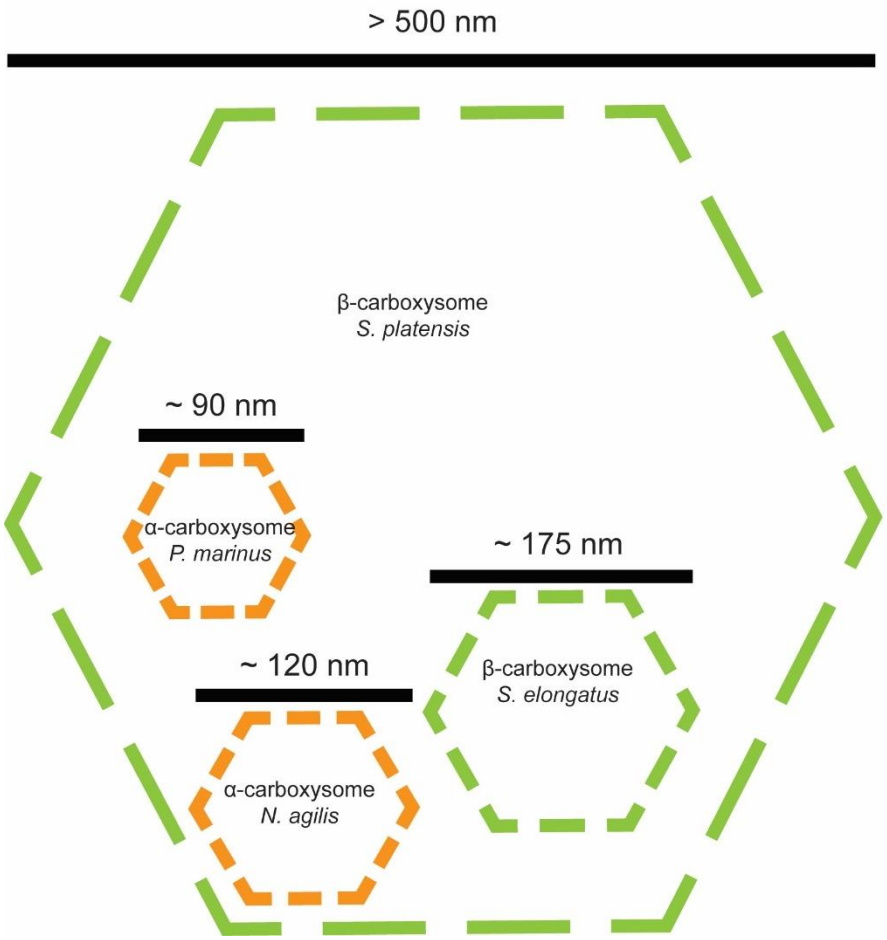

Figure 1.4. Comparison of carboxysome size. (*Nitrobacter agilis*, *Prochlorococcus marinus*) are coloured in orange. β-carboxysomes (*Synechococcus elongatus*, *Spirulina platensis*) are coloured in green.

Differences in diameter size also reflect a difference in volume and outer surface area, which likely mirror functional and structural differences of these supramolecular assemblies (Rae *et al.*, 2013).

1.2.5.3. The internal structure of β-carboxysomes

The ground work necessary to determine the sequential assembly of β-carboxysomes came from biochemical studies determining the function of the scaffolding protein CcmM and the intermediary protein CcmN (Long *et al.*, 2007; Pena *et al.*, 2010; Chowdhury *et al.*, 2014).

Binding studies (pull down studies) suggested that the scaffolding protein CcmM-58 (58 kDa) cross-links multiple RuBisCO and CA proteins into an extended network that promotes carbon fixation (procarboxysome). The N-terminus of CcmM-58 has sequence similarity to CA and was suggested to bind CA. The C-terminus of CcmM-58 has three to five tandem repeats with the small subunit of RuBisCO. Binding and comparative studies suggest that CcmM crosslinks the metabolic enzymes for carbon fixation (RuBisCO and CA) (Long *et al.*, 2007; Pena *et al.*, 2010; Kinney *et al.*, 2012; Chen *et al.*, 2013; Cameron *et al.*, 2013).

The truncated C-terminal isoform CcmM-35 (35 kDa) of CcmM-58 only consists of three to five tandem repeats with the small subunit of RuBisCO and is supposed to crosslink RuBisCO in the centre of the lumen (Kinney *et al.*, 2012). CcmM is therefore thought to organise the lumen of β-carboxysomes.

The internalised RuBisCO-CcmM-CA procarboxysome complex is associated with the shell via the intermediary protein CcmN (Kinney *et al.*, 2012; Cameron *et al.*, 2013; Chen *et al.*, 2013). The N-terminal domain of CcmN binds the encapsulated scaffolding protein CcmM; the C-terminal peptide of CcmN interacts with the major carboxysomal shell protein CcmK2. The outer shell of β-carboxysomes consists of CcmK2-4, CcmO and CcmP, which contain the BMC motif, and the pentameric vertex protein protein CcmL. Therefore, the scaffolding proteins CcmM and CcmN play essential roles in the biogenesis of carboxysomes and allowed the elucidation of carboxysome biogenesis. Due to the central role of CcmM in forming the procarboxysome, β-carboxysomes are suggested to form lumen centred structures, in contrast to α-carboxysomes.

1.2.5.4. Biogenesis of the β-carboxysomes

In contrast to the suggested non-sequential assembly mechanism for α-carboxysomes, biochemical and structural studies suggest a sequential assembly of β-carboxysomes. The biogenesis of β-carboxysomes was examined in two independent studies employing time-lapse fluorescence microscopy and electron microscopy of knock-out strains from *Synechococcus* PCC 7942 (Chen *et al.*, 2013; Cameron *et al.*, 2013). This determined the assembly pathway of nucleating CA with RuBisCO via the scaffolding protein CcmM. Next CcmN associates with the nucleated procarboxysome consisting of RuBisCO, CA and CcmM, followed by the recruitment of hexameric shell proteins (CcmK2-4), the trimers (CcmO and CcmP) and pentameric vertex proteins (CcmL). During shell closure, excess material of the procarboxysome is pinched off. The excess material then functions as a nucleation zone for future β-carboxysome biogenesis. The “pinching off” process is called a budding event.

1.3. The relation of carboxysomes to other bacterial microcompartments

In addition to the anabolic carbon fixation process that is encapsulated within carboxysomes, protein based bacterial microcompartments are also found to be involved in a series of catabolic processes (metabolosomes) such as 1,2-PD utilisation and ethanolamine utilisation (Eut) (Penrod; Roth, 2006; Tsoy *et al.*, 2009; Abdul-Rahman *et al.*, 2013; Chowdhury *et al.*, 2014; Axen *et al.*, 2014). According to several recent comparative genomic studies, bacterial microcompartments are a widespread phenomenon with up to 20-30% of eubacteria having the genomic potential to form such supramolecular assemblies and sequester metabolic pathways (Abdul-Rahman *et al.*, 2013; Axen *et al.*, 2014). Indeed, BMC loci have been identified in 23 different bacterial phyla, representing around 30 distinct BMC loci and subtypes were identified, many with only partly known metabolic functions.

The comparative genomic approaches have reported on catabolic BMCs, which are involved in the metabolism of 1,2-PD, choline, ethanol, ethanolamine, fucose and rhamnose. It also appears that BMCs are involved in other processes that are still to be determined. Despite this diversity of functional roles in anabolic and catabolic processes, BMC associated processes all appear to include volatile or cytotoxic intermediates. Furthermore, common genes are found associated with metabolosomes *e.g.* genes for aldehyde dehydrogenase (94%), alcohol dehydrogenase (76%), phosphotransacylase (66%) and genes encoding for proteins that are potentially associated with filament based organelle movement (68%) are very common and conserved along functionally divergent catabolic BMC loci and subtypes. In this respect, it also appears that structural proteins forming the BMC shell are conserved from α- and β-carboxysomes through to catabolic metabolosomes as shown for Pdu and Eut metabolosomes in Figure 1.5. Because they are formed from very similar shell proteins, it was initially suggested that anabolic and catabolic BMCs might well form similar structures (Wheatley *et al.*, 2013).

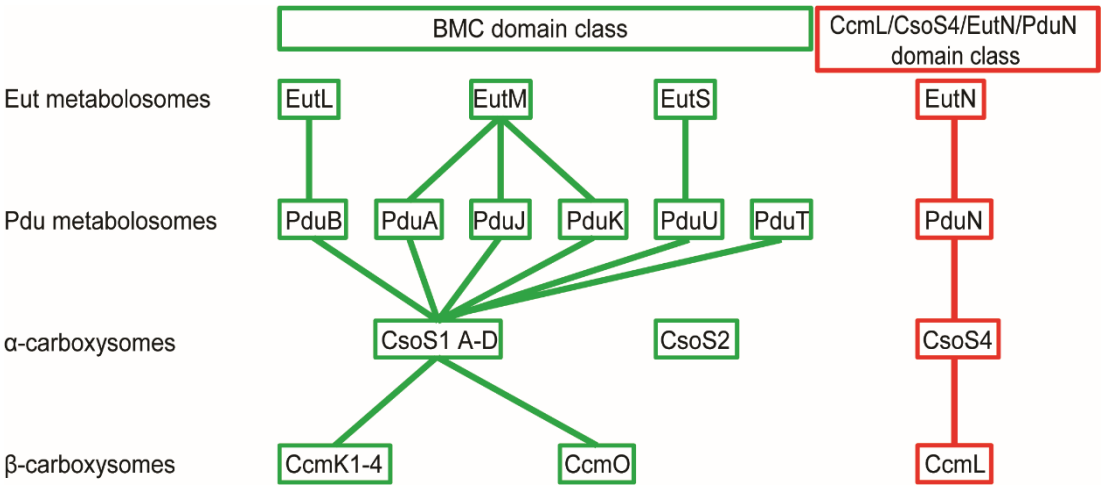

Figure 1.5. Phylogenetically conserved BMC domains. BMC domain proteins forming hexameric or pseudohexameric structures are coloured in green. The pentameric vertex protein domain class CcmL/CsoS4/EutN/PduN proteins are coloured red (Frank *et al.*, 2013).

1.4. 1,2-Propanediol utilising (Pdu) metabolosomes

Pdu microcompartments are the best studied catabolic BMC model system beside the structurally and functionally related ethanolamine utilising (Eut) metabolosomes (Chowdhury *et al.*, 2014). Both are supposed to protect the cell from a cytotoxic aldehyde intermediate and to encapsulate metabolic enzymes for Pdu or Eut degradation. In addition, both share their requirement for an Ado-B_{12} dependent enzymatic step and a proposed BMC associated reactivation of Ado-B_{12}. Functional aspects of metabolic enzymes and several crystal structures of Pdu and Eut BMC shell proteins have been reported, but little information is available concerning the overall structure, assembly and internal structural organisation of catabolic BMCs (Havemann; Bobik, 2003; Wheatley *et al.*, 2013; Chowdhury *et al.*, 2014). Similarly, little is known about transport of prosthetic groups such as Ado-B_{12} across the shell, although this aspect is partly addressed later in this thesis (Chapter 5).

1.4.1. Ecology and distribution of 1,2-PD degradation

1,2-PD is an important anaerobic breakdown product of the common plant sugars fucose and rhamnose (Toraya *et al.*, 1979; Obradors *et al.*, 1988). The degradation of 1,2-PD results in the formation of 1-propanol and propionate. The metabolism of 1,2-PD therefore has an important ecological role in the degradation of plant sugars in the soil (Frank *et al.*, 2013; Chowdhury *et al.*, 2014). Furthermore, Pdu has been suggested to play a role in pathogenesis in the human gut where 1,2-PD can be respired with tetrathionate (Conner *et al.*, 1998; Thiennimitr *et al.*, 2011). In this respect, genetic studies have confirmed the presence of *pdu* operons in enteric bacteria such as *Citrobacter*, *Clostridium*, *Klebsiella*, *Lactobacillus*, *Lactococcus*, *Listeria*, *Salmonella*, *Yersinia* and at least one *E. coli* (E24377A) strain (Chowdhury *et al.*, 2014).

1.4.2. The *pdu* operon

The genes encoding for the Pdu BMC shell, metabolic enzymes, cofactor reactivation and regulation are organised into a single operon in *S. enterica* (Chen *et al.*, 1994; Bobik *et al.*, 1999). The Pdu transcription factor gene (*pocR*) and 1,2-PD diffusion facilitator (*pduF*) gene are divergently transcribed from the main *pdu* operon, which encodes for 22 *pdu* genes (*pduABCDEGHJKLMNOPQSTUVWX,* Figure 1.6) (Bobik *et al.*, 1992; Rondon; Escalante-Semerena, 1992)).

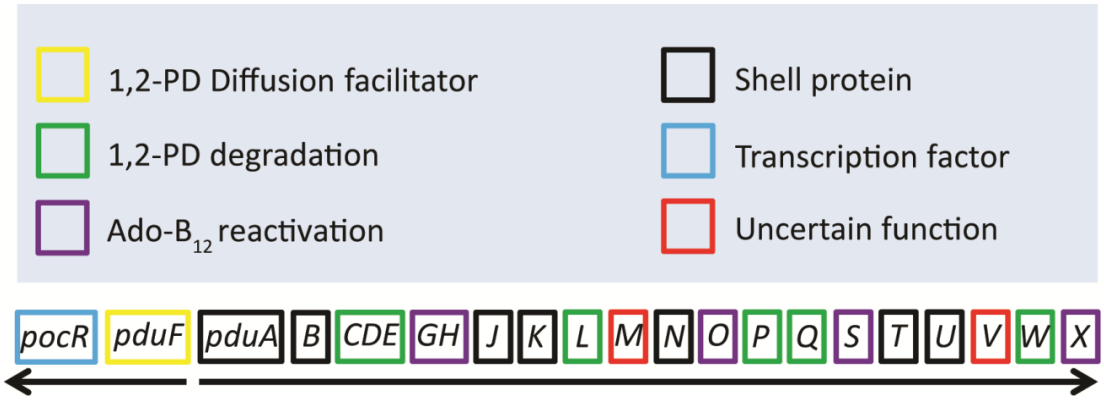

Figure 1.6. The *pdu* operon organisation. Gene names are coloured according to their functional role. The transcription direction is shown by black arrows.

In contrast to the comparatively simple two step pathway found in carboxysomes (CA and RuBisCO), the main *pdu* operon encodes for seven metabolic pathway enzymes (PduCDELPQW) and four Ado-B_{12} reactivation factors (PduGHSO) (Cheng *et al.*, 2008; Frank *et al.*, 2013). Thus, the catabolic Pdu BMCs, which form structures with a diameter of 100-150 nm, with a suggested molecular mass of 600 MDa and 18,000 individual polypeptides of 18-20 types, likely represent the most complex protein assemblies found in bacteria.

In addition to the metabolic enzymes for Pdu and Ado-B_{12} reactivation, the *pdu* operon encodes for structural BMC proteins that form the proteinaceous envelope (PduABJKNTU) (Havemann *et al.*, 2002; Havemann; Bobik, 2003). PduM has no BMC

domain but has been suggested to play a structural role because *pduM* knock-out mutants were proposed to be impaired in BMC formation (Sinha *et al.*, 2012). PduV is an AAA GTPase family member and is thought to play a role in the filamentous movement of the BMCs to position it in the cell and during cell division (Parsons *et al.*, 2010a). PduX has a role in Ado-B_{12} biosynthesis and is not a component of the BMC (Havemann; Bobik, 2003; Fan; Bobik, 2008).

1.5. The functional role of Pdu metabolosomes

1.5.1. Pdu BMCs sequester a cytotoxic compound

One proposed function of the Pdu metabolosome is to sequester the intermediate propionaldehyde, which is known to be cytotoxic (Cheng *et al.*, 2008; Rae *et al.*, 2013; Chowdhury *et al.*, 2014). In agreement with this hypothesis, BMC mutants unable to form Pdu metabolosome structures, or limited in propionaldehyde metabolism in *S. enterica*, accumulate propionaldehyde in the growth medium when grown on 1,2-PD (Havemann *et al.*, 2002; Sampson; Bobik, 2008). Mutant strains undergo a 20 h growth arrest due to propionaldehyde toxicity. Increased mutation rates were also reported for these mutant strains (Cheng *et al.*, 2011; Chowdhury *et al.*, 2014). Therefore, propionaldehyde is suggested to be cytotoxic by increasing mutation rates in *S. enterica*. Mutants disabled in BMC formation and *polA* (DNA repair polymerase) are unable to grow on 1,2-PD in *S. enterica* (Chowdhury *et al.*, 2014). Further studies used the characteristic growth arrest on 1,2-PD to describe the functionality of BMC knock-out mutants (Cheng *et al.*, 2011; Chowdhury *et al.*, 2015).

1.5.2. The BMC associated degradation pathway for 1,2-PD

As well as the sequestration of a cytotoxic intermediate, the BMC encapsulates enzymes for the utilisation of 1,2-PD, which can serve as an ATP and carbon source under aerobic conditions. For function, the Pdu metabolosome needs to acquire its substrate 1,2-PD, a multitude of cofactors (Ado-B_{12}, ATP CoA and NAD^+) and export metabolic products (1-propanol, propionyl-phosphate and propionyl-CoA) (Bobik *et al.*, 1997; Frank *et al.*, 2013; Huseby; Roth, 2013; Chowdhury *et al.*, 2014). How this is achieved remains largely unknown, although some insights have been gained on diffusion and transport processes based on the structural characterisation of a number of the BMC shell proteins by X-ray crystallography (Section 1.6). The cellular accumulation of propionaldehyde is reported to induce toxicity, which leads to a growth arrest (Cheng *et al.*, 2008; Cheng *et al.*, 2011). Therefore, the catalysis of encased enzymes is suggested to improve the detoxification of the accumulated aldehyde intermediate. Propionaldehyde is metabolised to propionyl-CoA by propionaldehyde dehydrogenase (PduP) or alternatively is reduced to 1-propanol by 1-propanol dehydrogenase (PduQ).

Propionyl-CoA is converted to propionyl-phosphate by the phosphotransacylase PduL. A propionate kinase (PduW) generates one molecule of ATP by substrate level phosphorylation of propionyl-phosphate to propionate. Alternatively, propionyl-CoA can feed directly into the methyl-citrate pathway under aerobic conditions (Horswill; Escalante-Semerena, 1997; Horswill; Escalante-Semerena, 1999). In the methyl-citrate pathway, propionyl-CoA is fused to oxaloacetate to form methyl-citrate, which is converted to succinate and pyruvate. Pyruvate is metabolised further to acetyl-CoA, which enters the tricarboxylic acid cycle. Mutations within the methyl-citrate pathway locus of *S. enterica* prevent the use 1,2-PD as a sole carbon source under aerobic conditions (Palacios *et al.*, 2003).

Anaerobically, the disproportionation of propionaldehyde into propionyl-CoA and 1-propanol allows for redox balancing. Obviously, under fermentative conditions 1,2-PD does not serve as a sole carbon source for *S. enterica* (Price-Carter *et al.*, 2001). Nonetheless growth on 1,2-PD is reported to increase the cell yield by providing ATP (Lawrence; Roth, 1996; Liu *et al.*, 2007).

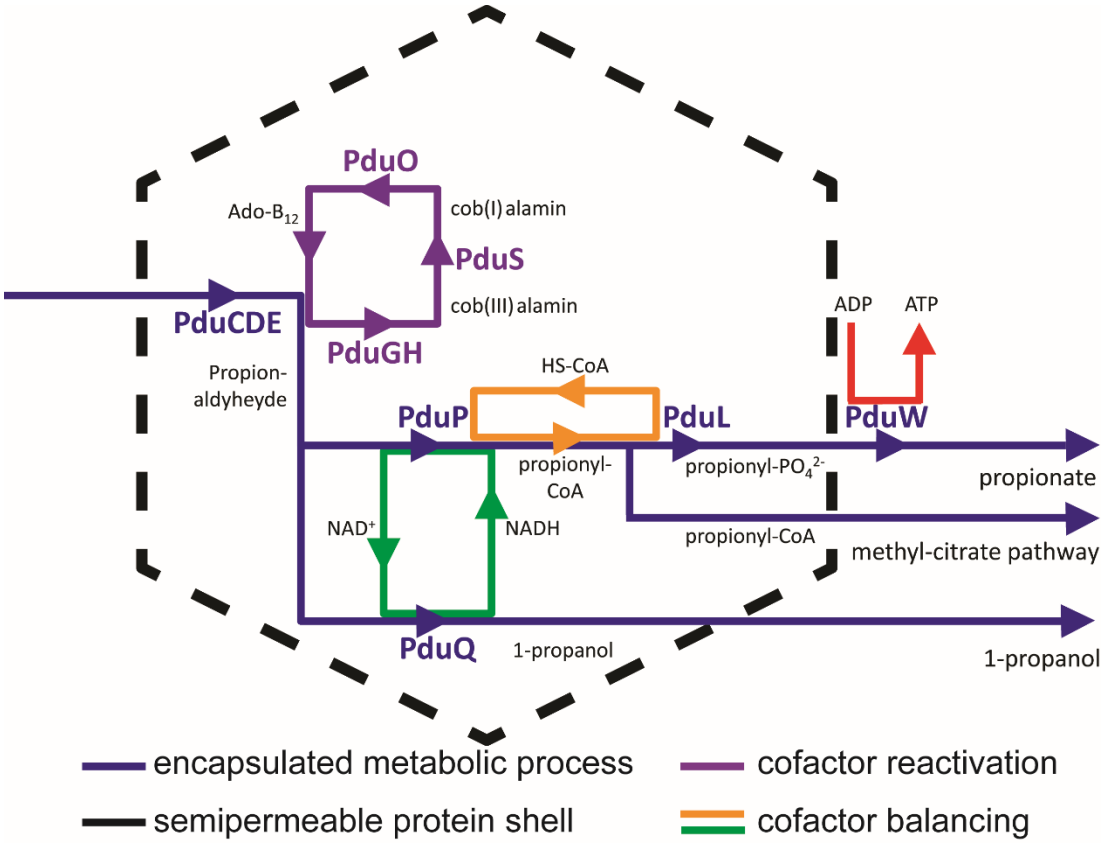

Figure 1.7. Pdu metabolosomes associated 1,2-PD degradation pathway.

1.5.3. A potential additional role of the BMC in cofactor balancing of NAD^+/H and CoA and internal reactivation of Ado-B_{12}.

1.5.3.1. Cofactor balancing.

On top of the suggested roles of the Pdu BMC in sequestering the cytotoxic propionaldehyde and metabolic enzymes for Pdu, the BMC is thought to optimise the reaction environment in the lumen via cofactor balancing and cofactor reactivation (Figure 1.7) (Havemann; Bobik, 2003; Cheng *et al.*, 2012; Liu *et al.*, 2015).

Enzymatic assays on isolated Pdu metabolosomes suggested a role for PduQ in supporting the activity of PduP by providing NAD^+ (Cheng *et al.*, 2012). In a similar fashion, PduL is suggested to recycle CoA for the activity of PduP in the lumen of the

BMC. However, the latter suggestion is not supported by enzymatic assays or confirmation of the internal localisation of PduL (Liu *et al.*, 2015). Cofactor recycling by PduQ and PduL is likely to improve 1,2-PD degradation. It has been suggested that the Pdu BMC contains and recycles private cofactor pools of NAD^+ and CoA which are encapsulated in the lumen during self-assembly (Huseby; Roth, 2013). This was suggested from growth phenotypes and computational models for the related Eut metabolosomes. Huseby and Roth further suggest that ethanolamine ammonia-lyase (EutBC), which plays a similar functional role to PduCDE is associated on the outside of the structure, instead of the inside, where EutBC injects the reaction product acetaldehyde into the lumen. This contradicts the general hypothesis that BMCs encapsulate their metabolic enzymes. However, the study by Huseby and Roth does exemplify two major issues in the investigation of BMC structures in general: (I) the localisation of metabolic enzymes and (II) the diffusion or transport mechanisms required to transverse the shell.

1.5.3.2. Ado-B_{12}-reactivation

In addition to the potential capability of the BMC to recycle cofactors, the Pdu BMC encodes for reactivation factors for Ado-B_{12}. This is needed because Ado-B_{12} periodically loses its adenosyl group during the dehydration of 1,2-PD, which leads to the formation of an inactive [OH-B_{12}-PduCDE] complex (Kazutoshi *et al.*, 1982; Toraya, 2000). The inactive complex is reactivated by freeing the OH-B_{12} from the apo-PduCDE by the action of the reactivase PduGH. Holo PduCDE reassociates with Ado-B_{12}. The OH-B_{12} is reduced to cob(I)alamin by PduS, a cobalamin reductase. The final step is catalysed by the adenosyltransferase PduO, which results in the formation of Ado-B_{12} (Escalante-Semerena *et al.*, 1990; Fonseca; Escalante-Semerena, 2000; Fonseca; Escalante-Semerena, 2001). The proteomic analysis of isolated Pdu metabolosomes from *S. enterica* has confirmed the presence of all the required reactivating enzymes (PduGH, PduS and PduO) in isolated BMC fractions (Havemann; Bobik, 2003; Cheng; Bobik, 2010; Parsons *et al.*, 2010b; Cheng *et al.*, 2012).

1.6. The structure of the Pdu BMC

1.6.1. The building blocks of the BMC shell

The shell of Pdu metabolosomes is composed of seven different shell proteins: PduA, PduB with PduB`, PduJ, PduK, PduN, PduT and PduU, as shown in Figure 1.8 (Frank *et al.*, 2013). PduA, PduJ, PduK and PduU are single BMC domain shell proteins (Havemann; Bobik, 2003; Yeates *et al.*, 2011; Cheng *et al.*, 2011). PduB, its N-terminal truncated isoform PduB`, and PduT contain two BMC motifs. Thus, PduB and PduT are fused shell proteins. PduN is closely related to other pentameric vertex proteins (Wheatley *et al.*, 2013). As outlined in Figure 1.8, crystal structures are available for PduA, PduB, PduT and PduU. No crystallographic data are available for PduJ, PduK and PduN.

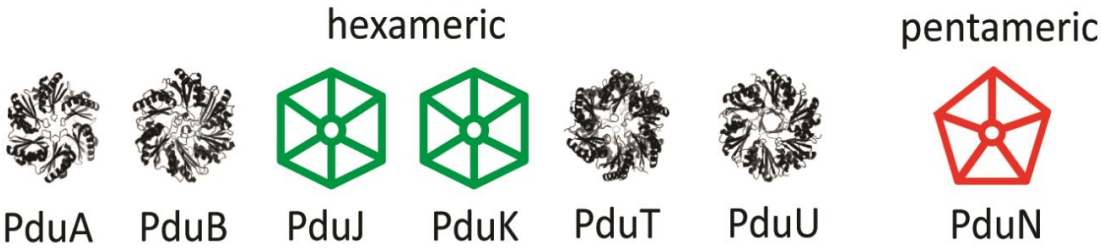

Figure 1.8. Schematic illustration of Pdu shell proteins.

1.6.1.1. The canonical BMC shell protein PduA

PduA is a single BMC domain protein (94 amino acids in *S. enterica*) and forms a hexameric structure with a distinct central pore (PDB code: 3NGK) (Havemann; Bobik, 2003; Frank *et al.*, 2013; Chowdhury *et al.*, 2014). Immunolabelling suggests that PduA is incorporated into the Pdu metabolosome shell of *S. enterica* (Havemann *et*

al., 2002). The central pore of a PduA hexameric tile is thought to allow the movement of 1,2-PD into the compartment, as the pore size of 5.6 Å is large enough to permit the movement of 1,2-PD without having to undergo any major conformational changes (Crowley *et al.*, 2010; Pang *et al.*, 2014; Chowdhury *et al.*, 2015). Hydrogen bond donors and acceptors in the PduA pore could help to bind the two hydroxyl groups of 1,2-PD and facilitate transport. Propionaldehyde is more apolar than 1,2-PD and has only 1 hydrogen bond acceptor and no donors. Thus, the efflux of cytotoxic propionaldehyde is limited from Pdu metabolosomes. PduA is thought to contribute to the flat faces of the overall structure.

PduA hexamers form a continuous 2D layer without any gaps in the crystal, suggesting strong interactions between the hexamers (Crowley *et al.*, 2010; Pang *et al.*, 2014; Chowdhury *et al.*, 2015).

1.6.1.2. PduJ is related to PduA but functionally divergent

PduJ is closely related to PduA (>80% sequence identity) (Cheng *et al.*, 2011). No crystal structure of PduJ is available to date but knock-out mutants of *pduJ* indicate a structural requirement in Pdu metabolosomes of *S. enterica*. Elongated structures were observed for knock-out mutants of *pduJ*. As a consequence, a structural role for PduJ in the formation of the BMC is more than likely.

1.6.1.3. The double BMC domain shell protein PduBB` might form a gated pore

Proteomic approaches have confirmed that *pduB* encodes two isoforms with an alternative start leading to a truncated version of PduB called PduB`, lacking 37 amino acids of the N-terminus in *S. enterica* (Havemann; Bobik, 2003; Parsons *et al.*, 2010a). The function of the truncation is not reported (Parsons *et al.*, 2010a). As for other

tandem BMC shell proteins, a gated pore with a functional role in cofactor transport has been mooted (Tanaka *et al.*, 2010; Pang *et al.*, 2012; Thompson *et al.*, 2014).

The crystal structure of PduB from *Lactobacillus reuteri* (PDB code: 4FAY,) showed trimeric flat hexagons analogous to other reported tandem BMC domain proteins. PduB forms 2D protein sheets in crystals (Pang *et al.*, 2012). Edge contacts between PduB hexamers are slightly out of alignment, which potentially reduces the sheet stability but is likely to increase the flexibility in the assembled structure. The crystal structure shows a closed central pore and three smaller pores. The large pore was proposed to accommodate the transport of large cofactors as *e.g.* ATP, NAD/H, CoA or Ado-B_{12} (Tanaka *et al.*, 2010; Pang *et al.*, 2012). The smaller pores are predicted to mediate the transport of the BMC substrate 1,2-PD (Sagermann *et al.*, 2009; Pang *et al.*, 2012).

1.6.1.4. PduK has a C-terminal domain of unknown function

PduK is a single-BMC domain shell protein of 160 amino acids in length. The PduK BMC domain has a C-terminal extension (~70 amino acids) with a recognisable [Fe-S] cluster binding motif (CNLCLDPKCPRQKGEPRTLC) (Crowley *et al.*, 2010; Cheng *et al.*, 2011). Purified PduK binds iron, supporting the presence of a Fe-S centre. A potential role in electron transfer was therefore suggested, however no evidence for an intact Fe-S cluster has actually been provided.

1.6.1.5. PduN is a pentameric vertex protein

PduN is related to other pentameric vertex proteins such as EutN, CsoS4 and CcmL. PduN knock-out mutants in *S. enterica* form a variety of morphologies including elongated, enlarged and aggregated BMCs, all of which are associated with a growth arrest, corresponding to dysfunctional Pdu metabolosomes (Cheng *et al.*, 2011; Chowdhury *et al.*, 2014). Due to its low abundance, the association of PduN with the

BMC was only confirmed by western blot analysis, GFP labelling and tandem mass spectrometry (Parsons *et al.*, 2010a; Cheng *et al.*, 2011; Sinha *et al.*, 2012). Such low abundance is expected because of the predicted specialised structural role of PduN as a vertex protein (Parsons *et al.*, 2010a; Sinha *et al.*, 2012).

1.6.1.6. PduT has a Fe-S cluster instead of a central pore

PduT is a double-BMC shell protein with 184 amino acids (Havemann; Bobik, 2003; Crowley *et al.*, 2010; Pang *et al.*, 2011). Crystallographic studies revealed that PduT (PDB code: 3N79) is a homotrimer with pseudohexameric symmetry. In contrast to other BMC domain proteins, PduT crystals did not form 2D layers. Interestingly, the pore of PduT is thought to contain a Fe-S centre, which is proposed to play a role in electron transport or as a Fe-S insertase (Parsons *et al.*, 2008).

1.6.1.7. PduU has a β-barreled pore

Crystallised PduU (PDB code: 3CGI) from *S. enterica* shows a unique circularly permuted BMC fold. The hexagonal layers are not well packed and have a tendency to form strips of side by side hexamers in crystal structures (Crowley *et al.*, 2008). This suggests weak interactions between PduU hexamers. The unusual six stranded parallel β-barrel of PduU in the central pore makes it structurally unique because β-barrel strands usually consist of a higher number of strands (*e.g.* 12 in transmembrane proteins).

1.6.2. Internal organisation of Pdu metabolosomes and the protein-protein network.

1.6.2.1. Targeting sequences are thought to mediate the encapsulation of metabolic enzymes

In addition to the characterisation of β-carboxysome scaffolding proteins CcmM and CcmN, discussed in Section 1.2, N-terminal extensions of PduD and PduP were found to help encapsulation of metabolic enzymes within Pdu metabolosomes (Section 1.5) (Fan *et al.*, 2010; Fan; Bobik, 2011; Fan *et al.*, 2012; Choudhary *et al.*, 2012; Chowdhury *et al.*, 2014; Jakobson *et al.*, 2015). N-terminal extensions of PduD (PduD18 and PduD60) and PduP (PduP18) are not required for the enzymatic activity but share a common hydrophobic motif, which appears to be conserved across the Eut and glycyl radical protein BMC systems. *In silico* studies suggest an interaction between the targeting sequences of PduD and PduP with C-terminal extensions on the BMC shell proteins PduA, PduJ and PduK. This interaction was shown by pull down assays of PduA and PduJ with PduP from *S. enterica* (Fan *et al.*, 2010; Fan *et al.*, 2012). A second study reported on the association of PduK and PduP in pull down studies from *C. freundii* (Lawrence *et al.*, 2014). Thus, the association of BMC shell protein with PduP supports an interaction of shell proteins with encapsulated enzymes. Key residues for the encapsulation of PduP (E7, I10 and L14) were identified via alanine scanning mutagenesis (Kim; Tullman-Ercek, 2014). More recently, the in-solution structure (by NMR) of PduP18 from *C. freundii* suggested an amphiphilic and helical structure of the peptide (Lawrence *et al.*, 2014).

As with the targeting sequences of PduD and PduP, an N-terminal targeting sequence was postulated for PduL (Liu *et al.*, 2015). However the majority of incorporated Pdu BMC proteins do not appear to have obvious non-enzymatic extensions or targeting sequences. This suggests additional incorporation mechanisms to the role of helical amphiphilic targeting sequences (Frank *et al.*, 2013; Chowdhury *et al.*, 2014).

1.6.2.2. The Pdu BMC interactome

One possible way to incorporate multiple proteins within a BMC shell via few targeting sequences is the formation of protein-protein complexes of internalised proteins. Proteomic analysis of isolated Pdu BMCs from *S. enterica* identified the

presence of the following Pdu BMC proteins PduA-B-CDE-GH-K-L-M-N-O-P-Q-S-T-U-V (Havemann; Bobik, 2003; Sinha *et al.*, 2012). PduCDE and PduGH are reported to form protein complexes for the Ado-B_{12} dependent 1,2-PD dehydratase and dehydratase reactivase, respectively (Bobik *et al.*, 1997; Havemann; Bobik, 2003). Pull down studies indicate interactions between enzymes such as PduP with PduQ (Cheng; Bobik, 2010; Cheng *et al.*, 2012). Pull down assays also highlighted interactions of the BMC shell protein PduT with PduS of *S. enterica* (Cheng *et al.*, 2012). Bacterial two hybrid studies infer interactions between PduS and PduO.

1.6.3. The overall structure of Pdu metabolosomes

Relatively little is known about the assembly of catabolic BMCs. This is due to the high degree of complexity associated with their formation, which is demonstrated by the involvement of 18-20 proteins in comparison to carboxysomes where 10-11 proteins are involved in the assembly of α-carboxysomes as in *H. neapolitanus* (Havemann; Bobik, 2003; Rae *et al.*, 2013). Furthermore, it appears that Pdu metabolosomes from *S. enterica* are more heterogeneous (120 ± 30 nm) in size and shape than their anabolic counterparts from *H. neapolitanus* (90 ± 10 nm), as evidenced in Figure 1.9 (Corchero; Cedano, 2011; Tocheva *et al.*, 2014). These features complicate the analysis of the structural properties of Pdu BMC structures.

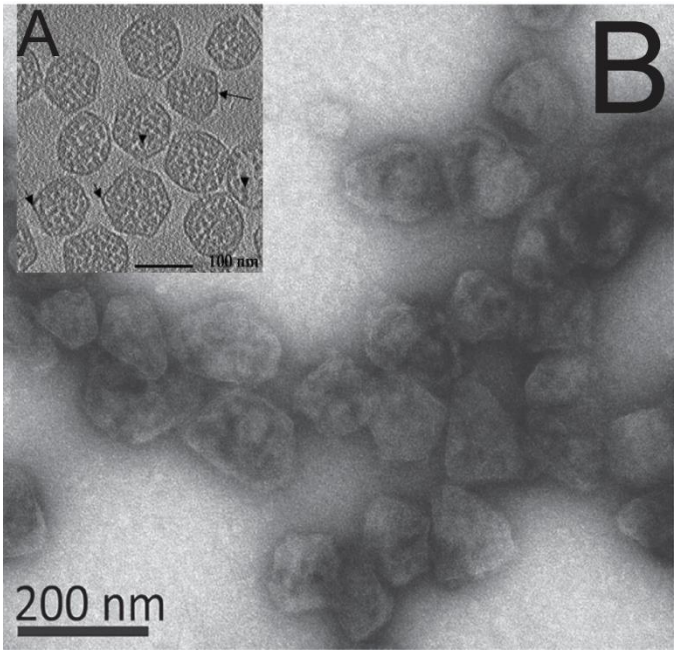

Figure 1.9. Isolated Pdu microcompartments. **A.** Central slice of α-carboxysomes in cryo-tomography (Schmid *et al.*, 2006). **B.** Isolated Pdu metabolosomes from *S. enterica* in negative stain TEM (Sinha *et al.*, 2012).

1.7. Work leading up to this project

1.7.1. The recombinant formation of BMCs in *E. coli*

The sequestration of metabolic processes is a desired feature for nano-biotechnological applications, for example, in the production of fine-chemicals including volatile or cytotoxic intermediates (Chessher *et al.*, 2015). One prerequisite for the application of BMCs in synthetic biology is the ability to form recombinant BMC structures. In this manner *E. coli* was empowered with the ability to form functional recombinant Pdu BMCs (rBMCs) from *C. freundii* (Parsons *et al.*, 2008). *E. coli* harbouring the *pdu* operon were able to metabolise 1,2-PD as determined by a McConkey agar plate. Furthermore, diol dehydratase assays were conducted to confirm the activity for 1,2-PD degradation in crude cell lysates. In addition to this gain of function, *E. coli* was shown to form polygonal Pdu metabolosomes (108-

123 nm diameter) with a similar size to *S. enterica* as determined by negative stain TEM and SuperSTEM (aberration corrected non-contrast electron microscope) of isolated structures. More recently, the genetic information for α-carboxysome formation from *H. neapolitanus* was transferred to *E. coli* to study the assembly of recombinant carboxysomes (Bonacci *et al.*, 2012). The recombinant formation of α-carboxysomes and Pdu BMCs suggest that BMC formation is a tractable system, which can assist the analysis of structure and function of BMCs. However, the recombinant BMCs have not been properly compared to native BMCs from the host organism (*C. freundii* or *H. neapolitanus*).

1.7.2. The recombinant formation of empty Pdu based microcompartments

The potential biotechnological application of BMCs for synthetic biology requires stripping the BMC of its internal cargo and to reintroduce non-native metabolic pathways. To achieve this, an artificial operon harbouring only the Pdu BMC shell protein genes (*pduA-B-J-K-N-U-T*, A-T) was constructed (Parsons *et al.*, 2010a). The expression of all BMC shell proteins led to the formation of so called "empty microcompartments" (eBMCs). These empty BMCs were able to form in the absence of any metabolic enzymes or enzymes for Ado-B_{12} reactivation. Furthermore, the reduction of Pdu BMC shell protein genes from A-T to A-U or A-N did not disrupt BMC shell assembly. The ability of such eBMC (A-U) structures to recruit pathway enzymes was demonstrated by fusing GFP to the C-terminus of PduC, PduD and PduP, which resulted in the regio-specific targeting of GFP-fusions to the eBMC. The study by Parsons *et al.* provided the ground-work to construct a BMC based bioreactor, forming a proteinaceous encasement by the coordinated expression of Pdu BMC shell proteins without characterising the assembly itself (Lawrence *et al.*, 2014).

1.7.3. The construction of a BMC based ethanol bioreactor

To utilise the capability of eBMCs for metabolic engineering, metabolic enzymes for ethanol formation were targeted to the stripped eBMC shell (A-U) (Parsons *et al.*, 2010a; Lawrence *et al.*, 2014). To allow this the N-terminus of pyruvate decarboxylase (Pdc) was labelled with the PduP18 (18 amino acids of the N-terminus of PduP) targeting sequence and the alcohol dehydrogenase (Adh) was fused onto the C terminus of PduD18 or PduD60 (18 or 60 amino acids of the N-terminus of PduD; Section 1.6.2.1). Both genes (Adh and Pdc) were cloned from *Zymomonas mobilis*. The resultant strain, containing PduA-U plus PduP18-Pdc and PduD60-Adh, allowed the formation of ethanol bioreactors that showed increased production level of ethanol. Isolated ethanol bioreactors were tested for the coupled enzymatic activity for ethanol production and showed a 20 fold increase in activity of isolated eBMCs in comparison to crude lysate samples. The formation of an ethanol bioreactor based on Pdu BMCs provides a proof of concept study, showing that BMCs in general can be manipulated to sequester relevant industrial metabolic pathways.

1.8. Aims and Objectives

Despite recent advances in the application of Pdu BMC based eBMCs, structural and functional properties of wild type, rBMC and eBMC variants have not been reported.

Therefore, this study aims to compare the structure of eBMCs and rBMCs to their wild type compartments through the application of TEM and AFM. Initially, purification protocols were developed and compared for eBMC, rBMC and wild type structures to allow the quantitative analysis of BMC shell building blocks by a proteomic approach consisting of 2D-PAGE, MALDI TOF-TOF and densitometric measurements. In part, the biophysical properties of the BMCs were compared in order to detect any differences in terms of size (TEM and AFM) and height (AFM). The application of AFM has yielded in a more detailed analysis of mechanical properties. A TEM technique was applied, that permitted the study of the internal organisation of all the various Pdu BMC structures (eBMC, rBMC and wild type). In addition to these proteomic and biophysical studies, LC-MS based methods were developed to study qualitative and quantitative effects of cobalamin in presence of BMCs (*in vivo* and *in vitro*). For visualisation in wide field microscopy, fluorescent B_{12}-analogues needed to be generated, purified and characterised.

Chapter 2

Materials and methods

2.1. Materials

Most chemicals and antibiotics were purchased from Sigma-Aldrich Ltd. Other materials were purchased from manufacturers as follows: IPTG and ampicillin from Melford Laboratories Ltd; chelating fast flow Sepharose, disposable from GE Healthcare; QIAprep® Spin Miniprep Kit from Qiagen, restriction enzymes were purchased from Promega and from New England Biolabs Inc.; tryptone, yeast extract and bacterial agar from Oxoid Ltd.

2.2. Bacterial strains

Table 2.1. Bacterial strains

Organism	Strain	Genotype and/or phenotype	Reference
E. coli	BL21 (DE3)	F - ompT hsdSB (rB - , mB -) gal dcm (DE3)	Novagen
E. coli	BL21 (DE3) pLysS	F - ompT hsdSB (rB - , mB -) gal dcm (DE3) pLysS (CmR)	Novagen
E. coli	DH5-α	F - φ80 lacZΔM15 Δ(lacZYA-argF) U169 recA1 endA1 hsdR17 (rK-,mK+) phoA supE44 λ- thi- 1 gyrA96 relA1	Invitrogen
C. freundii	*C. freundii* ballerup 7851	wild type (wt)	Sanger Institute
S. typhimurium	*S. typhimurium* (AR2680)	*cbiB* and *metE* mutant, blocking synthesis of coenzyme-B_{12} (*cbiB*) and methionine (*metE*), indicator strain for B_{12} quantification	(Raux *et al.*, 1996)

2.3. Plasmids

Table 2.2. Plasmid list

Name	Plasmid	Description	Reference or source
pET3a	pET3a	Overproduction vector with T7 promoter, Amp^r	Novagen
pET14b	pET14b	Overproduction N-terminal His_6tag fusion protein vector with T7 promoter, Amp^r	Novagen
pLysS	pLysS	Overproduction vector with T7 promoter, Cam^r	Promega
btuB	pLysS-*btuB*	Overproduction of the outer transmembrane cobalamin transporter	Provided by Dr. Evelyne Deery
btuB	pET3a-*btuB*	Overproduction of the outer transmembrane cobalamin transporter	Provided by Dr. Evelyne Deery
cobN	pET14b-*cobN*	Overproduction of N-terminal His_6tag CobN	Provided by Dr. Evelyne Deery
cobR	pET14b-*cobR*	Overproduction of N-terminal His_6tag CobR	Provided by Dr. Evelyne Deery
A-U	pLysS-ABJKNU	Formation of empty Pdu microcompartments	(Parsons *et al.*,2010a)
mCherryA-U	pLysS-mCherryABJKNU	Formation of fluorescently labelled empty Pdu microcompartments	(Parsons *et al.*,2010a)
CFPA-U	pET3a-CFPABJKNU	Formation of fluorescently labelled empty Pdu microcompartments	provided by Dr. Stefanie Frank
A-T	pET3a-ABJKNUT	Formation of empty Pdu microcompartments including the shell protein PduT	(Parsons *et al.*,2010a)
rBMC (A-X)	pET14b-Pdu65	Production of fully functional rBMCs	(Parsons *et al.*,2008)

2.4. Solutions and buffers

2.4.1. Media and solutions for bacterial work

Luria-Bertani (LB) broth	Tryptone	10	g
	Yeast extract	5	g
	NaCl	5	g

Made up to 1 L with dH_2O and autoclaved.

2YT broth	Tryptone	16	g
	Yeast extract	10	g
	NaCl	5	g

Made up to 1 L with dH_2O and autoclaved.

Luria-Bertani agar

15 g of bacterial agar were added to 1 L LB broth before autoclaving.

10x M9 salts:	Na_2HPO_4	60	g
	KH_2PO_4	30	g
	NH_4Cl	10	g
	NaCl	5	g

Made up to 1 L with dH_2O and autoclaved

Mg^{2+} stock	$MgSO_4(H_2O)_7$	1	M

Brought up to final volume with dH_2O and autoclaved.

50x NCE: Chemicals were dissolved one at a time in the order listed below, allowing each to dissolve completely. Heated 330 mL dH_2O on stirring block (not boiled).

KH_2PO_4	197	g
$K_2HPO_4 \cdot 3H_2O$	323	g
$NaNH_4HPO_4 \cdot 4H_2O$	175	g

Brought to 1 L with dH_2O and autoclaved.

NCE liquid medium:

50x NCE	20	mL
1 M $MgSO_4$	1	mL

Sterile 1,2-PD and carbon source were added and the solution brought to 1 L with dH_2O.

2.4.2. Antibiotics and additives

Table 2.3. Antibiotics and additives

Antibiotics/Additives	Stock concentration	Final concentration
Ampicillin	100 mg mL^{-1} in EtOH	100 µg mL^{-1}
IPTG	1 M in dH_2O	100 µM
Chloramphenicol	34 mg mL^{-1} in EtOH	34 µg mL^{-1}

2.4.3. Solutions for DNA work

TAE buffer:	Tris-HCl, pH 8.0	10 mM
	EDTA, pH 8.0	1 mM
6x DNA loading buffer	Bromophenol blue (w/v)	0.25%
	Glycerol (v/v)	50%
	TAE buffer (v/v)	50%

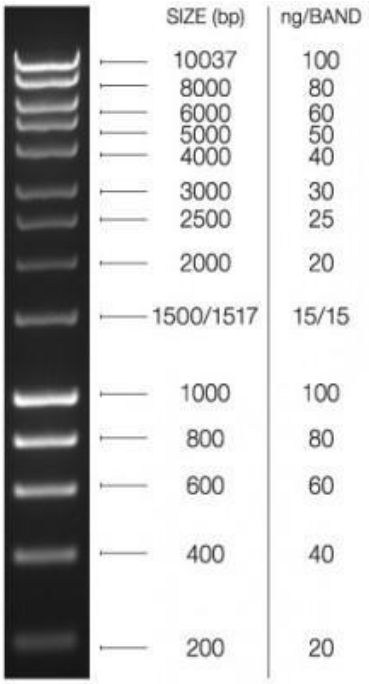

Figure 2.1. Hyperladder 1 kb (Bioline): 5 µL applied to a 1% (w/v) TBE/agarose gel visualised using ethidium bromide.

2.4.4. Solutions used for protein work

2.4.4.1. Solutions for BMC purification (B-PER™)

Buffer A	Tris-HCl, pH 8.0	50	mM
	KCl	500	mM
	$MgCl_2$	12.5	mM
Buffer B	Tris-HCl, pH 8.0	50	mM
	KCl	50	mM
	$MgCl_2$	5	mM

2.4.4.2. Solutions for eBMC purification (Y-PER™):

Resuspension buffer	Tris-HCl, pH 8.0	20	mM
	NaCl	20	mM

2.4.4.3. Solutions for protein polyacrylamide gel electrophoresis.

10x running buffer:	Tris	30	gL^{-1}
	Glycine	144	gL^{-1}

1% (w/v) SDS added to 1x running buffer for SDS gels

2x SDS sample buffer	0.5 M Tris-HCl, pH 6.8	6.0	mL
	Glycerol	4.8	mL
	SDS 10% (w/v)	9.6	mL
	Bromophenol blue	1.2	mL
	dH_2O	24	mL

14 µL β-mercaptoethanol added per mL 2x SDS sample buffer.

Denaturing molecular weight marker- Dalton VII (Sigma):

Protein molecular weight (kDa): 66, 45, 36, 29, 20.1, 14.2

Denaturing molecular weight marker- Prestained protein marker, broad range (New England BioLabs); Molecular weight (kDa): 175, 80, 58, 46, 30, 25, 17 and 7

Denaturing molecular weight marker- Blue protein standard, broad range (New England BioLabs): Molecular weight (kDa): 190, 135, 100, 75, 58, 46, 32, 25, 22, 17, 11

Coomassie blue stain:	TCA 100% (w/v)	250	mL
	Coomassie blue R250	0.60	g
	SDS	0.10	g
	Tris-HCl	0.25	g
	Glycine	0.15	g

Made up to 500 mL with dH_2O

Table 2.4. Gel composition for SDS-PAGE and 2D-PAGE

SDS gels				
Running gels	**12.5%**	**15%**	**Stacking gel**	**5%**
dH_2O (mL)	3.4	2.2	**dH_2O (mL)**	3.4
30% Acrylamide (mL) Acryl/Bis™ 29:1	6.3	7.5	**30% Acrylamide (mL) Acryl/Bis™ 29:1**	1.5
1.5 M Tris-HCl pH 8.8 (mL)	3.8	3.8	**0.5 M Tris-HCl pH 6.8 (mL)**	1.9
10% (w/v) SDS (mL)	1.5	1.5	**10% (w/v) SDS (mL)**	0.75
10% (w/v) APS (mL)	0.15	0.15	**10% (w/v) APS (mL)**	0.075
TEMED (mL)	0.01	0.01	**TEMED (mL)**	0.01

2.4.4.4. Solutions for two dimensional polyacrylamide gel electrophoresis (2D-PAGE)

2D lysis buffer:	Urea	600	g/L
	CHAPS	20	g/L
	DTT	10	g/L
	Pharmalyte (pH 3-10)	20	mL/L
Bromophenol blue stock solution	Bromophenol blue	100	mg
	Trizma base	60	mg

Made up to 10 mL with ddH_2O

Agarose sealing solution:

1 *x* Laemmli SDS electrophoresis buffer	100	mL
Agarose 0.5% (w/v)	0.5	g
1% bromophenol blue stock solution	200	µL

SDS equilibration buffer:

Urea	360.5	g/L
Tris-HCl, pH 8.8	50	mL/L
Glycerol	344	mL/L

SDS		20	g
1% (w/v) Bromophenol blue		2	mL
Fix solution:	Ethanol	300	mL
	Acetic acid	100	mL

Made up to 1 L with ddH_2O

2.4.4.5. Solutions for western blot analysis

Transfer Buffer	Trizma base	25	mM
	Glycine	200	mM
	Methanol	20%	(v/v)
Phosphate buffered saline-PBS	NaCl	140	mM
	KCl	3	mM
	Na_2HPO_4	10	mM
	K_2HPO_4	2	mM
Tris-NaCl pH 7.5 wash buffer	NaCl	150	mM
	Trizma base	50	mM

The components were mixed and the pH was adjusted to pH 7.5 before adjusting to the final volume.

2.4.4.6. Solutions for MALDI-TOF and MALDI-TOF-TOF

Colloidal coomassie blue stain:	Ammonium sulphate	1.3	M
	Methanol	34%	(v/v)
	Coomassie blue G250	1	g/L
Matrix solution:	HCCA saturated in TA30		

2.4.5. Solutions for electron microscopy experiments

Fixing solution	1% (v/v) glutaraldehyde in PBS

Osmium tetroxide 2x stock	2% (w/v) in dH_2O
Uranyl acetate	5% (w/v) in dH_2O
Lead Citrate	0.1% (w/v) in dH_2O

2.4.6. Solutions for tetrapyrrole HPLC and HPLC-MS

Solution A	Trifluoroacetic acid (v/v)	0.1% (v/v)
Solution B	Acetonitrile	100% (v/v)

All solutions were filtered prior to use.

2.5. B_{12}-analogue synthesis and purification

2.5.1. Synthesis and purification of the upper ligand analog Texas-Red-B_{12}

Texas Red™ N-hydroxysuccinimidyl ester (Life Technologies, 0.026 mmol) was added to a slurry of β-(3-aminopropyl) cobalamin (provided by Dr. Andrew Lawrence, 0.021 mmol), DMF (0.4 mL) and N,N-diisopropylethylamine (DIPEA) (0.05 mmol). The reaction was stirred for 1.5 h, after which it was judged complete by HPLC analysis. MeOH (0.5 mL) was added to the reaction mixture and the solution was added to rapidly stirring 1:1 dichloromethane/diethyl ether (50 mL). The purple solid was triturated with 2×3 mL each of dichloromethane, acetone, and finally diethyl ether. The compound was dried *in vacuo.* Samples were resolved on an ACE 5AQ column (4.6 *x* 250 mm; Advanced Chromatography Technologies) attached to an Agilent 1100 series HPLC equipped with diode array. The column was developed with a binary gradient at a flow rate of 1.0 mL per min. The LC gradient corresponds to Section 2.8.5. Purified fractions were dried *in vacuo* and analysed by analytical LC-MS (Section 2.8.5) (Smeltzer *et al.*, 2001).

2.5.2. Synthesis and purification of lower loop B_{12} analogues

2.5.2.1. Ethylene Diamine-B_{12} synthesis

Solid 1,1`-carbonyldiimidazole (CDI, 260 mg) was added to cyanocobalamin (1.0 g, 0.74 mmol) previously dissolved in dimethyl sulfoxide (12 mL) at 30°C, and the mixture stirred for 25 min. Ethylene Diamine (2.7 mmol) was added in one portion, and the mixture stirred for 24 h at room temperature. The mixture was poured into ethyl acetate (30 mL) and left to stand. The precipitate was filtered, and the red solid was washed with acetone. The

product was dried *in vacuo.* The reaction mix was analysed by analytical LC-MS (Section 2.8.5) (McEwan *et al.*, 1999).

2.5.2.2. Synthesis of Oregon-Green-B_{12} and Bodipy-TR-X B_{12}

Oregon-Green or Bodipy-TR-X N-hydroxysuccinimidyl ester (Life Technologies, 0.026 mmol) were added to a slurry of Ethylene Diamine-B_{12} (Section 2.5.2.1), DMF (0.4 mL) and N,N-diisopropylethylamine (DIPEA) (0.05 mmol). The reaction was stirred for 1.5 h, after which it was judged complete by HPLC analysis. MeOH (0.5 mL) was added to the reaction mixture and the solution was added to rapidly stirring 1:1 dichloromethane/diethyl ether (50 mL). The (orange or purple) solid was triturated with 2 *x* 3 mL each of dichloromethane, acetone, and finally diethyl ether. The products were dried *in vacuo* and the structure confirmed by analytical LC-MS (Section 2.8.5) (McEwan *et al.*, 1999).

2.5.2.3. Purification of Oregon-Green-B_{12} and Bodipy-TR-X B_{12}

Samples were resolved on an ACE 5AQ column (4.6 x 250 mm; Advanced Chromatography Technologies) attached to an Agilent 1100 series HPLC equipped with diode array. The column was developed with a binary gradient at a flow rate of 1.0 mL per min. Solvent A was 0.1% (v/v) TFA and solvent B was acetonitrile. The column was equilibrated with 0% B. Following sample injection, the concentration of B was increased from 5 min to 20 min to 40%, increased to 60% at 35 min and 100% at 45 min where it was held for 5 min before returning to starting conditions. The total length of each run was 60 min. Data were processed using Compass™ Data Analysis (Bruker). Purified fractions were dried *in vacuo.* Purified samples were analysed by analytical LC-MS (Section 2.8.5).

2.6. Microbiological techniques

2.6.1. Sterilisation

Unless stated otherwise medim and buffers were sterilised for 15 min at 121°C and 1 bar pressure in an autoclave. Temperature sensitive substances were filter sterilised (0.2 µm pore size).

2.6.2. Storage of bacteria

For long-term storage of bacteria, glycerol stocks were prepared. Glycerol was added to an overnight bacterial culture to a final concentration of 25% (v/v). The culture was then incubated on ice for 30 min before storage at -80°C.

2.6.3. Plate cultures

Bacteria were usually streaked directly from a glycerol stock onto agar plates and antibiotics or vitamin-B_{12} was added where required. The agar plates were incubated overnight at 37°C.

2.6.4. Liquid cultures

Liquid cultures were inoculated with a single colony from an agar plate culture. The medium was supplemented with antibiotics. Liquid cultures were shaken at ≈ 160 rpm in baffled flasks at 37°C. After induction cultures were incubated at 19°C at ≈ 160 rpm.

2.6.5. Preparation of competent cells

Competent *E. coli* cells were prepared based on a method previously described (Green; Sambrook, 2012). A bacterial overnight starter culture derived from a single colony was inoculated into 10 mL fresh LB broth and grown to an OD_{600} of 0.3. The cells were cooled on ice for 15 min and centrifuged at 850 *x g* at 4°C. The pellets were gently resusupended in 25 mL of ice-cold 0.1 M $CaCl_2$ and incubated on ice for 30 min. Cells were collected again by centrifugation and resuspended in 0.25 mL of 0.1 M $CaCl_2$ containing 25% (v/v) glycerol. Aliquots of 30 µL were frozen in dry ice and stored at -80°C.

2.6.6. Transformation of *E. coli* competent cells

Competent cells were defrosted on ice for 10 min before adding 0.5 µg plasmid DNA. The mixture was incubated on ice for 15 min and then heat-shocked by incubation at 42°C for 50 sec before rapid transfer to ice and incubation for 2 min. After the addition of 250 µL LB medium, the cells were incubated at 37°C for 60 min to allow antibiotic resistance expression. The mixture was then spread on a LB agar plate containing the required antibiotics and incubated at 37°C overnight.

2.6.7. Recombinant microcompartment/metabolosome production in *E. coli*

The *E. coli* strains BL21 (DE3) and BL21 (DE3) pLysS were transformed with a vector containing the gene(s) of interest cloned in frame (Section 2.6.6). The recombinant strains (rBMC, A-T, A-U, mA-U and CFPA-U) was grown in 2YT (200 mL in baffled flasks) with ampicillin (and chloramphenicol for pLysS strain) at 37°C and shaken at ≈160 rpm until the culture reached an OD_{600} of approximately 0.6. Protein production was induced with 0.1 µM IPTG overnight at 19°C. The cells were collected by centrifugation at 3,500 *x g* for 20 min at 4°C. The pellet was directly used for microcompartment and metabolosome purification (Section 2.6.11 and 2.6.12).

2.6.8. Culture of *Citrobacter freundii* ballerup 7851

400 mL of NCE medium containing 10 mL 20% (v/v) succinate, 0.5% (v/v) 1,2-PD and 400 mM $MgSO_4$ were inoculated with 2 mL overnight culture and incubated at 37°C, and shaken at ≈160 rpm for 8-9 h. The liquid culture was incubated overnight at 19°C at 160 rpm, after adding 0.5% (v/v) 1,2-PD.

2.6.9. Lysis of cells using sonication

Harvested cells were lysed by sonication using a Sonics Vibracell Unltrasonic processor, with an output wattage of between 20 and 30 in 30 sec bursts with 30 sec breaks repeated six times. The sonicated cells were centrifuged at 35,000 *x g* for 20 min at 4°C to remove cell debris

2.6.10. Cobyric acid quantitative bioassay

S. typhimurium (*cysG* and *metE* knock-out mutants, AR2680) was used as the indicator strain to estimate concentration of cobyric acid and later intermediates of various samples (Raux *et al.*, 1996). A *cysG* mutation blocks the B_{12} pathway between uroporphyrinogen III and precorrin-2, but intermediates before cobyric acid cannot be taken up by *Samonella*. Therefore, the first intermediate, which can be detected, is cobyric acid. The bioassay plates containing the indicator strain were prepared as follows: bacterial growth was scraped from an overnight minimum medium plate containing methionine (50 mg/L) and cysteine (50 mg/L) [cysteine only for AR3612 due to the *cysG* mutation blocking the cysteine synthesis], washed three times with 0.9% (w/v) NaCl. The cells were finally mixed with 300 mL of minimum medium agar previously cooled to 47/48°C. 10 µL sample droplets were placed on the surface of bioassay plates and the plates were incubated for 18 h at 37˚C. The extent of *S. typhimurium* mutant growth (in the bioassay plate agar) surrounding the sample

application point is dependent upon the amount of cobyric acid present in the sample. Synthesised vitamin-B_{12}-analogues were compared in equal concentrations to vitamin-B_{12} (2 pmol).

2.6.11. Purification of empty Pdu microcompartments

Cells were harvested by centrifugation for 10 min at 4°C at 2683 *x g* (Lawrence *et al.*, 2014). Wet cell pellets (1 g) were re-suspended in 10 mL Y-PER™ Plus (Pierce) supplemented with one tablet of Complete Protease Inhibitor Cocktail (Roche) and 1250 units Benzonase® nuclease (5 µL per 10 mL Y-PER™). The lysate was incubated for 3 h at room temperature and gently agitated (shaking platform). The lysate was pelleted for 5 min at 11,300 *x g* (Beckman Coulter, rotor JA 25.50, 4°C). The pellet was re-suspended in 2 mL 20 mM Tris-HCl, pH 8.0, 20 mM NaCl. The suspension was centrifuged at 4°C for 5 min at 11,000 *x g* (Multispeed Refrigerated Centrifuge, ALC PK121R). The NaCl concentration of supernatant 2 was raised to 80 mM by addition of 5 M NaCl (24 µL of 5 M NaCl in 2 mL supernatant 2). Supernatant 2 was then centrifuged at 4°C for 5 min at 11,000 *x g.* Pellet 3 (contained the microcompartments) was re-suspended in 1 mL of 20 mM Tris-HCl, pH 8.0 and clarified by centrifugation (4°C for 5 min at 11,000 *x g*).

2.6.12. Purification of Pdu metabolosomes

Cells were harvested by centrifugation and washed twice with 40 mL of buffer A. Cells (1 g wet weight) were resuspended in a mixture of 10 mL of buffer and 15 mL of B-PER-II, 25 mg of lysozyme, and 5 µL Benzonase (Sinha *et al.*, 2012). The suspension was incubated at room temperature shaking at 60 rpm for 30 min. Cell debris was removed by centrifugation twice at 12,000 *x g* (Beckman Coulter, rotor JA 25.50, 4°C) for 5 min at 4°C, and BMCs were spun down at 20,000 *x g* for 20 min at 4°C. The pellet was washed once with a mixture of 4 mL of buffer A and 6 mL of B-PER-II, and then resuspended in 0.5 mL of buffer B. Remaining cell debris was removed by centrifugation at 12,000 *x g* for 5 min at 4°C and performed three times. Purified metabolosomes were stored at 4°C until used.

2.7. Molecular Biology

2.7.1. Electrophoresis of DNA

DNA fragments were separated by agarose gel electrophoresis.

2.7.2. Agarose gel

The agarose gel percentage was chosen according to the size of the DNA fragments to be separated [0.7-1.5% (w/v) agarose in TAE buffer]. Routinely, a 1% (w/v) agarose gel was used. Agarose gels were set with the appropriate amount of agarose in 1 *x* TAE buffer with the addition of ethidium bromide to a final concentration of 0.5 µg mL^{-1}. The DNA samples containing 20% (v/v) DNA loading buffer were loaded into the agarose gel wells and electrophoresis was carried out at 70 V for approximately 1 h using a SubCell GT electrophoresis tank (BioRad) connected to a Power PAC 300 power supply (BioRad).

2.7.3. Visualisation of DNA

Ethidium bromide is a fluorescent dye that intercalates between DNA base pairs. UV radiation (312 nm) is absorbed by the ethidium bromide and re-emitted at 590 nm in the red orange wavelength range. This allows visualisation of the DNA using a UV transilluminator.

2.7.4. Isolation of plasmid DNA

A QIAprep® Miniprep Kit (Qiagen) was used for the purification of plasmid DNA as described in the handbook according to the protocol for using a microcentrifuge.

2.7.5. Restriction enzyme digest

Plasmid DNA was digested using the relevant enzymes (10 U μL^{-1}) and the optimal buffer chosen according to either the Promega or New England Biolabs information provided. The reactions were incubated for 2 h at the temperature required by the restriction enzyme before being subjected to electrophoresis.

Table 2.5. Restriction enzyme digest

Component	Single digest	Double digest

dH_2O	4 µL	4 µL
Restriction enzyme 1	1 µL	0.5 µL
Restriction enzyme 2	-	0.5 µL
10x buffer	1 µL	1 µL
Plasmid/PCR	4 µL	4 µL

2.8. Biochemistry

2.8.1. Bradford protein assay

The Bradford assay relies on the dye Coomassie brilliant blue G-250 binding to proteins, most readily to arginyl and aromatic residues, causing a shift in the absorbance maximum of the dye from the red cationic form (470-650 nm) to the blue anionic form (590-620 nm) in the presence of protein (Bradford, 1976). Therefore, the quantity of the protein can be estimated by measuring the amount of dye in the blue form at 595 nm. The protein assay dye from BioRad was added to diluted protein solution, and the reaction was carried out as described in the instructions. The reaction was left at room temperature for 10-30 min and the OD_{595} was measured in duplicates. Simultaneously, a standard curve with bovine serum albumin (0, 5, 10, 15, 20 and 25 mg mL^{-1}) was generated.

2.8.2. Polyacrylamide gel electrophoresis

2.8.2.1. SDS-PAGE

The composition of the gel, buffers and stain were previously described in Section 2.4.4.3. Polyacrylamide gels were run as previously described (Laemmli, 1970). The sample was denatured by 1:1 addition of SDS sample buffer and boiling for 5 min. Between 5 and 20 µL of denatured sample was loaded into each well and 5 to 10 µL molecular mass marker was run on each gel to estimate the relative molecular mass of the protein of interest and was performed at a constant voltage of 200 V using an Atta Dual Mini Slab AE6450 electrophoresis apparatus and an Atto Mini Power electrophoresis power supply SJ1082 (GRI Ltd.). The gel was stained with coomassie blue stain or colloidal stain for MALDI MS-MS and destained using ddH_2O.

2.8.2.2. Two dimensional polyacrylamide gel electrophoresis

Purified microcompartment fractions were separated by two-dimensional (2D) denaturing electrophoresis that employed isoelectric focusing (IEF) and SDS-PAGE (Rasband, 1997). Purified microcompartment and metabolosome pellets were resuspended in 2D-PAGE lysis buffer. Protein concentration was quantified using Bradford assay and the sample standardised to contain 160 µg of protein in 125 µL for 7 cm IPG (Immobilised pH gradient) strips. Prior to running the first dimension, grains of bromophenol blue were added to the sample and subsequently the sample was applied to an IEF boat. The IEF dry strip (GE Healthcare pH 3-10 nonlinear 7 cm) was placed on top before being overlayed with 0.6 mL of mineral oil. The samples were then focused on a Pharmacia Biotech IPGphor IPG runner with the conditions stated in Table 2.6.

Table 2.6. Isoelectric Focussing parameters

IEF settings:			
Rehydrate	0 h at 20°C		
IEF Parameters	20°C		50 µA/strip
S1	Step-n-hold		
	30 V		14 h
S2	Gradient		
	200 V		0.45 h
S3	Step-n-hold		
	500 V		0.45 h
S4	Step-n-hold		
	1000 V		0.45 h
S5	Gradient		
	8000 V		1.00 h
S6	Step-n-hold		
	8000 V		9.00 h
Stop			
S6	20°C	49	µA 1W
4109 V		2934 Vhs	
Total: 8092 Vhr			

Following focussing, the strips were removed from the boats, rinsed with dH_2O and placed in 20 mL of SDS equilibration buffer containing 200 mg of DTT for 20 min. The strips were rinsed with dH_2O followed by 20 mL of the equilibration buffer containing 500 mg of iodoacetamide. The strip was then placed onto a 15% SDS running gel, gaps sealed with the agarose sealing solution before running for 2 h at 180 V. The gel was then removed, fixed and stained with colloidal coomassie blue for analysis. Gel images were analysed in ImageJ v1.48 and protein spots picked for MALDI MS-MS (Section 2.8.5).

2.8.3. Western blot analysis

Proteins separated on a denaturing polyacrylamide gel (Sections 2.4.4.3 and 2.8.2) were transferred onto Hybond-P, hydrophobic polyvinylidene difluoride (PVDF) membrane from Amersham Biosciences (Towbin *et al.*, 1979). The PVDF membrane was briefly soaked in 100% (v/v) methanol before immersing in transfer buffer. The polyacrylamide gel, PVDF membrane, blotting paper and gauze pads were all soaked in transfer buffer for 10 min before the blot was constructed. The 'sandwich' was placed in the Western Blot transfer tank (BioRad) along with an ice block and filled with cold transfer buffer before being electrophoresed at 100 V for 75 min using a BioRad power pac 300. Once electrophoresis was complete the PVDF membrane was incubated with 5% (w/v) non-fat dry milk in PBS for at least 2 h to block non-specific sites before probing with antibodies. All solutions used for any Western blotting method used can be found in Section 2.4.4.5. To probe for His-tagged recombinant proteins, the His-tag monoclonal antibody (Ab) obtained from Novagen is used as the primary Ab. The epitope for this Ab are five consecutive histidine residues (HHHHH), and binding is not dependent on sequence context. The secondary Ab used is the goat anti-mouse IgG alkaline phosphatase conjugate, also from Novagen. Once the membrane had been incubated in the 5% (w/v) milk solution in PBS, it was rinsed briefly three times with PBS and incubated for 1 to 2 hours at 4°C with the primary Ab at a working dilution of 1:1,000. After thoroughly rinsing the membrane three times with PBS and twice with Tris-NaCl wash buffer, the membrane was incubated with the secondary Ab for 1 h at room temperature at a working dilution of 1:5,000. The membrane was again washed thoroughly with Tris-NaCl wash buffer before proteins were detected by incubating with Sigma Fast™ BCIP/NBT buffered substrate reagent, containing 0.15 mg/ml BCIP, 0.30 mg/ml NBT, 100 mM Tris buffer and 5 mM $MgCl_2$.

Alkaline Phosphatase + BCIP BCI → BCI + PO_4, pH 9.5

BCI + NBT → insoluble, blue colour

The colour was allowed to develop and the reaction stopped by immersing the membrane in water. The blots were stored dry.

2.8.4. MALDI-TOF (MALDI MS) and MALDI TOF-TOF (MALDI MS-MS)

2.8.4.1. Reduction and desalting

To identify proteins, present within purified eBMCs, rBMCs and BMCs were subjected to SDS-PAGE or 2D-PAGE. The gel was removed from the running buffer and fixed with a PAGE fix solution for 1 h. The gel was stained with colloidal coomassie stain and individual protein bands/spots were excised and prepared for MALDI-TOF and MALDI-TOF-TOF as follows. Bands of interest were excised with a clean scalpel, cut into small squares (1 *x* 1 mm) and transferred to a microfuge tube. The gel pieces were then washed with 100 µL of 50 mM NH_4HCO_3/acetonitrile (1:1) for 15 min and the spun down to remove the liquid. The gel pieces were shrunk by the addition of 100 µL acetonitrile and left to stand for 15 min. The samples were then spun down and the liquid was removed before incubation at 56°C for 30 min in 50 µL of 10 mM DTT and 50 mM NH_4HCO_3. The gel pieces were centrifuged, the liquid removed and the samples shrunk briefly again in acetonitrile. The acetonitrile was

subsequently removed and the samples incubated in 55 mM iodoacetamide and 50 mM NH_4HCO_3 for 20 min in the dark. Iodoacetamide solution was removed and gel pieces were washed twice for 15 min in 50 mM NH_4HCO_3. The gel pieces were then shrunk again in acetonitrile and acetonitrile removed and the samples dried in a vacuum centrifuge.

2.8.4.2. In-gel digestion

The gel pieces were rehydrated in 20 µL digestion buffer (10 mM NH_4HCO_3, 10% acetonitrile) containing 10 ng/µL of trypsin at 4°C (on ice). After 30 min, the supernatant was removed and 10 µL of digestion buffer without trypsin was added to keep gel pieces wet during enzyme cleavage. Samples were left at 37°C overnight.

2.8.4.3. Extraction of peptides

5 µL of acetonitrile was added to each sample before sonication in an ultrasonic bath for 15 min. The supernatant was then removed and stored in a microfuge before the addition of 10 µL of 50% (v/v) acetonitrile with 5% (v/v) formic acid and another sonication for 15 minutes in an ultrasonic bath. The supernatant was removed and combined with the previous supernatant, and the samples were analysed by MALDI TOF and MALDI TOF-TOF on a Bruker Ultraflex machine.

2.8.4.4. MALDI-TOF-TOF

The sample (1 µL of the above peptide digest) was placed on the sample target (AnchorChip standard, 800 µm, Bruker) and dried (Alanen *et al.*, 2014). 0.5 µL of matrix solution was added and dried. The matrix was HCCA (α-CHCA, 0.7 $mgmL^{-1}$ in 85% (v/v) acetonitrile, 0.1% (v/v) TFA and 1 mM $NH_4H_2PO_4$) (Sigma-Aldrich). For external calibration in the protein mass range, Peptide Calibration Standard I (Bruker) was used. MALDI TOF MS and MALDI TOF-TOF MS-MS analysis was performed in the positive ion mode using a Bruker UltrafleXtreme**.** The spectra were obtained in reflector mode with an acceleration voltage of 25 kV and a pulse ion extraction time of 80 ns. The mass range for MS was generally between 700 and 3500 *m/z*. The number of laser shots summed in MS was 3500. The number of laser shots summed in MS-MS was 3000. The software FlexAnalysis (Bruker) was used for peak picking prior to using the standard Mascot search engine (Matrix Science Ltd). The peptide mass fingerprint was searched against the NCBI proteobacteria protein database.

2.8.5. Analytical HPLC-MS

For biological samples, protein was removed prior to analysis by HPLC-MS by heat (10 min at 90°C), centrifugation at 13,000 *x* rpm and acidification to 0.1% (v/v) TFA. Samples were resolved on an ACE 5AQ column (2.1 *x* 150 mm; Advanced Chromatography Technologies) attached to an Agilent 1100 series HPLC equipped with diode array detector and coupled to a micrOTOF-Q mass spectrometer (Bruker). The column was developed with a binary gradient at a flow rate of 0.2 mL per min. Solvent A was 0.1% (v/v) TFA and solvent B was

acetonitrile. For cobalamins and cobalamin derivatives the column was equilibrated with 0% B. Following sample injection, the concentration of B was increased from 5 min to 45 min to 100%, where it was held for 10 min before returning to starting conditions. The total length of each run was 70 min. Data were processed using Compass™ Data Analysis (Bruker).

2.9. Wide field fluorescence microscopy

Fluorescently labelled bioengineered Pdu microcompartments (mCherryA-U, CFPA-U and YpetA-U) were purified as described in Section 2.6.11. Purified microcompartments (15 µL) were added on glass slides and 1 µL [1 mM] of B_{12} fluorophore (Texas-Red, Oregon Green or Bodipy-TR-X) was added before imaging. The samples were then visualised using an Olympus IX81 microscope with PlanApo 150x OTIRFM-SP 1.49 NA lens mounted on ASI stage (Applied Scientific), and illuminated using LED light sources (Cairn Research Ltd) with appropriate filters (Chroma). Samples were visualized using aPrinceton ProEM 1024 back-thinned EMCCD camera (Princeton Instruments), and the system was controlled with Metamorph software (Molecular Devices). Each 3D-maximum projection of volume data was calculated from 15 *z*-plane images, each 0.2 µm apart, using Metamorph or Autoquant X software. Final figures were generated using Adobe Photoshop software.

2.10. Biophysical techniques

2.10.1. Transmission electron microscopy (TEM)

2.10.1.1. Dehydration and embedding

A 200 mL culture of *E. coli* (BL21(DE3) pLysS) producing microcompartments of interest was grown overnight at 37°C. The cells (15 mL) were harvested by centrifugation and resuspended in fixing solution and left for 1 h. The cells were subsequently pelleted and fixing solution removed. Traces of the fixing solution were then removed by washing the cells twice with PBS. The samples were then resuspended in the primary stain, 1% (w/v) osmium tetroxide, and incubated at room temperature for 1 h. The samples were washed twice with PBS prior to dehydration. This was accomplished by subjecting the sample to a solvent gradient (Table 2.7).

Table 2.7. Dehydration solvent gradient.

Composition	Solvent	Time (minutes)
70%	Ethanol	20
100%	Ethanol	20

100%	Ethanol	30
100%	Propylene oxide	30
100%	Propylene oxide	30
50:50	Embedding medium: propylene oxide	60
100%	Embedding medium	180

The embedding medium used was agar low viscosity resin. Components for a block of medium hardness are shown in Table 2.8. The samples were placed in 0.5 mL embedding tubes and centrifuged for 10 min at 4,000 *x g* to concentrate the cells to the tip, and incubated at 60°C overnight to polymerise.

Table 2.8. Embedding medium components.

Component	**Mass**
LV Resin	48.0 g
VH1 Hardener	16.0 g
VH2 Hardener	36 g
LV Accelerator	2.5 g

2.10.1.1. Sectioning and visualisation of samples

Specimens were thin sectioned with a diamond knife on an RMC MT-6000-XL ultramicrotome. Sections were collected on copper grids and post-stained with 4.5% (w/v) uranyl acetate for 30 min at 60°C, and with 0.1% (v/v) and lead citrate for 10 min at room temperature. Sections were then visualised and photographed with a CEM 902 transmission electron microscope (Zeiss CEM 902).

2.10.1.2. Sample preparation of purified microcompartments for transmission electron microscopy

For EM analysis 15 µL of purified microcompartments were mounted onto Formvar, carbon coated 400 mesh copper grids for 2 min, followed by the addition of 15 µL of 2.5% (v/v) glutaraldehyde in PBS for 2 min. The grids were washed three times in 15 µL drops of 2.5% (v/v) glutaraldehyde in PBS and then three times in dH_2O. Finally, the grids were dried and stained with 2% (w/v) aqueous uranyl acetate. Grids were analysed at zero-loss bright field mode in an energy-filtered transmission electron microscope (Zeiss CEM 902).

2.10.2. Atomic force microscopy

2.10.2.1. Sample preparation for AFM

For semi-dry AFM, purified microcompartment samples were deposited onto freshly cleaved MICA surfaces for 5 min. Microcompartments were fixed using 2.5% (v/v) glutaraldehyde in PBS for 5 min. The surface was washed three times with 1 mL sterile filtered deionised H_2O and dried under a gentle stream of N_2 gas. Images were collected in air using Bruker Multimode 8 scanning probe microscope (Nano Inc.) and ScanAsyst air cantilever probes (Nano Inc.).

2.10.2.2. High resolution imaging

A nominal spring constant of 0.4 N/m was used. Height images of 4096 *x* 4096 pixels in size, covering surface areas of 10 *x* 10 µm to 20 *x* 20 µm were acquired at 20°C. Sample tilt and scanner bow were reduced using NanoScope1.40 (Nano Inc.) as described previously (Lawrence *et al.*, 2014). Images were analysed using ImageJ 1.48v (Rasband, 1997) or NanoScope 1.40 (Bruker). Size distribution measurements of TEM and AFM images were conducted using ImageJ v1.48. Areas were measured in ImageJ v1.48. Diameters were calculated presuming microcompartments have circular shapes. Peak height information of 125 single particles for each construct were obtained using NanoScope 1.40. Anova *post hoc* tests (Scheffe) were performed on all obtained data sets.

2.10.2.3. Nano-mechanical measurements

Deformation control experiment: spring constant and deflection sensitivity were estimated using a thermal tune procedure (for more information, see the user's guide of Nanoscope software 6.13). Tip geometry was estimated using an absolute method on a titanium roughness surface to scan the surface and Nanoscope 1.40 to qualify the tip geometry according to the image. 20 particles each were analysed on their change of height, reduced DMT modulus and deformation using NanoScope 1.40.

2.10.2.4. In-solution AFM

Samples were prepared on HOPG surfaces as described in Section 2.10.2.1 and rehydrated. Height images of 1024 *x* 1024 pixels in size, covering surface areas of 5 *x* 5 µm were acquired at 20°C using ScanAsyst probes for in-solution and automated settings.

Chapter 3

A proteomic comparison of wild type *C. freundii* Pdu BMCs to recombinant Pdu variants produced in *E. coli*

3.1. Introduction

The outer shell of BMCs is composed from a set of specific proteins that house a recognisable protein fold called a BMC domain (Sections 1.3.1 and 1.5.9) (Frank *et al.*, 2013). The BMC fold allows the proteins to oligomerise into hexameric tiles. Some proteins contain two BMC domains and those oligomerise into trimeric tiles with a pseudohexameric symmetry. Hexameric and pseudohexameric tiles are proposed to compose the facets of the BMC.

In the Pdu metabolosome, hexameric tiles (pfam 00936) are thought to be formed by PduA, PduJ, PduK and PduU (Chowdhury *et al.*, 2014). Pseudohexameric tiles are formed by PduB, PduB` and PduT (pfam 00936). A related, but distinct, BMC fold is also found in the pentameric shell protein, PduN (pfam 03319), which is thought to form the vertices of the BMC structure. Therefore, the shell protein composition plays a defining role in the assembly and properties of the organelle, affecting both the outward-facing surface of the assembly as well as the internal environment. Moreover, all shell protein tiles, whether hexameric, pentameric or trimeric, have distinct central pores that play a role in the semi-permeable nature of the outer shell. In this way, the composition of the shell also affects properties associated with diffusion into and out of the structure.

Only one proteomic analysis of a catabolic metabolosome has been reported and that relates to the isolated Pdu metabolosomes from *S. enterica*. In that study the authors were able to purify intact Pdu metabolosome structures and the samples were subjected to 2D gel analysis followed by quantification in order to gauge the relative proportion of the proteins that make up the assembly. Interestingly, they found that with the *S. enterica* Pdu BMC PduB and PduB` constituted approximately a quarter (25%) of the total protein and more than half (52%) of the BMC shell. PduA and PduJ were also quite abundant and in this respect PduB, PduB`, PduJ and PduA constitute over 90% of the shell, which means that PduK, PduU and PduT are minor components (Table 3.1). The vertex protein, PduN, was not detected, possibly due to its very low

abundance. These results suggest that PduB, PduB`, PduJ and PduA play a major role in holding the overall structure together and in mediating the majority of movement into and out of the BMC. PduK, PduN, PduT and PduU are likely to play more specialised roles.

Table 3.1. Shell protein composition based on Havemann and Bobik (2003). Percentage [%] and molecular masses of *Salmonella* BMC shell proteins as reported (*n.d. = not detected).

Shell protein composition	**PduA**	**PduB**	**PduB`**	**PduJ**	**PduK**	**PduN**	**PduT**	**PduU**
Molecular mass (kDa)	9.6	28.0	24.0	9.0	16.8	n.d.*	19.1	12.5
% shell protein	16	27	25	23	3	n.d.*	3	3

Following on from the proteomic study of the *S. enterica* Pdu BMC, researchers investigated the role of individual shell proteins through a programme of targeted gene knock-outs (Cheng *et al.*, 2011). As predicted from the previous proteomic study, deletion of the major shell proteins such as PduB`, PduB and PduJ severeley impaired BMC formation (summarised in Table 3.2). Strangely, deletion of *pduA* did not prevent BMC formation, but its absence did result in propionaldehyde accumulation in the growth media and a growth arrest phenotype.

Table 3.2. Essential structural proteins in Pdu metabolosomes and eBMCs. (+) essential structural component, expendable structural component (-).

	PduA	**PduB**	**PduB`**	**PduJ**	**PduK**	**PduM**	**PduN**	**PduT**	**PduU**
BMC	**-**	**+**	**+**	**+**	**-**	**+**	**+**	**-**	**-**
eBMC	**+**	**+**	**+**	**+**	**+**	**-**	**+**	**-**	**-**

In separate studies on *the C. freundii* Pdu system, it was shown that when the whole *pdu* operon was transformed into *E. coli*, the transformed bacteria were empowered with the ability not only to metabolise 1,2-PD, but also to generate recombinant BMC

structures (rBMCs) (Parsons *et al.*, 2008). The construction of these rBMCs effectively provided a powerful genetically tractable system with which to study BMC form and function. Following on from this research it was shown that empty BMCs (eBMCs) could be generated by the expression of selected shell protein genes (Parsons *et al.*, 2010a). The co-ordinated expression of the *pduA-B-J-K-N* (A-N construct) resulted in the appearance of proteinaceous bodies within the *E. coli* cytoplasm that had clear delimiting boundaries. Slightly larger structures were observed with the coordinated expression of *pduA-B-J-K-N-U* (A-U construct, Figure 3.1) and *pduA-B-J-K-N-U-T* (A-T construct). Smaller constructs containing *pduA*, *pduA-B*, *pduA-B-J*, *pduA-B-J-K* resulted in the appearance of filaments, swirls and rosettes within the cytoplasm of the cell. Thus, it would appear that eBMCs can be formed by a minimal set of shell proteins composed of PduA-B-J-K-N.

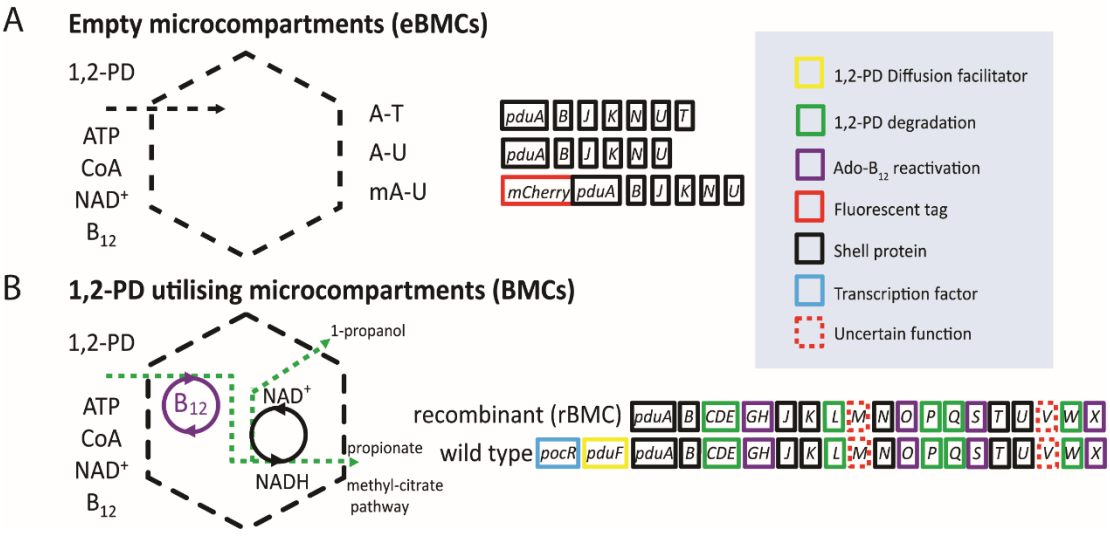

Figure 3.1. Schematic illustration of empty microcompartments and Pdu metabolosomes. **A.** Features of empty microcompartments (A-T, A-U and mA-U) **B.** Features of 1,2-PD utilising microcompartments (rBMC and wild type).

Furthermore, the order of gene expression would also appear important for BMC formation. Moving *pduA* to the end of the gene sequence, rather than having it at the start, was found to prevent BMC formation. In this respect, the relative abundance

of certain shell proteins was found to prevent BMC formation. Thus, the shell protein composition appears to be instrumental in permitting the shell assembly of these remarkable structures.

3.2. Aims and objectives

Although the generation of a recombinant Pdu BMC has greatly assisted our understanding of BMC form and shape, no detailed comparison of wild type, recombinant Pdu BMCs or eBMC variants was conducted. The major focus of the research described in this chapter was to address this problem. Therefore, the presence of BMCs in wild-type *C. freundii* was investigated and methods for BMC extraction and purification were developed. This permitted a proteomic analysis of wild-type Pdu BMCs from *C. freundii* and their comparison to both rBMC and eBMC structures (A-U, mA-U and A-T) in *E. coli*.

.

3.3. Visualising Pdu microcomparment formation *in vivo* by electron microscopy

As discussed earlier, the *in vivo* formation of bioengineered eBMCs and rBMCs in *E. coli* has been previously reported (Parsons *et al.*, 2008; Parsons *et al.*, 2010a; Sinha *et al.*, 2012). The transformation of *E. coli* (BL21(DE3)) with the appropriate *pdu* genes results in the occurrence of cytoplasmic-located structures that appear to be consistent with the presence of BMCs as revealed by TEM after thin-sectioning of the cells. In this chapter, the presence of both rBMCs and a number of eBMC variants are compared to wild type *C. freundii* BMCs by TEM.

A fully sequenced *C. freundii ballerup* strain (7851) with 99% sequence identity to the constructed *pdu* operon was obtained from the Sanger Institute (Cambridge, UK). To determine whether *C. freundii* had the ability to make Pdu BMCs, the strain was grown in NCE minimal medium in the presence of 1% (v/v) 1,2-PD (Section 2.6.4) to induce the formation of Pdu BMCs. After overnight growth the cells were harvested by centrifugation, resuspended in fixing solution, stained and embedded in agar low viscosity resin (in collaboration with Rokas Juodeikis, University of Kent). Cells were sectioned into 70 nm slices as described in Section 2.10.1.

In parallel, a range of *E. coli* strains producing rBMCs and eBMCs were prepared. Three different eBMC variants were tested: A full set of BMC shell proteins (A-T), a reduced set missing PduT (A-U) and a variant with mCherry fused to PduA (mA-U) were compared to Pdu BMCs (wild type and rBMC). This comparison allows an opportunity to explore the effects of the missing BMC shell protein PduT and the mCherry-PduA fusion on BMC formation. *E. coli* (BL21DE3) was transformed with plasmids to allow the production of rBMCs and eBMCs (A-U, mA-U and A-T). The cells were grown in rich medium (2YT). After the cultures reached an OD_{600} of 0.3-0.6, the cultures were induced with 100 µM IPTG and were allowed to continue growing overnight (Section 2.6.4). Cells were harvested by centrifugation, resuspended in fixing solution, stained and embedded in agar low viscosity resin. Thin sections were placed onto carbon grids and stained with uranyl acetate and lead citrate as described in Section 2.10.1.

Analysis of the thin sections by TEM provided clear results as shown in Figure 3.2. Firstly, as expected, thin sections of *E. coli* harbouring empty plasmids (Panels A and B) did not reveal the presence of any BMC-type of sub-cellular structure. Although the cytoplasm contains ribosomes and a nucleoid, no evidence of larger (100 nm) sized bodies are present within any of the observed bacteria. In contrast to control sections, a number of large proteinaceous bodies within the cytoplasm of the cell (Panel C) are clearly visible in *C. freundii*. Wild type Pdu BMCs appeared as distinct electron dense spots in the cytoplasm. Features such as size and shape appeared heterogenic. Although irregular in structure, wild type Pdu BMCs, had common features as distinct vertices and closed shells. Furthermore, they shared a pentameric to hexameric outline. Moreover, the bodies contain electron dense material suggesting high protein content.

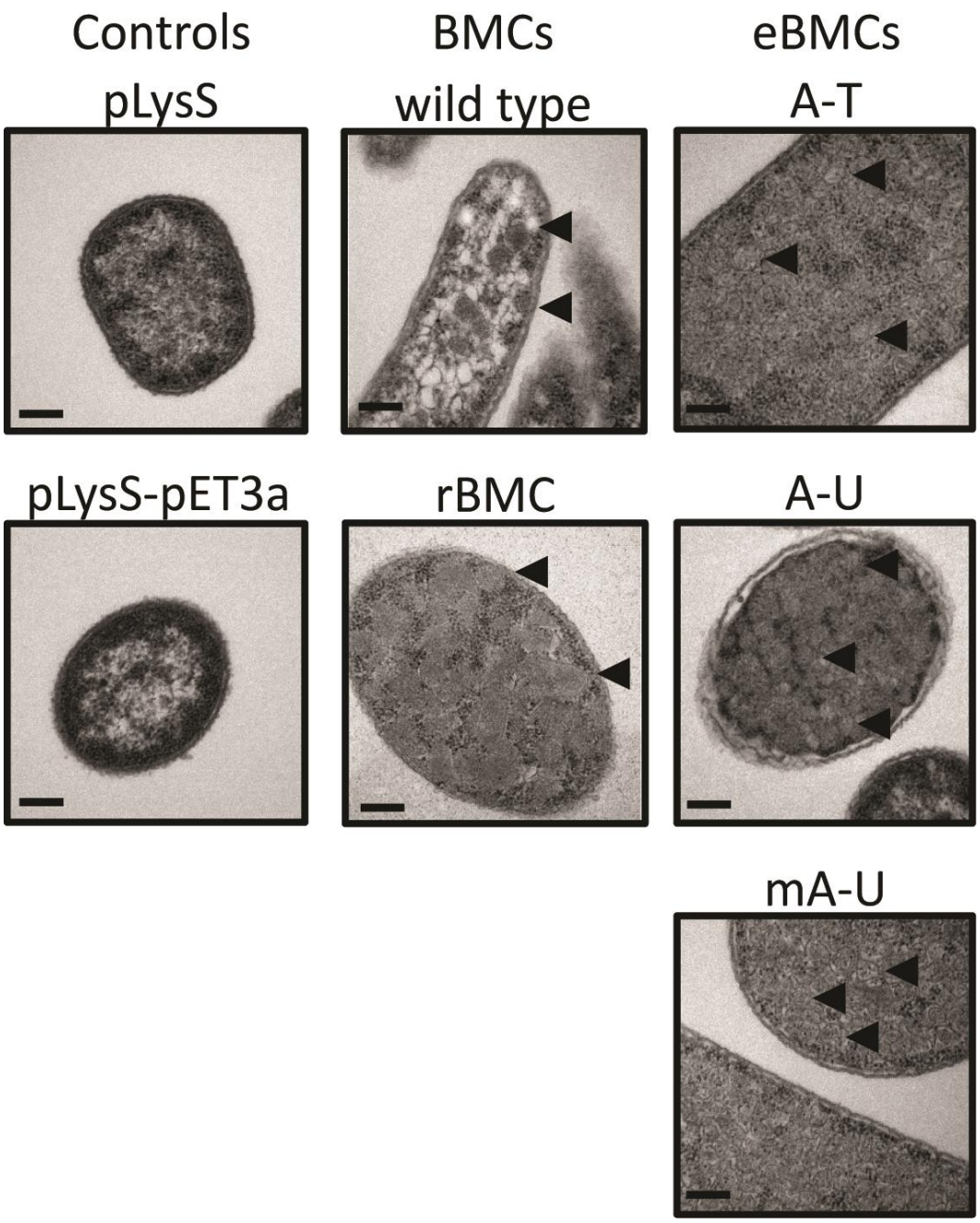

Figure 3.2. Presence of BMC in a range of bacterial strains. **Left.** Control section of *E. coli* containing pLysS and of *E. coli* containing pLysS and pET3a. **Middle.** Presence of BMC in a range of bacterial strains: Section of wild type *C. freundii* after growth on 1,2-PD. and section of *E. coli* containing the full recombinant *pdu* operon (rBMC) plasmid. **Right.** Section of *E. coli* containing the A-T, A-U and mA-U plasmid. Scale bars correspond to 200 nm. Single intracellular BMC structures are highlighted by arrows.

Similar bodies, but in much greater abundance, have been observed in *E. coli* that house the complete *pdu* operon (Panel D). Interestingly, the *E. coli* appear to have more ribosomes (Figure 3.2), which could be due to cellular stress associated with recombinant protein production, or could be due to the fact that the ribosomes are compressed into a smaller area due to the abundance of rBMC structures (Hoffmann; Rinas, 2004). Both wild type and rBMCs are heterogeneous in size and structure, and appear to have pentameric or hexameric-like shapes.

Cells containing the genetic material for eBMC variants (A-U, mA-U and A-T) were densely packed with closed proteinaceous subcellular structures. All the *E. coli* strains producing eBMCs were also found to contain similar irregular polygonal structures (Panels E-G) to wild type and rBMC structures (Panels C-D). The reduction of BMC shell proteins from A-T to A-U has no obvious detrimental phenotypical effect. The presence of the mCherry-PduA fusion producing mA-U strain (Panel F) does not appear to have an adverse effect on the size or shape of the empty organelle in comparison to the eBMCs produced in the strains harbouring A-U (Panel E) or A-T (Panel F). Overall, the size of the eBMCs was noticeably smaller than the rBMCs and wild type BMCs seen in *C. freundii*. These differences in size could be due to a difference in the BMC shell composition or could be due to the fact that eBMCs lack internalised proteins. The lack of incorporated enzymes could lead to a deflation of the overall structure. Finally, it is also noticeable that the size of the bacterial cells that contained the eBMCs varied.

Many of the cells in Figure 3.2 appeared elongated, possibly due to problems associated with septation. Alternatively, elongated cells could reflect a stress response due to the pressure associated with producing so many unnatural structures within *E. coli* (Hoffmann; Rinas, 2004; Parsons *et al.*, 2010a). The dense packing of the cells with eBMC variants and rBMC structures made it difficult to analyse single structures of eBMC variants and rBMCs.

Due to the tight packing of recombinant Pdu microcompartments and the proximity of Pdu BMCs in wild-type Pdu BMCs, it was essential to extract and purify these structures as monodispersed particles. Purification permits the proteomic

characterisation. Furthermore, the isolation of Pdu microcompartments is vital for structural analysis and the biochemical characterisation of cofactor uptake and accumulation.

3.4. Development of purification strategies for eBMC variants, rBMC and wild type Pdu BMCs

The detailed analysis of Pdu BMCs requires efficient and robust extraction and purification methods to allow the isolation of intact organelles in a sufficient yield for proteomic analysis, high resolution imaging techniques and biochemical investigations of the organelle. Two related methods have been independently developed for BMC isolation (Sinha *et al.*, 2012; Lawrence *et al.*, 2014). The two methods utilise mild detergent lysis procedures, employing either a bacterial specific lysis reagent (B-PER™) or a yeast specific lysis reagent (Y-PER™, Section 2.6.11 and Section 2.6.12). The detergent based cell lysis method is a comparatively gentle method for releasing cellular contents without requiring more damaging as *e.g.* mechanical forces during sonication. To determine which purification works best, both processes were compared for the isolation of wild type BMCs, rBMCs and eBMC variants. The purified samples were analysed by SDS-PAGE (Figure 3.3).

3.4.1. Evaluation of purification methods for rBMC and native BMC isolation

Purified BMCs give a characteristic banding pattern that reflects the major proteins associated with the organelle in SDS-PAGE. This distinct fingerprint can be seen in Figure 3.3, lanes 2 and 4 (Sinha *et al.*, 2012; Lawrence *et al.*, 2014). In this case the two lanes represent wild type and rBMC purified by the B-PER™ procedure. The two lanes show that the rBMC and wild type BMCs have been purified to a high quality

with the B-PER™ procedure. Major BMC shell protein bands at 30 kDa, 25 kDa, 22 kDa, 10 kDa and 9 kDa represent PduB, PduB`, PduK, PduU, PduA and PduJ.

Use of the Y-PER™ (Lanes 1 and 3) method resulted in the isolation of an indistinct set of high molecular mass proteins. Analysis by SDS-PAGE revealed that BMCs were only purified effectively using the bacterial protein reagent (B-PER™) protocol. No differences in purification were observed for heterologously formed rBMCs and native microcompartments. For all follow up experiments BMCs (wild type and rBMC) were purified using B-PER™.

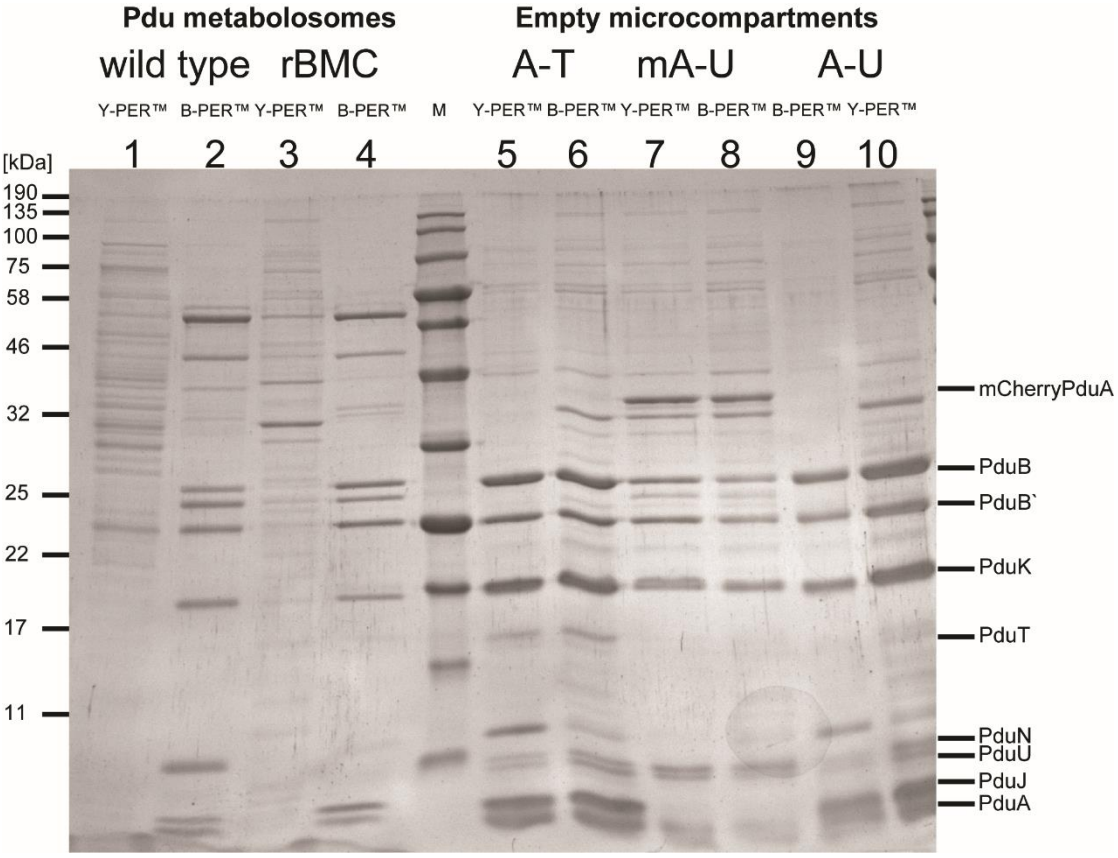

Figure 3.3. Comparative purification of BMCs using either B-PER™ or Y-PER™ reagent. 15% polyacrylamide gel, 10 µL loaded each lane, (M) marker. The typical shell protein fingerprint is shown on the right.

3.4.2. Enhancing purification protocols for empty microcompartments by SDS-PAGE

Figure 3.3 reveals that all the eBMCs (A-U, mA-U and A-T) can be isolated to a high level of purity by using either the B-PER™ or Y-PER™ method (Lanes 5 to 10).

In summary, a comparison of the two major methods for BMC isolation reveals that the larger complete wild type and rBMCs should be purified by the B-PER™ method. The smaller eBMCs can be isolated by either method. The eBMC variants differ from BMCs in their purification, likely reflecting either a change in their shell protein composition or a change in their size.

3.4.3. Evaluation of the purification protocols for the eBMC structures as judged by western blot analysis

The two methods for BMC purification utilising either B-PER™ or Y-PER™ reagent were tested for their effectiveness in the purification of eBMCs. The purification of BMCs can become contaminated by the presence of aggregating proteins and thus proteins that are co-produced with BMCs can sometimes co-purify with purified BMC fraction. To evaluate the purification procedures the B-PER™ and Y-PER™ purifications were performed in the presence and absence of eBMCs (A-U) in *E. coli*.

After growth and cell lysis using either B-PER™ or Y-PER™ and purification, co-purification of either CobN or CobR was investigated by western blot using an anti His_6 antibody (Section 2.8.3). The results, in Figure 3.4, suggest that the Y-PER™ method is more appropriate for the isolation of eBMCs as it restricts the amount of contamination from either CobN or CobR. In contrast, more signal is observed on the western when B-PER™ is used in the extraction process. Therefore, in all follow up experiments the Y-PER™ methods was used for eBMC isolation.

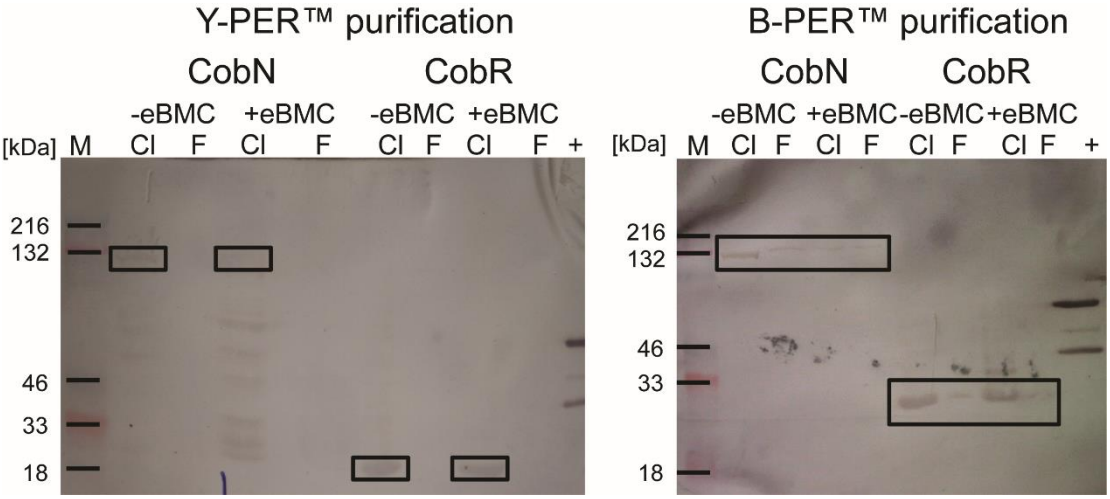

Figure 3.4. Specificity of eBMC purification protocols in presence (+) and absence (-) of eBMCs judged by western blot analysis. The left blot demonstrates the relatively specific purification using Y-PER™. Western blot signal for CobN and CobR was only detected for crude lysate samples. The right blot demonstrates the relatively unspecific purification of CobN and CobR in Cl and final fraction (F), using the B-PER™ purification protocol in both absence (-eBMC) and presence (+eBMC) of eBMCs. 15% SDS-PAGE. 10 µL loaded each lane. Cl and F were both applied to western blot analysis. Marker (M) is on the left and a positive control (+) on the right.

3.5. Determination of the shell protein composition of Pdu microcompartments

A proteomic analysis of wild type BMCs, rBMCs and eBMCs was undertaken to investigate significant differences in shell protein composition. As outlined above such changes in protein composition of the BMC shell and incorporated enzymes could alter their structure and potentially cause differences in their purification. To investigate their protein profiles, purified fractions containing BMCs were separated by 2D PAGE (Section 2.8.2). The 2D gels are shown in Figure 3.5. Protein spots were picked and analysed by peptide mass fingerprinting (MALDI TOF and TOF-TOF, Section 2.8.4, see appendix).

3.5.1. Detection of single shell proteins of purified Pdu metabolosomes

Pdu metabolosomes (rBMCs and wild-type) were extracted and purified from overnight cultures and analysed by isoelectric focussing and SDS-PAGE (2D-PAGE, Figure 3.5, Section 2.6.12 and 2.8.2). From the resulting gel, all encoded Pdu shell proteins in rBMCs produced in *E. coli* and wild type BMCs were identified (PduA, PduB, PduB`, PduJ, PduK, PduN, PduT and PduU). SDS-PAGE and 2D-PAGE suggest that the BMCs are purified to a high extent.

All encoded shell proteins were identified from the purified Pdu microcompartment fractions. The high level of purity allowed the protein components of the BMCs to be quantified by densitometric measurements.

3.5.2. Detection of single shell proteins of purified empty microcompartments

The single shell proteins that were detected from the purified eBMC structures are shown in Figure 3.5. Details of the MALDI TOF-TOF analysis (Section 2.8.4) for individual shell proteins are reported in Section 7.1. The shell protein data are comparable to the previously reported proteomic study of the *S. enterica* Pdu BMC, as the shell proteins migrated with a similar profile. Predictably the data were also similar to Pdu BMCs from *C. freundii* formed natively or heterologously in *E. coli* (rBMC) (Havemann and Bobik, 2003; Sinha *et al.*, 2012).

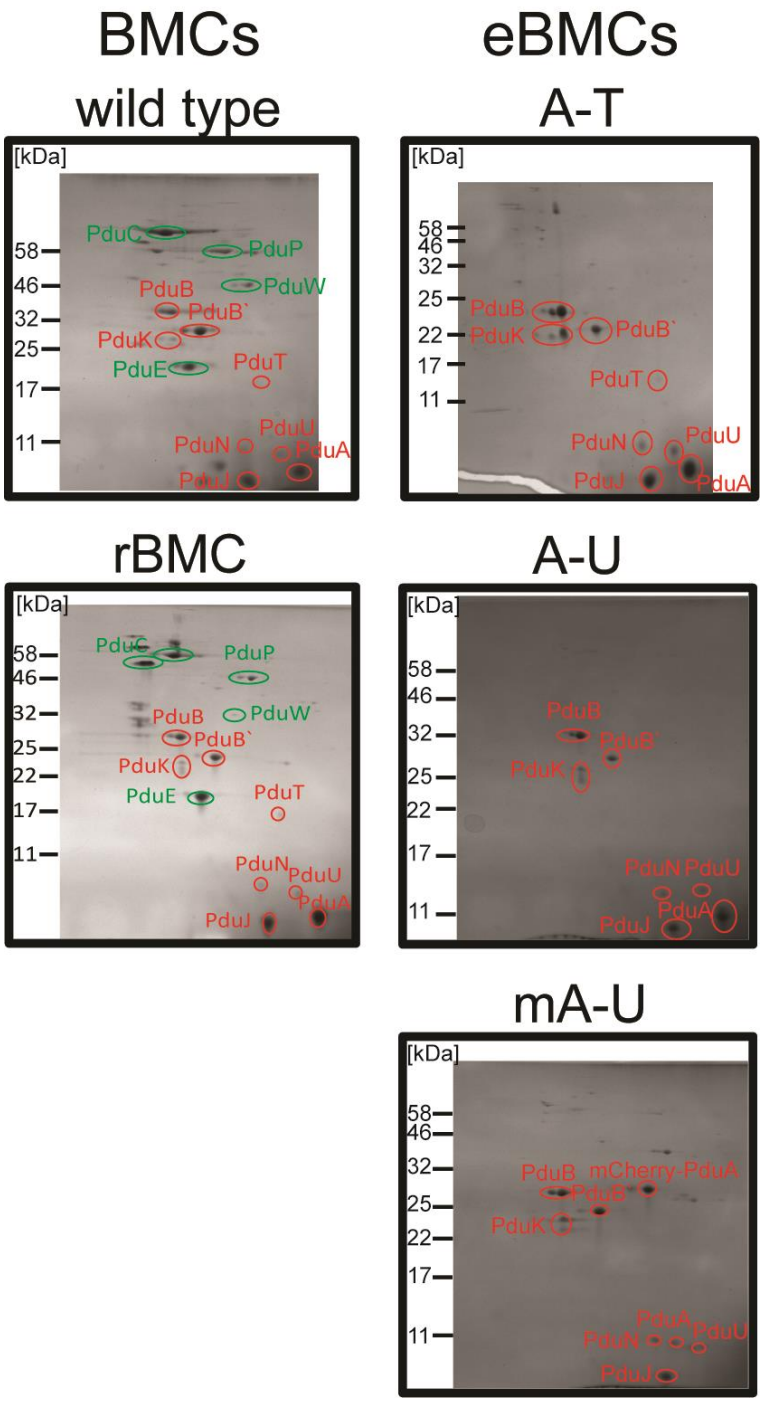

Figure 3.5. 2D-PAGE of wild type BMC, rBMC and purified eBMC variants. Purified protein fractions (160 µg) were applied to 2D-PAGE. Molecular mass standards are shown on the left of each gel. Shell protein spots (red) and BMC related metabolic enzymes (green) were identified by tandem mass spectrometry. **Wild type.** Purified Pdu metabolosomes, extracted from *C. freundii*. **rBMC.** Purified Pdu metabolosomes, extracted from *E. coli*. **A-T.** Purified empty microcompartment (A-T), extracted from *E. coli.* **A-U.** Purified empty microcompartment (A-U), extracted from *E. coli* **mA-U.** Purified empty microcompartment (mA-U), extracted from *E. coli***.**

The 2D gels for the eBMC variants are shown in Figure 3.5. The gels reveal a clear separation of the various proteins. From these gels, the majority of the BMC associated proteins were identified by peptide mass fingerprinting. Protein spot localisation of eBMCs led to the identification of all BMC shell proteins. The purified eBMC fractions were estimated to be more than 90% pure by densitometric measurements of the SDS-PAGE (Figure 3.3) image. All eBMC variants were found to have a high degree of purification, suggesting that they had been isolated intact.

3.5.3. Shell protein composition of Pdu microcompartments

The protein spots observed in the 2D gels were quantified by densitometric measurements using ImageJ v.1.48 (Section 2.8.2.2; Figure 3.6) (Rasband, 1997). ImageJ v.1.48 is an imaging processing freeware, available from http://rsb.info.nih.gov/ij.

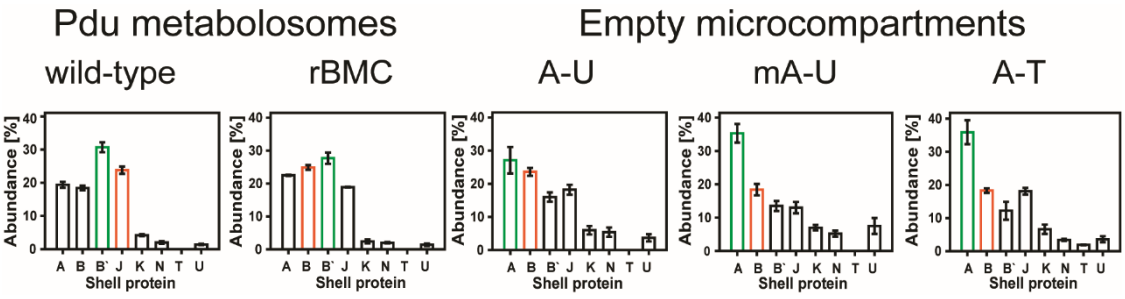

Figure 3.6. Shell protein composition of Pdu microcompartments. Normalised average abundance (N=3) of single shell proteins of Pdu metabolosomes (wild type and rBMC) and eBMCs (A-U, mA-U, A-T) and standard errors of mean are given. The predominant shell protein is coloured green and the 2nd most abundant shell protein is coloured in orange.

The results showing the relative abundance of the shell proteins in various BMCs are outlined in Figure 3.6. The most abundant BMC shell protein of the Pdu metabolosomes (rBMC and wild-type) is PduB` (28%, 31%). PduB (18%, 25%), PduA

(23%, 19%) and PduJ (19%, 24%) are also major shell protein components. PduK, PduN, PduT and PduU are minor shell protein components comprising less than 10% of the shell. PduT was not quantified accurately due to its low spot intensity (see Figure 3.5-6).

In the eBMC variants that were analysed, PduA was found to be the major Pdu shell protein component (27-35%) followed by PduB (18-24%). PduB` (12-16%) and PduJ (13-18%) are further major components of the Pdu shell. PduK, PduN, PduT (only in A-T) and PduU are the minor Pdu shell components comprising less than 20% of the Pdu shell. Although some variation in the shell protein composition has been noted for eBMCs, the overall trend is similar.

The purified eBMC fractions differ from the purified BMC fractions in the relative abundance of their building blocks. Whereas PduA is the most abundant shell protein in purified eBMC fractions, PduB` is the most common BMC shell protein in purified Pdu BMC fractions of wild type and rBMCs. As with the analysis of the eBMCs, some variation was observed between rBMC and wild type BMC structures. In rBMCs the order of shell protein abundance is PduB`-PduB-PduA-PduJ whereas the wild type BMCs have an assigned hierarchy of PduB`-PduJ-PduA-PduB. However, overall the profile of the rBMC to wild type is remarkably similar indicating that they have a very similar composition.

The major conclusion from this comparative proteomic analysis is that eBMCs appear to incorporate more PduA, in comparison to their Pdu counterparts (wild type and rBMC). Whether this reflects a different expression pattern or whether this reflects a consequence of lacking internal cargo has yet to be determined.

3.6. Discussion

The research in this chapter has addressed questions concerning the *in vivo* formation of heterologously formed eBMCs and rBMCs in *E. coli* and the wild-type assembly of Pdu metabolosomes in *C. freundii*. *E. coli* cells recombinantly producing eBMCs and rBMCs were found to be densely packed with supramolecular structures in comparison to the presence of fewer distinct organelles in wild-type *C. freundii* (Parsons *et al.*, 2010a; Frank *et al.*, 2013).

The extraction and purification protocols for eBMCs and Pdu BMCs were compared in order to allow optimisation of the isolation procedures. Interestingly, eBMCs purified more effectively with Y-PER™ whereas rBMCs and wild type BMCs purified more readily with B-PER™. The differences in the purification likely reflect differences in protein composition or other biophysical parameters.

The protein composition of the eBMCs (A-U, mA-U and A-T) as well as the rBMC and wild type BMC were analysed by 2D-PAGE. This resulted in a series of well-resolved protein spots that allowed a detailed proteomic analysis of the organelles. In all cases the proteins were clearly identifiable, including the vertex protein PduN, whose presence has previously been difficult to identify due to its low abundance.

The presence of the mCherry-PduA fusion did not affect the formation of the eBMC. This all helps to confirm the idea that the Pdu BMC assembly is a flexible process giving rise to highly stable macro-molecular structures.

The quantification of the various shell proteins associated with BMC formation provided some interesting observations. With rBMCs and wild type BMCs, PduB is the most abundant shell protein. In contrast, with all eBMC variants PduA is the major shell protein. These differences in composition will be used to explain the differences in the physical properties of the eBMCs in comparison to the complete structures (see Chapter 4). The differences in protein composition may also explain the differences observed in their purification.

Chapter 4

A structural comparison (by AFM and TEM) of wild type *C. freundii* Pdu BMCs to recombinant Pdu variants produced in *E. coli*

4.1. Introduction

Following on from the proteomic differences observed in the shell protein composition of eBMCs and Pdu BMCs, the structural consequences of missing incorporated enzymes and altered shell protein composition were analysed. This was investigated by both EM and AFM, which, together, allow for estimations of the size distribution, nano-mechanical properties and the internal structural organisation of the organelles to be determined.

Structural information of single Pdu BMC shell building blocks has been determined from X-ray studies of individual shell proteins such as PduA, PduB, PduT and PduU (Frank *et al.*, 2013; Chowdhury *et al.*, 2014). In addition to the structural information of various shell proteins of carboxysomes, the overall structure of extracted and purified α-and β-carboxysomes has been reported in two independent studies through the use of electron cryo-tomography data (Schmid *et al.*, 2006; Iancu *et al.*, 2007; Yeates *et al.*, 2013; Rae *et al.*, 2013). These studies revealed that tomographs of carboxysomes can be reconstructed as regular icosahedral structures, incorporating 20 faces, 30 edges and 12 vertices. In this model, all faces are triangular. The size distribution of carboxysomes was also reported. Surprisingly, this revealed that α-carboxysomes from *H. neapolitanus* varied between 90 and 100 nm, whereas β-carboxysomes from *Synechococcus* WH8102 had a size of 120 to 130 nm. More generally, carboxysome sizes range from 90 nm to more than 500 nm (Rae *et al.*, 2013). Although there are many structural and functional similarities of α-and β-carboxysomes, it is not known if there are any functional consequences associated with the different sizes. In contrast to these relatively detailed structural analysis of the carboxysomes, much less is known about the size distribution, internal organisation and the overall structure of Pdu BMCs because isolated BMCs are much less homogeneous than their anabolic counterparts (Corchero; Cedano, 2011; Frank *et al.*, 2013; Chowdhury *et al.*, 2014).

In fact, TEM analysis of catabolic Pdu BMC structures reveals that they are quite irregular in shape even though they have previously been described as regular icosahedral structures, analogous to carboxysomes (Corchero; Cedano, 2011). The diameter of the *S. enterica* Pdu BMC was reported as 123 ± 30 nm, indicating that they have a greater variation in size, in comparison to carboxysomes (Cheng *et al.*, 2011). Recombinant *C. freundii* Pdu BMCs (rBMCs) were reported to have a diameter of 108-123 nm but no structural data have been reported on the eBMCs or the wild type BMCs from *C. freundii* (Parsons *et al.*, 2008). This chapter focuses on the structural characterisation of eBMC variants and their comparison to heterologously formed rBMCs and wild type BMCs.

This was achieved by using a combinatorial approach consisting of different transmission electron microscopy (TEM) and atomic force microscopy (AFM) techniques to analyse the size distribution, nano-mechanical properties and internal structural organisation of *C. freundii* Pdu BMCs. The relative advantages and disadvantages of electron microscopy and atomic force microscopy are discussed below. Electron microscopes use accelerated electrons as a source of illumination (Adrian *et al.*, 1984; Bai *et al.*, 2015). The high resolution of electron microscopes relies on the, up to 10^5, shorter wavelength of electrons in comparison to light photons. Thus, smaller structures can be imaged with a resolution of up to 50 pm. Electrostatic and electromagnetic lenses are used to control the electron beam and focus it, to form an image, rather than the optical lenses found in light microscopy. In standard TEM applications, biological samples are chemically fixed by the crosslinking of proteins with aldehydes (standard TEM) or fixed by freezing in liquid ethane (for cryo-EM). Sample preparation requires negative stain (*e.g.* uranyl acetate).

Atomic force microscopy (AFM) is a more recent technique that has evolved into a useful tool for the direct measurement of structural parameters. It can also be used to determine mechanical forces at a nanoscale level (Jalili; Laxminarayana, 2004). Typically, AFM systems consist of a micro-machined cantilever probe and a sharp tip (1-2 nm in diameter) mounted to a piezoelectric actuator and a position-sensitive

photo detector for receiving a laser beam reflected off the end-point of the beam, to provide cantilever deflection feedback, as shown in Figure 4.1.

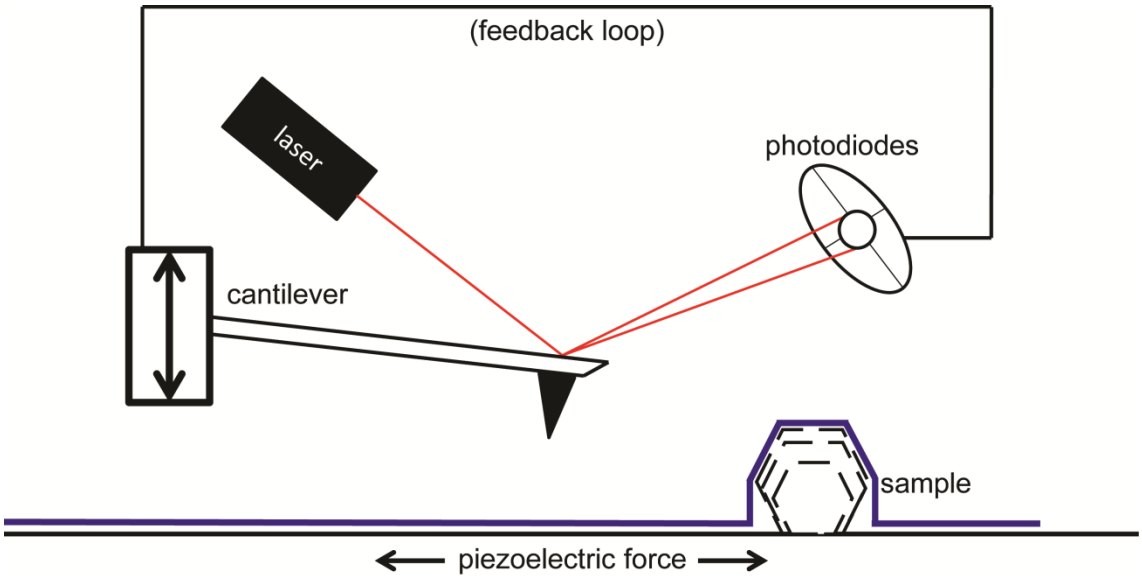

Figure 4.1. Schematic of a basic AFM operation.

The principle of AFM operations is to scan the tip over the sample surface. Feedback mechanisms enable the piezoelectric scanners to maintain the tip at a constant force or height above the sample surface. As the tip scans the surface, moving up and down with the contour of the surface, the differences in light intensities between the upper and lower photo detector are measured. The system is readjusted by a feedback loop corresponding to the incoming signal.

Three operation modes are commonly used for AFM applications: non-contact mode, contact mode and tapping mode (Sweers *et al.*, 2011; Foster, 2012). In this study, the ScanAsyst mode from Bruker was used for topological scans and high resolution imaging. Basically, ScanAsyst uses the tapping mechanism. In contrast to standard tapping mode imaging, critical imaging parameters are automatically adjusted. Automated feedback loops, such as ScanAsyst, ease the access for user groups not specialised on AFM applications and contribute to the implementation of AFM.

The real advantage of AFM in comparison to other biophysical and structural tools lies in the possibility to directly measure topolopy and additional parameters in a simultaneous fashion. In compression studies (quantitative nano-mechanical mapping), nano-mechanical parameters (reduced Derjaguin-Muller-Toporov (DMT) modulus, adhesion, deformation and dissipation) of biological samples can be elucidated at the same time as requiring topological information. The Derjaguin-Muller-Toporov (DMT) elasticity model describes the contact mechanics of the probe interacting with the scanned surface. In contrast to other elasticity models, the DMT modulus takes additional attractive interactions outside the area of contact into account. In less technical words, the reduced DMT modulus is used to describe the sample stiffness of the deposited biological sample. The cantilever impacts the surface only for a minimal amount of time to separate the contributions from different material properties such as reduced-DMT modulus and deformation. Quantitative nano-mechanical measurements (QNM) use the ability of the AFM system to acquire and analyse the individual force curves from each tap that occurs during the imaging process (Figure 4.2).

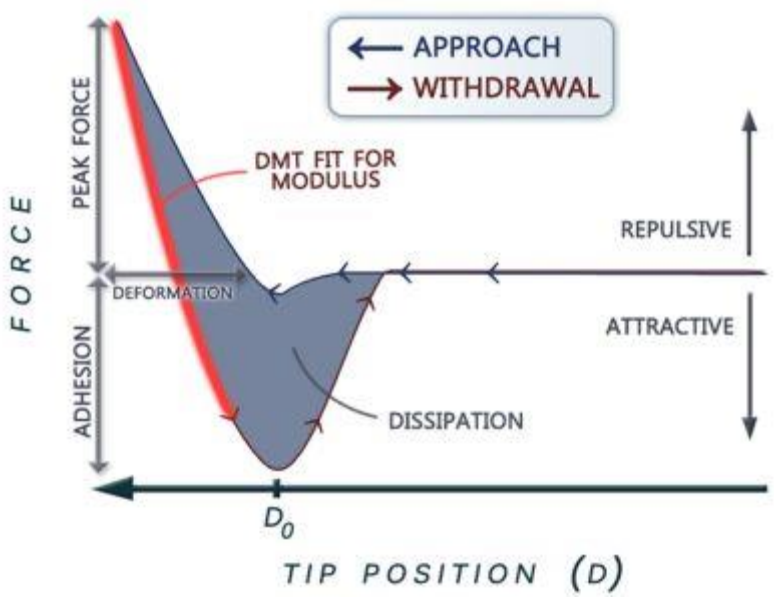

Figure 4.2. Individual force curve for quantitative nano-mechanical measurements (© http://www.imaging-git.com).

Thus, AFM can assist in the determination of nano-mechanical properties of biological materials. Further applications such as the measurement of particles in-solution have helped establishing AFM as a powerful tool in the analysis of biological samples.

4.2. Aims and Objectives

In Chapter 3, methods for the isolation of intact Pdu microcompartments were developed, which permitted a comprehensive proteomic analysis. The purified BMCs provided an opportunity to investigate their structural and biophysical properties.

The aims in this chapter are therefore to apply both TEM and AFM measurements to purified BMCs in order to compare their structural parameters. In this respect, purified wild type BMCs were compared to rBMCs and eBMCs.

4.3. General observations of BMC imaging by TEM

In parallel with the proteomic analysis of Pdu microcompartments (Chapter 3) the various microcompartments (wild type, rBMC, A-U, mA-U and A-T) were analysed by TEM (Section 2.10.1). To achieve this, isolated microcompartments were deposited onto carbon grids and were stabilised with glutaraldehyde. After washing, the sample grids were negatively stained with uranyl acetate and dried before visualisation by TEM.

The isolated Pdu microcompartments (wild type, rBMC, A-U, mA-U, A-T) appeared to be highly pure as viewed by negative stain TEM (Figure 4.3). The TEM images are therefore consistent with the proteomic analysis in Chapter 3, which showed that the isolated compartments had a homogeneous protein content. As observed in Figure 4.3, some tendency for aggregation was seen for wild type BMCs (Panel A). This might be due to the high density of the wild type Pdu microcompartments or it may reflect on the ability of the structure to interact with other BMC particles.

Wild type BMCs were also observed to adopt a wide variety of different shapes (Figure 4.3, Panel A) and appeared to be irregular in overall topology. No major differences in size and shape were visualised between wild type (Panel A) and rBMC structures (Panel B). This suggests that the heterologous formation of Pdu BMCs in *E. coli* does not affect BMC size. To identify significant differences between wild type Pdu BMC and rBMC structures or between different eBMC variants, the diameter and area of single particles (N>100) were measured by ImageJ v.1.48. These data are compared later on to those obtained by AFM in Section 4.5.

No obvious structural differences were visualised between the different eBMC variants (Panels C-E). This suggests that the presence of PduT does not affect the BMC structure and that the fusion of mCherry to the N-terminus of PduA does not disrupt BMC assembly, size or shape.

However, a clear size difference was visualised between 1,2-PD metabolising microcompartments (wild type and rBMC), when compared to eBMC variants. The differences in size (diameter and area) are quantified later in Section 4.5.

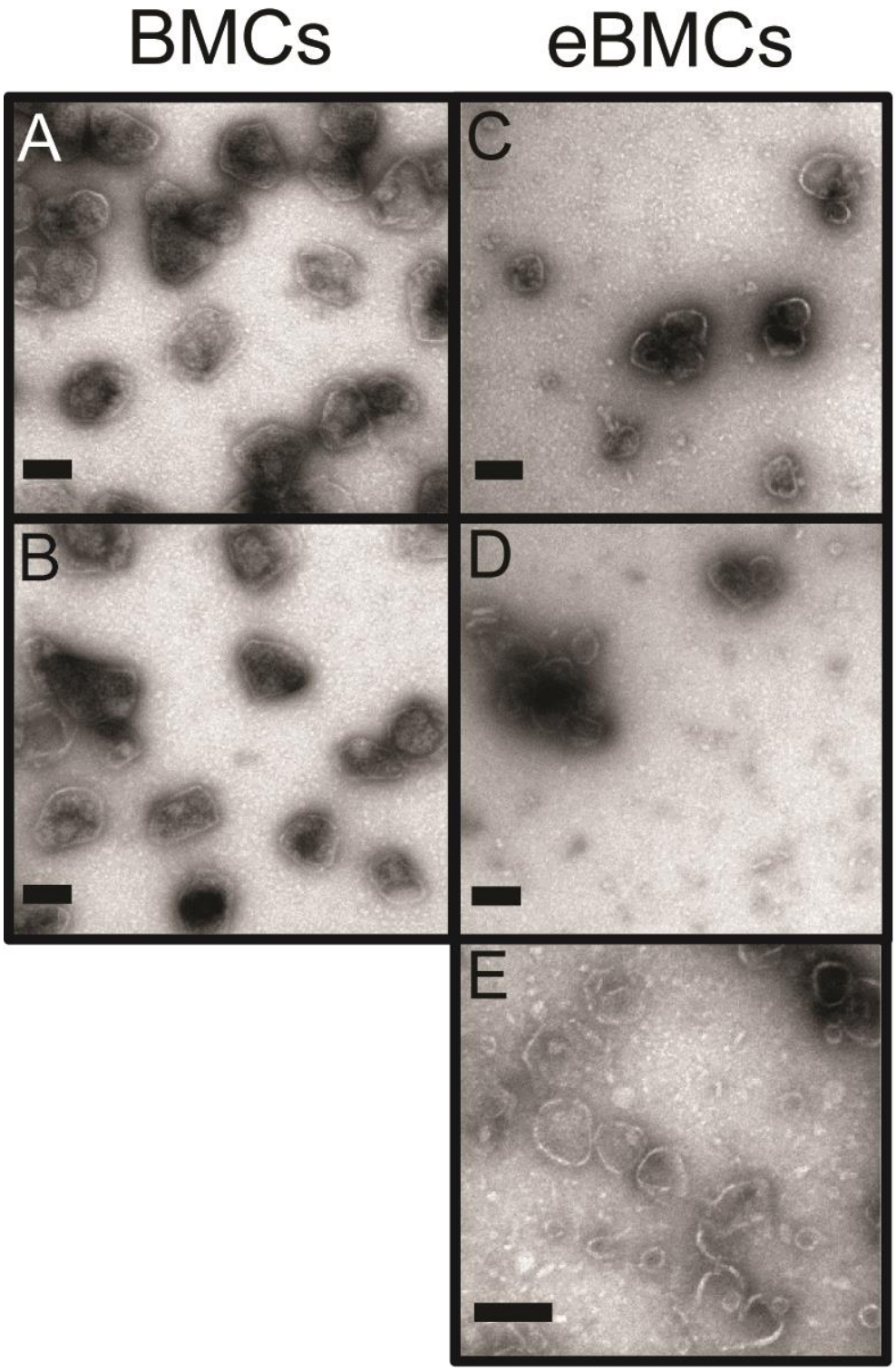

Figure 4. 3. Representative TEM micrographs for purified Pdu microcompartments. **A.** Purified wild type BMCs, isolated from *C. freundii* after growth on 1,2-PD. **B.** Purified rBMCs, isolated from *E. coli* harbouring the full recombinant *pdu* operon plasmid (rBMC) **C.** Purified A-U eBMC, isolated from *E. coli* harbouring the empty shell construct A-U **D.** Purified mA-U eBMC, isolated from *E. coli* harbouring the empty shell construct mA-U. **E.** Purified A-T BMC, isolated from *E. coli* harbouring the empty shell construct A-T. Scale bars correspond to 100 nm.

In addition to Pdu microcompartments, filamentous structures were visualised with the wild type and rBMC structures when imaged by TEM (Figure 4.4). The diameter of the filaments in the wild type Pdu BMC samples (10-20 nm) was smaller than the measured diameter in the rBMC samples (20-40 nm). On the other hand, filaments in wild type samples were observed to be longer (up to 10 μm) than those in the rBMC samples (<3 μm). These different characteristics (length and diameter) suggest that the filaments originate from different proteins. The protein(s) associated with these observed filaments was not identified. No filamentous structures were observed for the eBMC variants (A-U, mA-U and A-T) that were also imaged by TEM.

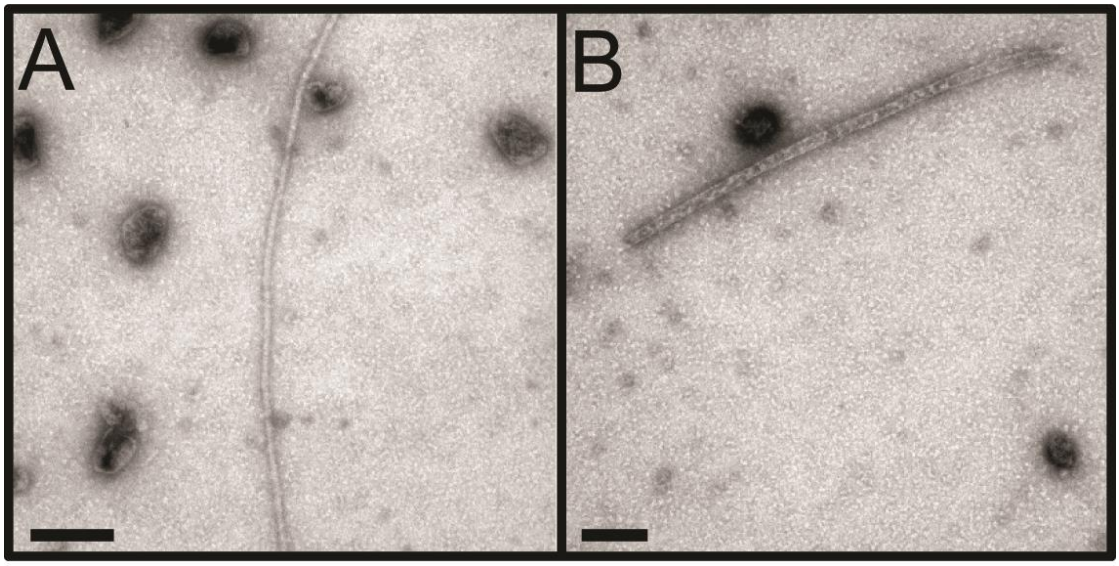

Figure 4.4. Co-purified filamentous structures in TEM. Transmission electron microscopy (TEM) of filamentous structures in purified BMC fractions. **Panel A.** Purified wild type Pdu BMCs, extracted from *C. freundii*. **Panel B.** Purified recombinant Pdu BMCs (rBMC), isolated from *E. coli*. Scale bars correspond to 200 nm.

4.4. General observations of BMC imaging in high resolution AFM

One of the long term goals in the study of catabolic BMCs is to determine an overall structure of the organelle. One possible way to elucidate the structure of Pdu microcompartments is to use in-solution AFM. The advantage of in-solution measurements is that the sample is subject to comparatively mild sample reagents, which should retain the topology of the assembly. In contrast to EM, no harsh sample preparation steps such as freeze drying or staining are required. For in-solution AFM, (ideally) native samples can be imaged in a repetitive and non-invasive fashion.

The sample preparation for in-solution AFM imaging is reported in Section 2.10.2.3. In contrast to high resolution semi-dry sample scanning (Section 2.10.2.2), purified Pdu microcompartments (wild type) were deposited onto a HOPG surface (graphene, no charge) for in-solution AFM and stabilised with glutaraldehyde. Unlike TEM sample preparation, AFM samples do not require staining. Next, the surface was washed with distilled water and dried under a gentle stream of nitrogen. Dried down surfaces were rehydrated in buffer and images were obtained using the ScanAsyst mode for in-solution applications. Areas of 5 µm *x* 5 µm were scanned at a resolution of 1024 samples per lane (Figure 4.5).

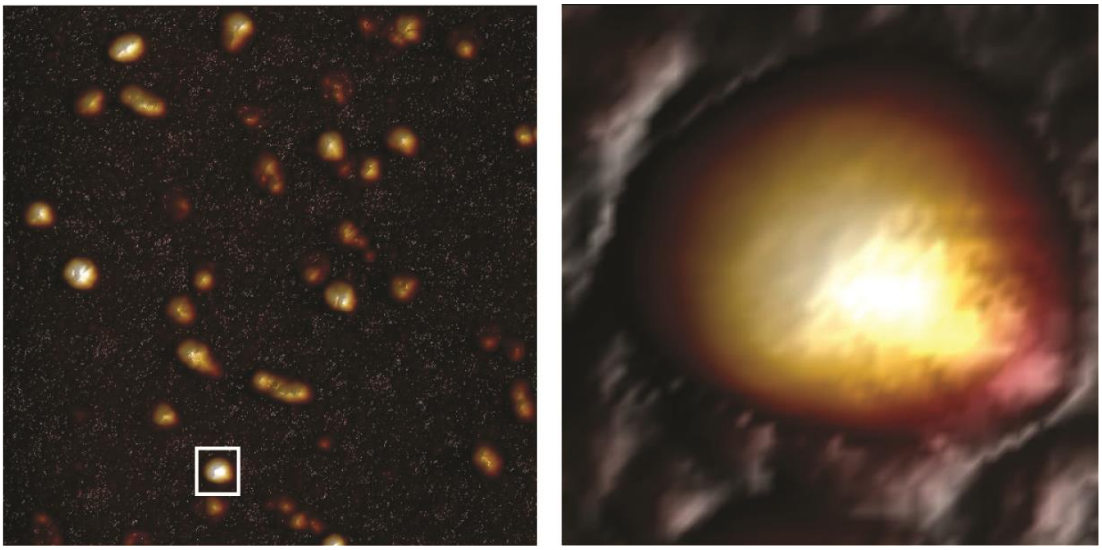

Figure 4.5. In solution AFM of rehydrated wild type Pdu BMCs. **LEFT.** Overview of a 3 *x* 3 µm crop out (autoscale setting). The white square resembles the single particle on the right. **RIGHT.** Single wild type Pdu BMC particle (top view, 240 *x* 240 nm).

The initial experiment with purified wild type Pdu microcompartments provided several interesting insights. First of all, it was possible to image rehydrated BMCs at low resolution in a repetitive and non-invasive fashion. The second observation was that the size (diameter, area and height) of the deposited particles showed no difference to semi-dry AFM data shown in Section 4.4 and Section 4.5. However, in-solution AFM did not improve the image quality in this study. Furthermore, technical difficulties did not allow the imaging of multiple sample specimens at a high resolution, as required for this study. Some sample drift was observed and thus technical solutions need to be found for this research to be taken forward. Consequently, this study focused on semi-dry AFM for the structural characterisation of Pdu microcompartments and their quantitative nano-mechanical measurements.

In parallel with proteomic and negative stain TEM analysis, the various microcompartments (wild type, rBMC, A-U, mA-U and A-T) were scanned using semi-dry AFM. The purified microcompartments were deposited onto MICA (silicate, negative charge) surfaces (Section 2.10.2.2). After deposition, BMC structures were stabilised by crosslinking with glutaraldehyde. The surfaces were washed with distilled water and dried under a gentle stream of nitrogen. Next, 10-20 µm squares were scanned at a resolution of 4096 samples per lane. Such high resolution measurements were conducted overnight to ensure run stability at a constant temperature. Both factors are necessary in order to generate stable, high quality scans (4½ h per scan).

As with the TEM images of wild type and rBMCs, filamentous structures were observed. These filamentous structures found in wild type samples had lengths of up to 10 µm and an average diameter of 10-20 nm (Figure 4.6), whereas the filaments in the rBMC samples had a diameter of 20-40 nm and lengths of up to 3 µm. The measured peak height of both filamentous structures was roughly 10 nm.

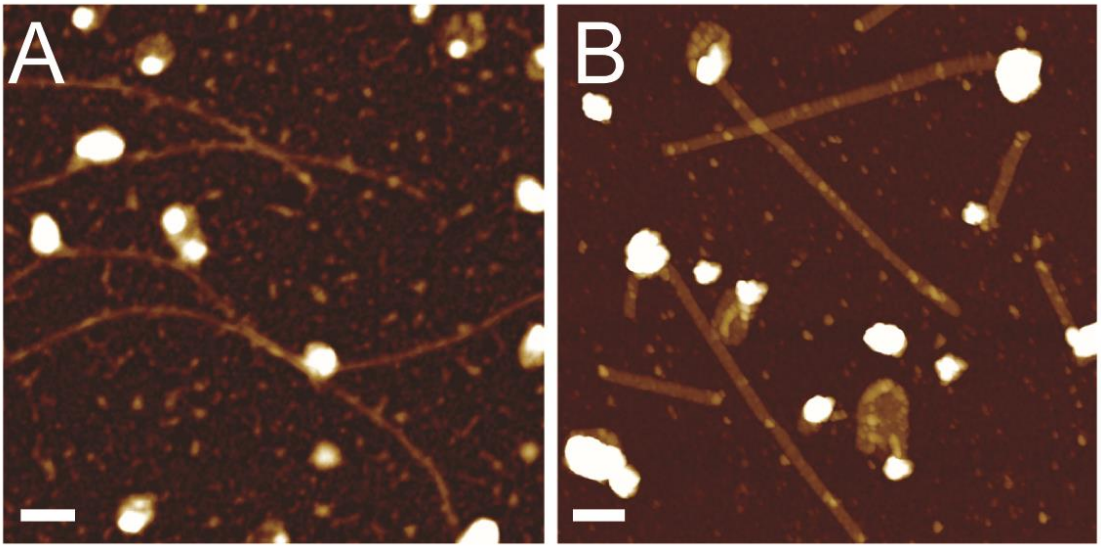

Figure 4.6. Co-purified filamentous structures in AFM. AFM scan of filamentous structures in purified BMC fractions. **Panel A.** Filamentous structures, extracted from *C. freundii*. **Panel B.** Filamentous structures, extracted from *E. coli* harbouring the rBMC plasmid. Scale bars correspond to 200 nm.

After analysis of these filamentous structures, individual BMC particles were identified and characterised. The general observations made by AFM are consistent with those made by TEM reported in Section 4.3. All the isolated microcompartments (wild type, rBMC, A-U, mA-U and A-T) appeared to be highly pure.

Catabolic Pdu BMC structures (wild type, Panel A; rBMC, Panel B) appeared heterogeneous in shape. No obvious size differences were observed between wild type and rBMC structures. However, the high resolution AFM scans of wild type and rBMCs revealed the presence of structures (Figure 4.7 and Figure 4.8), that appear to show budding. Such an event has been reported previously during β-carboxysome biogenesis (Chen *et al.*, 2013; Cameron *et al.*, 2013). As described in Section 1.2, budding events are thought to play a major role in the biogenesis of BMCs. The biogenesis of carboxysomes was shown to be initiated by the nucleation of RuBisCO. The nucleate forms a procarboxysome. Next, BMC shell proteins surround the procarboxysome and cut off excess RuBisCO. The excess of nucleated RuBisCO, in proximity to the mature carboxysomes, acts as a nucleation zone for future

carboxysome biogenesis (budding event). Such budding events are shown in Figure 4.8 (particle 2 of wild type and rBMC). More detail, which can be seen in Figure 4.7, shows a single rBMC particle undergoing a budding event.

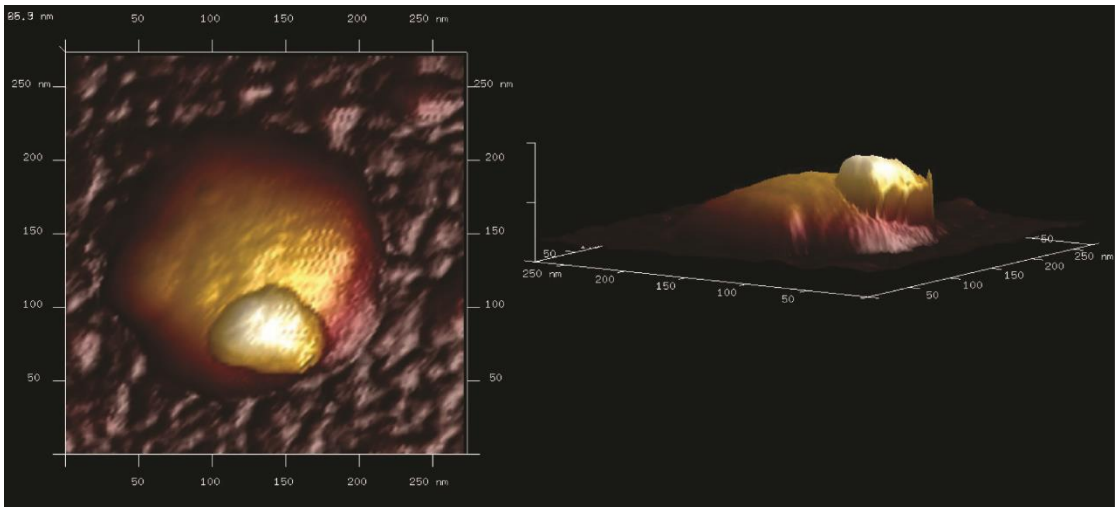

Figure 4.7. Budding event of a single rBMC structure in AFM. **LEFT** Top view of a single rBMC particle, 270 *x* 270 nm (autoscale setting, top view). **Right** Side view of a single recombinant Pdu microcompartments (rBMC, 270 *x* 270 nm each) from left.

Figure 4.7 shows a smaller, approximately hexameric, structure sitting on top of a mature rBMC. The observation of buds (wild type and rBMCs) suggest the purification of BMCs at different maturation stages.

Next, eBMC structures were compared (Figure 4.8). All tested eBMC variants (A-U, Panel C; mA-U, Panel D; and A-T, Panel E) appeared irregular in shape and heterogeneous in size. Due to the variety in size and shape, it was difficult to determine structural differences between eBMC variants. Wild type and rBMCs appeared larger than the eBMC variants in negative stain TEM (Figure 4.3) and AFM (Figure 4.8).

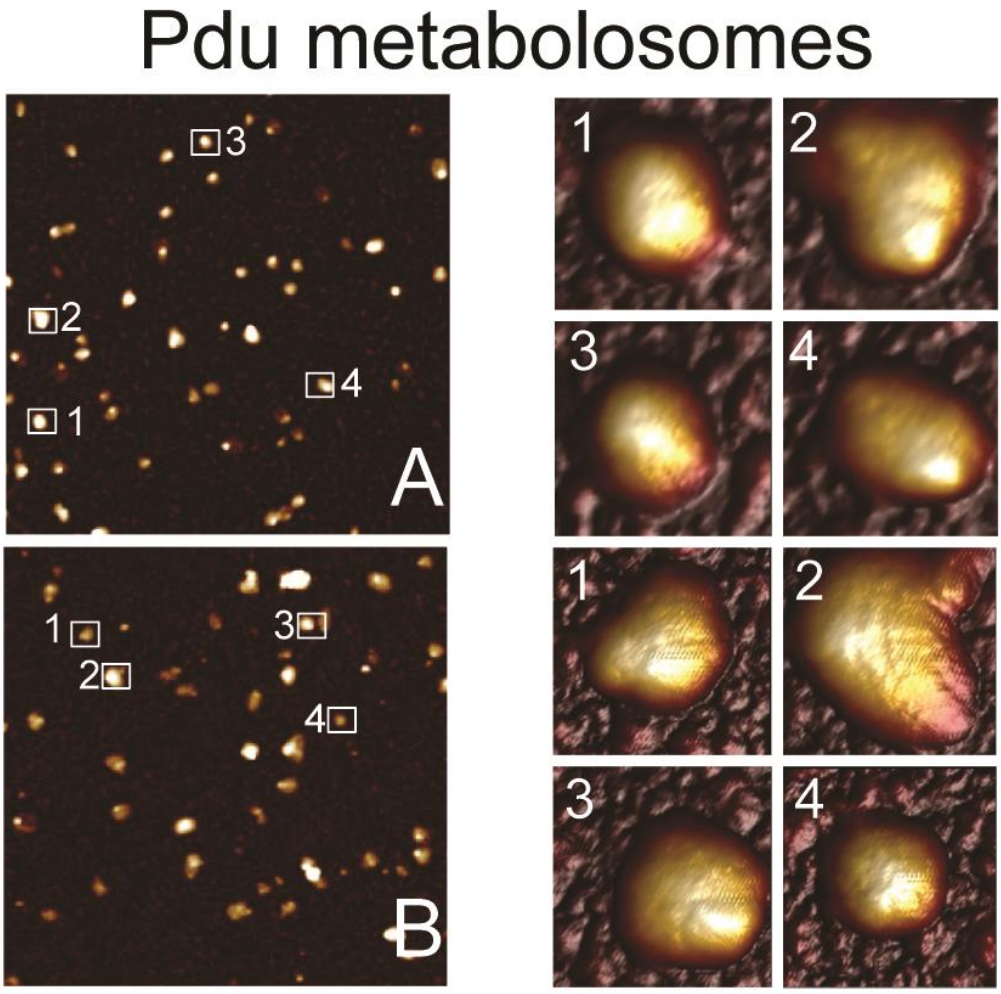
Pdu metabolosomes
3
2
4
1
A
1
3
2
4
B
1
2
3
4
1
2
3
4

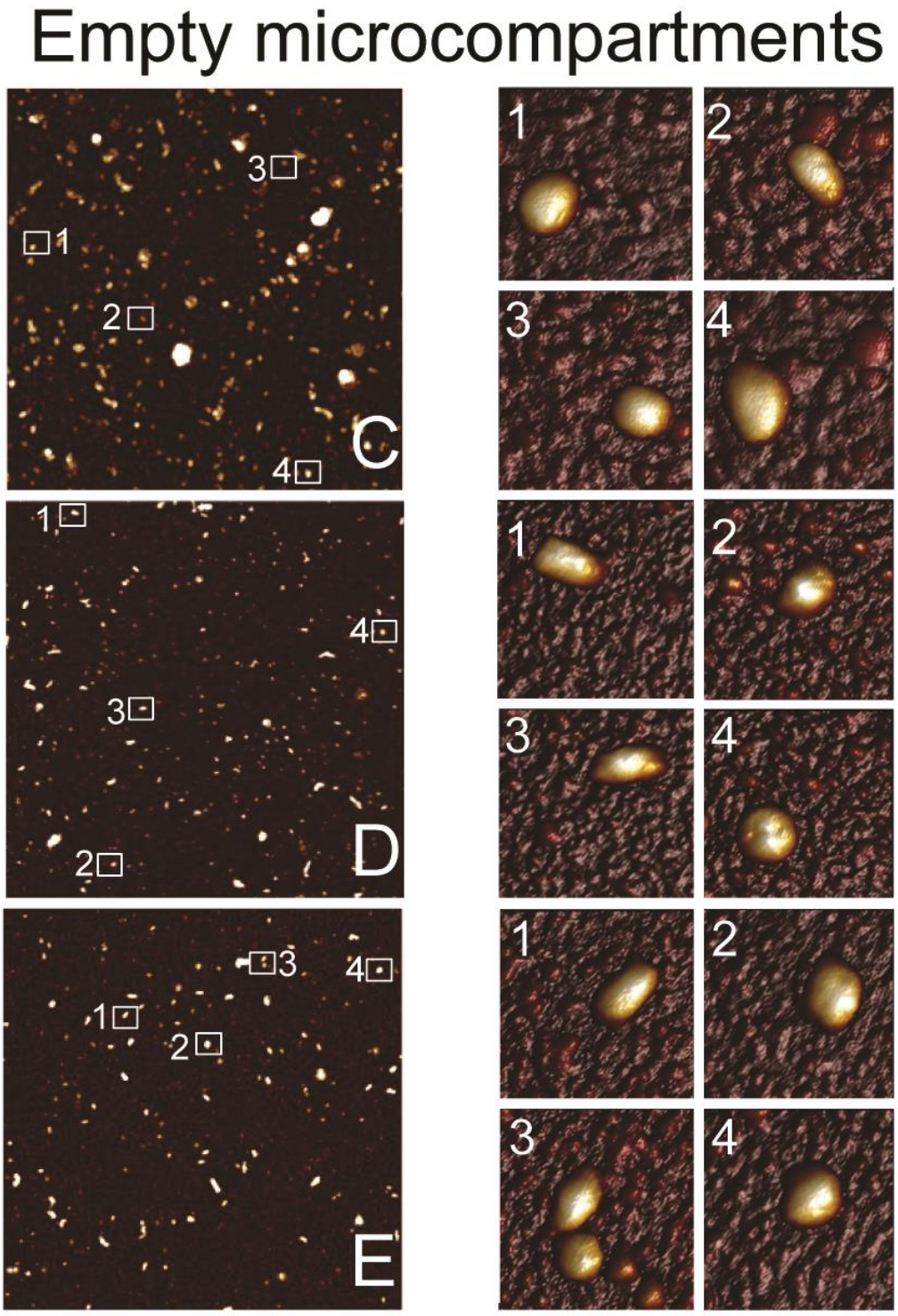

Figure 4.8. Topological AFM images of Pdu microcompartments. **(LEFT)** Overview of zoomed in 4 *x* 4 µm height AFM scans (autoscale setting). White squares resemble crop outs for in-detail view. **A.** Purified Pdu metabolosomes (wild type), extracted from *C. freundii*. **B.** Purified Pdu metabolosomes (rBMC), extracted from *E. coli.* **C.** Purified empty microcompartments (A-U), extracted from *E. coli*. **D.** Purified empty microcompartments (mA-U), extracted from *E. coli*. **E.** Purified empty microcompartments (A-T), extracted from *E. coli* **(RIGHT)** In-detail height images of single Pdu microcompartments (240 *x* 240 nm each) from overview.

To characterise and quantify differences between all the tested Pdu microcompartments, TEM images (Section 4.3) and AFM scans were used to measure single particles and quantify structural differences.

4.5. Single particle analysis of Pdu microcompartments

The size distribution of Pdu microcompartment structures is vital in order to understand nature`s design principles for BMC systems. The characterisation of size distribution by single particle analysis can assist the elucidation of driving forces for self-assembly. By using single particle analysis, differences between wild type *C. freundii* BMCs and the reported size of *S. enterica* BMCs can be compared. Likewise, wild type BMCs from *C. freundii* can be compared to rBMCs formed in *E. coli*. Similarly, the different eBMC variants (A-U, mA-U and A-T) can be compared in order to determine the effects of missing BMC building blocks and to analyse structural effects of the mCherry-PduA fusion on size distribution.

The average diameter and area of TEM images and AFM scans were measured in ImageJ v.1.48 (Section 2.10). The peak height (AFM only) was measured in Nanoscope v1.40. More than a 100 single particles (individually for TEM and AFM) were measured for each tested BMC (wild type, rBMC, A-U, mA-U and A-T).

Analysis of variance (ANOVA) was conducted by a single-step, multiple comparison procedure (Scheffe`s method, in collarboration with Wei-Feng Xue). No significant differences were found between the AFM and EM data sets for all Pdu microcompartments (wild type, rBMC, A-U, mA-U and A-T) that were analysed.

From TEM and AFM data sets the diameter, area and peak height of Pdu BMCs (wild type and rBMC) were compared. The average diameter of *C. freundii* wild type Pdu BMCs was found to range from 94 to 175 nm (Figure 4.8). The isolated rBMC structures showed a slightly wider variability (72 to 201 nm) but the average values

for diameters of Pdu metabolosomes (wild type and rBMC) were alike (122-131 nm). The average values of wild type BMCs and rBMC derived from *C. freundii* are consistent with the reported average diameter of the Pdu BMCs from *S. enterica* (123 ± 30 nm) (Cheng *et al.*, 2011).

To take the heterogeneous and irregular appearance of Pdu BMCs into account, the area, rather than diameter of wild type and rBMC particles was measured and compared. The area of individual wild type Pdu BMCs ranged from 0.008-0.016 μm^2. Single particles of rBMCs were observed from 0.004-0.03 μm^2. As with the average diameter, rBMC particles showed a higher variation in area size. The average area size of wild type and rBMCs (0.012-0.014 μm^2) showed no statistical difference.

In addition to 2D-parameters, peak height values from the AFM scans of wild type and rBMC particles permitted the 3D comparison of BMC particles (Figure 4.8). The peak height of individual Pdu microcompartments was smaller than the radius. This suggested that particle distortion may have occurred during sample deposition. Nonetheless, the peak height information still provided some new information concerning the size distribution of Pdu microcompartments. The peak height of wild type and rBMC particles ranged from 36 to 78 nm, with an average peak height of 49-50 nm. As observed previously with both diameter and area, no significant differences were observed between wild type and rBMC structure (Figure 4.8).

The determination of the average diameter, area and peak height of wild type Pdu BMCs and rBMC particles did not detect significant differences between them. Therefore, Pdu BMCs (wild type and rBMCs) are very similar and form one size cluster of Pdu microcompartments. These structural observations are consistent with the proteomic analysis in Section 3.5, which shows a high degree of similarity between wild type and rBMCs in terms of their protein composition.The slightly greater variation in diameter and area of rBMCs might be a consequence of differences between the host organism *C. freundii* and *E. coli*, or a consequence of making unnaturally large numbers of rBMCs in the cytoplasm (Section 3.3). The heterogeneity of Pdu BMC (wild type and rBMC) particles in diameter, area and height suggest the formation of irregular structures.

In parallel with the analyses of wild type and rBMC structures, the eBMC variants (A-U, mA-U and A-T) were also compared. The size distribution of eBMCs was quantified and reported in Figure 4.9.

As with wild type BMCs and rBMCs, a wide variety of sizes were observed with all the eBMC variants (17-186 nm). Despite this variability, the eBMC variants had an average diameter between 40 and 80 nm. Importantly, no significant differences were observed for the average diameter values of A-U, mA-U and A-T. The average diameters of eBMC variants ranged between 56 and 77 nm.

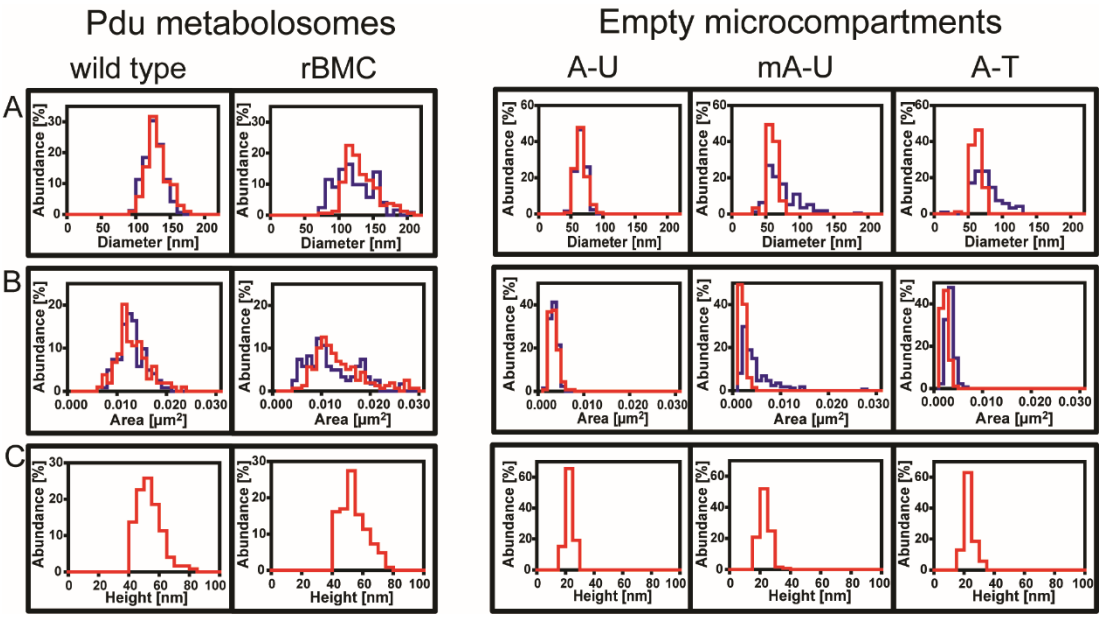

Figure 4.9. Single particle analysis of diameter, area and height of Pdu microcompartments. **A.** Diameter distribution of normalised data of TEM (blue) and AFM (red), bin of 10 nm. **B.** Area distribution of normalised TEM (blue) and AFM (red) data, bin of 0.001 µm^2. **B.** Height distribution of normalised AFM data, bin of 5 nm red line.

As with wild type and rBMC particles, the cross-sectional areas of all three tested eBMCs were compared (Figure 4.9). Interestingly, no significant differences in area size between A-U, mA-U and A-T were identified. The vast majority of all tested eBMC variants ranged between 0.001 and 0.006 µm^2 and average values were obtained between 0.0025 µm^2 and 0.0049 µm^2. These differences were not significant.

Finally the peak heights associated with the eBMC variants were compared (Figure 4.9). All eBMC variants appeared distorted, as their peak heights were smaller than their diameter. The peak height of the eBMC particles ranged from 12 to 37 nm. Average values of all three eBMC were alike with peak heights of 18-19 nm.

The size distribution of all the eBMC variants revealed that they were all similar in terms of diameter, area and peak height. This study provides the first initial structural insights into the stability of eBMC assembly and allows several conclusions to be made. Firstly, reducing the set of building blocks from A-T to A-U had no structural consequences in size distribution. Secondly, the fusion of mCherry onto PduA had no effects on size distribution either. The size variation of eBMCs in terms of diameter, area and peak height may reflect the purification of eBMCs at different maturation stages, as it has been suggested for wild type and rBMCs.

As mentioned in Sections 4.3 and 4.4, significant size differences were observed between Pdu BMCs (wild and rBMCs) and empty BMCs (A-U, mA-U and A-T). The average diameter of all tested eBMC variants was approximately half of that observed for wild type and rBMC particles. The average area of eBMC variants was approximately 1/3 of the average area of Pdu BMCs (wild type and rBMC). The average peak height of all eBMC variants was almost 40% of the average peak height of Pdu BMCs (wild type and rBMC).

All eBMC variants formed smaller particles (average diameter, area and peak height) in comparison to Pdu BMCs (wild type BMCs). The structural differences could be a consequence of altered shell composition (described in Chapter 3) or a consequence of lacking internalised enzymes. To test this, the nano-mechanical stability of the eBMC variants was compared to the stability of wild type and rBMC structures.

4.6. Classification of Pdu microcompartments by quantitative nano-mechanical mapping

As well as recording 3D topographical measurements, AFM can also monitor further biophysical parameters, such as nano-mechanical properties of biological samples. Prior to such compression studies, it is vital to determine the deflection sensitivity and calibrate the spring constant using a thermal tune protocol of the probe and to measure the tip-radius using an absolute method (Section 2.10).

The non-invasive manner of AFM for BMC peak height measurements was confirmed by compression studies at low forces (0.2-2.0 nN). In this control experiment, no difference in height were recorded (data not shown). Furthermore, no reduced Derjaguin-Muller-Toporov (DMT) modulus data, describing sample stiffness, were recorded. No deformation values were obtained for the Pdu microcompartment samples (wild type, rBMC, A-U, mA-U, A-T). This confirms that AFM is a non-invasive tool for the topological measurement of Pdu microcompartments.

In a follow up experiment, the various Pdu microcompartment structures were subjected to force titration in order to identify the force ranges to allow for comparative compression studies. In this respect 250 nN was identified as sufficient force to measure the reduced DMT modulus and deformation. As with the single particle analysis in Section 4.5, wild type BMCs have been compared to rBMC particles and the eBMC variants (A-U, mA-U and A-T). For each particle class 20 individual peak values of nano-mechanical properties (reduced DMT modulus and deformation) were measured in Nanoscope v.1.40 (Figure 4.10).
The quantification of these two nano-mechanical properties gave some unexpected results. As shown in Figure 4.10, Pdu BMCs (rBMCs and wild type) showed a lower rigidity (5.0-5.4 Gpa), in comparison to the eBMC variants (A-U, mA-U and A-T). The reduced DMT modulus for eBMC structures ranged from 22.8-29.8 GPa. No significant differences were observed for Pdu BMC particles (wild type and rBMC) and eBMC variants (A-U, mA-U and A-T). On the other hand, significant differences were observed between Pdu BMC particles and eBMC variants.

Figure 4.10 shows that the more elastic Pdu BMCs (according to DMT modulus) are more flexible to deformation (2.9-3.0 nm). In contrast, the stiffer eBMC variants only deformed 1.7-1.9 nm at an applied force of 250 nN.

No significant differences in deformation were observed between wild type and rBMC particles. Thus, the recombinant production of BMCs does not appear to affect their size or properties. The same applies to eBMC variants. The fusion of mCherry to PduA (mA-U) and the presence of PduT (A-T) did not result in nano-mechanical changes in comparison to A-U. Significant differences were observed between the eBMC variants and complete Pdu BMCs. Quantitative nano-mechanical mapping suggests that eBMCs form more stable structures in comparison to larger Pdu BMC structures.

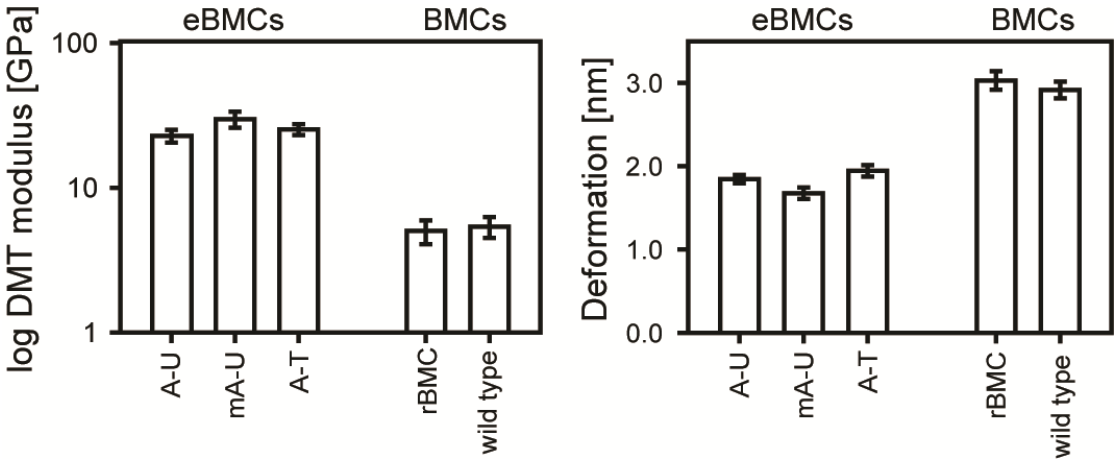

Figure 4.10. Quantitative nano-mechanical mapping of Pdu microcompartments. Average values (N=20) and standard error of mean for reduced DMT modulus [GPa] and deformation [nm] are given.

Topological and nano-mechanical information reveals that larger Pdu BMC structures (wild type and rBMC) are less stiff and more flexible than the eBMC variants. The proteomic shift from PduB`, in wild type and rBMCs, to PduA in the eBMC variants could be associated with the nano-mechanical stiffness and decrease deformation of the empty compartments (Section 3.5). Alternatively, the higher stability of eBMC structures could be caused by the specific or unspecific incorporation of cytoplasmic material in eBMCs. To test this, the internal structural organisation of Pdu microcompartments was investigated by using TEM to determine the presence of encased proteins by thin sectioning purified BMCs.

4.7. Internal structural organisation and Pdu microcompartments

4.7.1. The internal structural organisation of eBMC and BMC structures according to TEM

Microcompartments were extracted from overnight cultures and purifed (Sections 2.6.7, 2.6.11 and 2.6.12). After precipitation, pellets containing mainly BMCs were fixed and embedded in low viscosity resin. Samples were thin sectioned and spotted onto carbon coated grids and visualised by TEM (Section 2.10.1).

Wild type Pdu BMCs were compared to rBMCs (Figure 4.11). Both structures showed an intact outline with a pentameric or hexameric shape. Particles appeared heterogeneous, as described in Sections 4.3 and 4.4, and sampled diameter and area values corresponded to the analysis in Section 4.5 (data not shown). The lumen of wild type Pdu BMCs and rBMC appeared highly electron dense with granular spots. Such density would be consistent with the physiological role of Pdu microcompartments to sequester enzymes for 1,2-PD utilisation and reaction factors within an intact proteinaceous shell. No higher order was observed for the internal structural organisation of wild type and rBMC structures in negative stain TEM.

The eBMC variants (A-U, mA-U and A-T) showed intact outlines that appeared heterogeneous in size and shape as observed previously in Sections 4.3 and 4.4. Diameter and area values of single eBMC structures as thin sections of wild type and rBMCs were consistent with reports in Section 4.5. In contrast to the wild type and rBMCs, all eBMC variants showed low electron density in the lumen. This suggests that eBMCs form hollow structures. The formation of intact and hollow structures is not affected by the presence of PduT or mCherry fused to PduA. These observations support the hypothesis that eBMCs form intact but hollow structures.

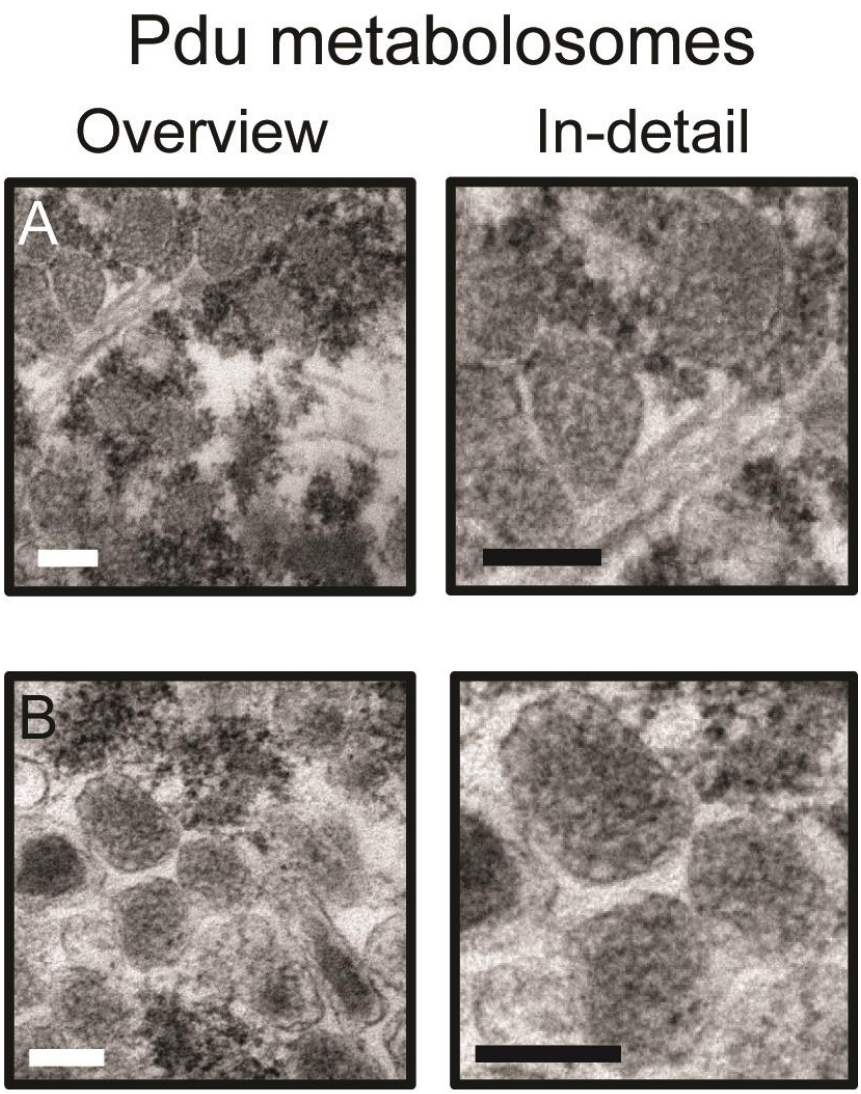
Pdu metabolosomes
Overview
In-detail
A
B

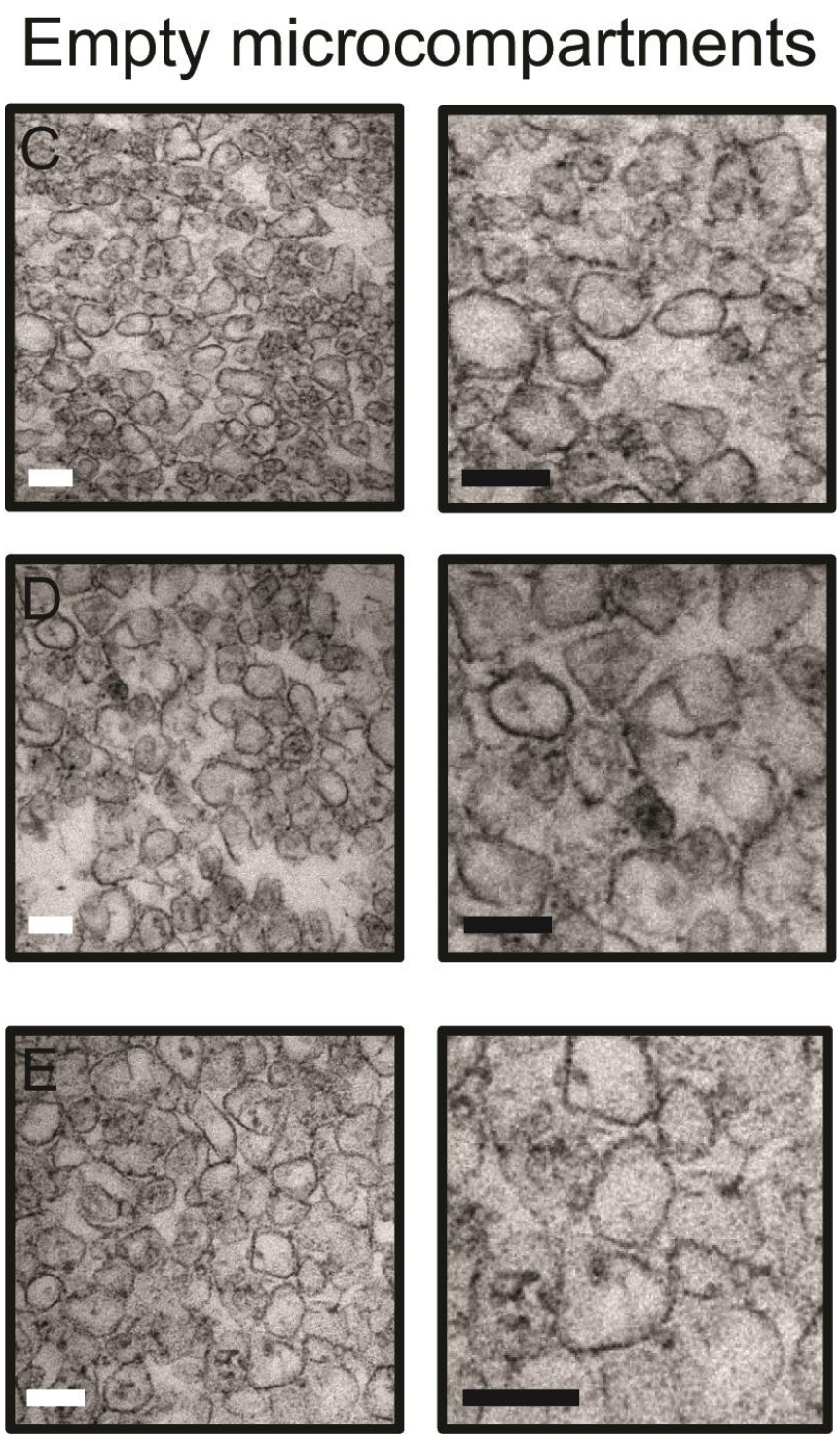

Figure 4.11. Electron microscopy images of sectioned and purified Pdu microcompartments. Section thickness of 70 nm. **LEFT** Overview of thin sectioned Pdu microcompartments. **RIGHT** In-detail view of thin sectioned Pdu microcompartments. **Panel A.** Purified wild type Pdu BMCs, extracted from *C. freundii*. **Panel B.** Purified rBMCs, extracted *from E. coli*. **Panel C.** Purified A-U eBMC, extracted from *E. coli.* **Panel D.** Purified mA-U eBMC, extracted from *E. coli*. **Panel E.** Purified A-T eBMC, extracted from *E. coli*. Scale bars correspond to 100 nm.

4.7.2. The intact and hollow structure of a eBMC in cryo-tomography

The structural analysis of Pdu microcompartments was investigated further using cryo electron-tomography (in collaboration with Dr. Lorna Hodgson and BSc. Judith Mantell, University of Bristol). Cryo-tomography imaging allows the 2D data acquisition of freeze dried Pdu microcompartments, by rotation of the electron beam (Figure 4.12). 2D images can then be reconstructed to a 3D model.

In cryo-tomography, A-U particles showed an intact outline with pentameric to hexameric symmetry. The particle sizes are consistent with the diameters and areas reported by negative stain TEM in Section 4.3 and 4.5. The eBMC (A-U) appears hollow in cryo electron-tomography. This provides further evidence that the A-U eBMC represents an empty protein capsid and shows the potential of cryo-tomography to study the overall structure of BMC structures in general (Bai *et al.*, 2015).

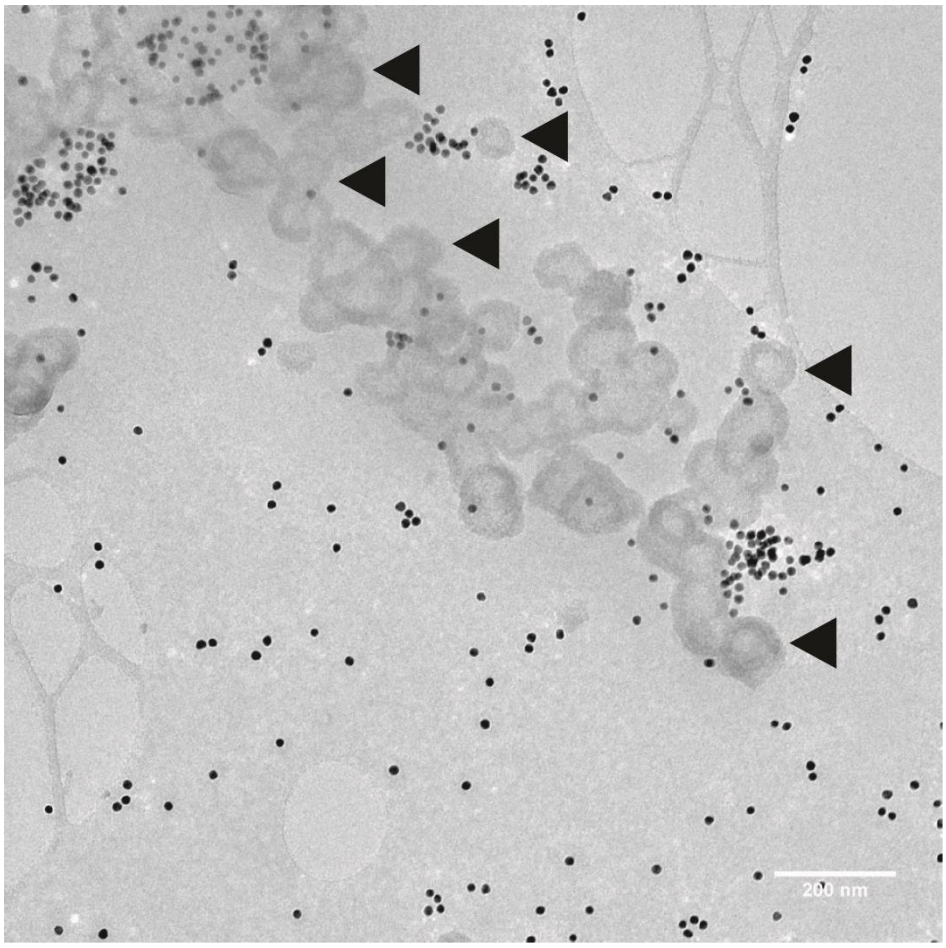

Figure 4.12. Intact and hollow structure of one eBMC variant in cryo electron microscopy. Structures of eBMCs (A-U) are highlighted by arrows. Black dots correspond to gold particles for tracing during z-series.

4.8. Discussion

In the previous chapter proteomic differences between wild type, rBMCs and the eBMC variants were identified. This chapter focussed on the biophysical characterisation of size, nano-mechanical properties and internal structural organisation of the various compartments. Different EM and AFM techniques have been employed to investigate the nature and biophysical properties of Pdu microcompartments. In contrast to the structure of the anabolic carboxysomes, Pdu BMCs appear irregular in size and shape. Differences in size and nano-mechanical properties between wild type and rBMC particles and the tested eBMC variants were quantified. From these studies it can be concluded that eBMCs are hollow, more rigid and less flexible than the more densely packed wild type and rBMC particles.

In addition to the characterisation of the Pdu microcompartment particles, filamentous structures were co-purified with both wild type and rBMCs. Two Pdu related proteins are reported to form filamentous structures, PduA which can self-assemble into nano-tubular structures and PduV which is thought to have a role in filament-coordinated metabolosome movement in the cell (Frank *et al.*, 2013; Chowdhury *et al.*, 2014). However, the protein identity of the observed filamentous structures has yet to be assigned.

The observation of budding events requires further experimental back-up. The observation of buds on Pdu BMCs still represents an important development in the characterisation of Pdu BMCs. Budding of BMCs is thought to be a consequence of the BMC shell surrounding its cargo (Section 1.2). The observation of budding events suggests that Pdu BMCs pinch off excess cargo material. The excess material acts as a nucleus for the biogenesis of further BMCs (Chen *et al.*, 2013; Cameron *et al.*, 2013). However, eBMCs are capable of forming in the absence of any cargo and no buds were observed for eBMCs. Further information on the frequency of buds and the timing of their appearance will provide greater insight into the maturation process associated with BMCs.

Interestingly, no size differences were observed between wild type particles from *C. freundii* and those from *S. enterica* (Cheng *et al.*, 2011). Likewise, the heterologous formation of Pdu BMCs from *C. freundii* in *E. coli* (rBMCs) had no effects on the average particle size, nano-mechanical properties and internal structural organisation.

Similarly, no structural differences in size were identified for the eBMC variants. A full set of Pdu shell proteins (A-T) was compared to a reduced set of building blocks (A-U) and labelled building blocks (mA-U). All of them were shown to form particles of the same general size, quantitative nano-mechanical properties and internal structural organisation. Biophysical similar structures with regard to eBMC variants and Pdu BMCs (wild type and rBMC) further establish the idea that BMC shell formation is a stable and flexible process.

Despite the similarities between eBMC variants and Pdu BMCs (wild type and rBMC), significant differences were observed in size, quantitative nano-mechanical properties and internal structural organisation (Section 4.3-7). The Pdu BMCs (wild type and rBMCs) are about twice the size of the empty variants. Moreover, they are less stiff and more compressible than the smaller eBMCs.

These physical properties could reflect differences in the shell protein composition where PduB and PduB` are the most abundant BMC shell protein in wild type and rBMC structures, whilst the major BMC shell proteins in all the eBMC variants is PduA. But, it is not understood if differences in shell protein composition or the missing internal protein scaffold cause the observed biophysical differences between Pdu BMCs (wild type and rBMC) and the eBMC variants.

Chapter 5

Investigations into the uptake and accumulation of cobalamin in a bacterial microcompartment

5.1. Introduction

The previous Chapters, 3 and 4, focussed on the proteomic and biophysical characterisation of wild type BMCs, rBMCs and eBMC (A-U). The research objective of this chapter was to investigate a functional aspect of the BMC. In particular, it aims to characterise cobalamin uptake by the BMC and whether the BMC variants have an effect on the process.

Adenosylcobalamin (Ado-B_{12}) is an organometallic (Co) cofactor (Figure 5.1) that contains a modified tetrapyrrole macrocycle, which is closely related to other pigments of life such as haem (Fe), chlorophyll (Mg) and the lesser known coenzyme F_{430} (Ni) (Raux *et al.*, 2000; Banerjee; Ragsdale, 2003). Cobalamins are composed of three core structural components: (I) A corrin ring, (II) a lower nucleotide loop and (III) an upper ligand. The corrin ring donates four ligands to the central cobalt ion. The lower (α) ligand is usually donated by 5,6-dimethyldbenzimidazole (DMB), which is within the nucleotide loop. The upper (β) ligand is the sixth binding partner for the central cobalt ion and plays a key role in the biological activity of the molecule. Methylcobalamin (Me-B_{12}) and adenosylcobalamin (Ado-B_{12}) represent the two major biological forms of cobalamin. Hydroxycobalamin (OH-B_{12}) and the artificial cyanocobalamin, better known as vitamin-B_{12}, represent inactive forms of cobalamin. Inactive forms of cobalamin can be assimilated (vitamin-B_{12}) or reactivated (OH-B_{12}) to Ado-B_{12}. More recently, cobalamin, with no upper ligand, has been shown to be the active form in reductive dehalogenases (Payne *et al.*, 2014).

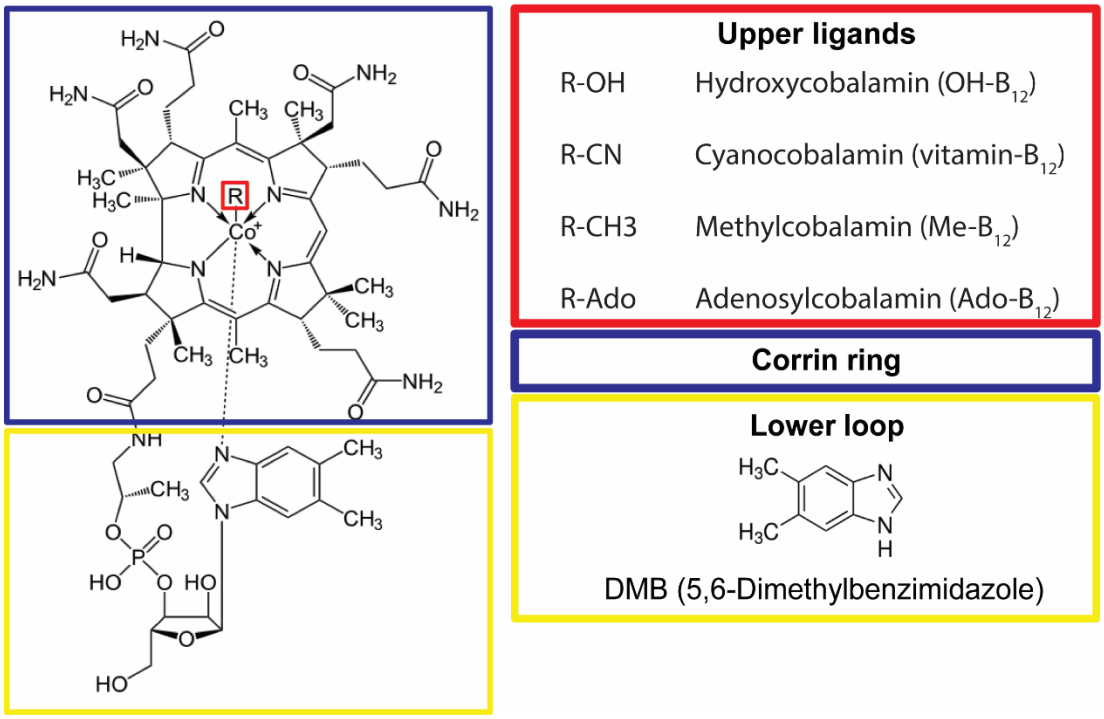

Figure 5.1. Cobalamin structure. Cobalamins are distinguished by their β-ligand (red), corrin ring (blue) and α-ligand (yellow).

A number of BMCs house cobalamin-dependent processes. Both the Pdu and Eut BMCs contain Ado-B_{12} enzymes in the form of propanediol dehydratases (PduCDE) and ethanolamine ammonia lyase (EutBC), respectively (Havemann; Bobik, 2003; Mori *et al.*, 2004; Chowdhury *et al.*, 2014). Both BMCs also house a set of Ado-B_{12} reactivation factors for cobalamin assimilation and reactivation. The reactivation enzymes (PduGH, PduO and PduS) have been suggested to increase the availability of Ado-B_{12} in spatial proximity to the Ado-B_{12}-dependent propanediol dehydratase (PduCDE). The Ado-B_{12} dependent degradation of 1,2-PD and Ado-B_{12} reactivation are described in Section 1.5.2. However, it is not known how cobalamin enters the BMC, although EutL would appear to be able to bind to cobalamin in the Eut metabolosome (Thompson *et al.*, 2014). The crystal structure of EutL from *Clostridium perfringens* is a homolog to PduB (PDB code: 4U6I) and was reported to bind cobalamin in the crystal structure. Intriguingly, the binding amino acid residue His32 is not conserved along EutL homologs and therefore the biological relevance of this study is questionable.

5.2. Aims and Objectives

The interaction of Pdu organelles with the cellular cobalamin pool requires the attachment of cobalamin to the shell or its encasement within the metabolosome but no experimental evidence has been provided as to how this might occur. In this chapter, the ability of BMCs, both *in vivo* and *in vitro*, to associate and potentially accumulate cobalamin is investigated, in order to provide the first firm evidence for a cobalamin accumulation process.

5.3. Association of soluble cobalamins with Pdu microcompartments *in vitro*

An *in vitro* approach was applied to check for the association of different cobalamins with Pdu microcompartment structures rather than the individual shell proteins. Strains producing wild type BMCs, rBMCs and eBMCs (A-U) were grown overnight to allow the production of the intracellular macromolecular structure.

After cell lysis using B-PER™ (Section 2.6.12) and Y-PER™ (Section 2.6.11) and the first centrifugation step, cobalamin (2 µM, Ado-B_{12}, Me-B_{12}, OH-B_{12} and vitamin-B_{12}) was added to the BMC containing solution and equilibrated at 4°C. After 30 min, the Pdu microcompartments (wild type, rBMC and eBMC) were purified.

The cobalamin content of the purified Pdu microcompartments was compared to the initial cobalamin content by LC-MS, as reported in Figure 5.2.

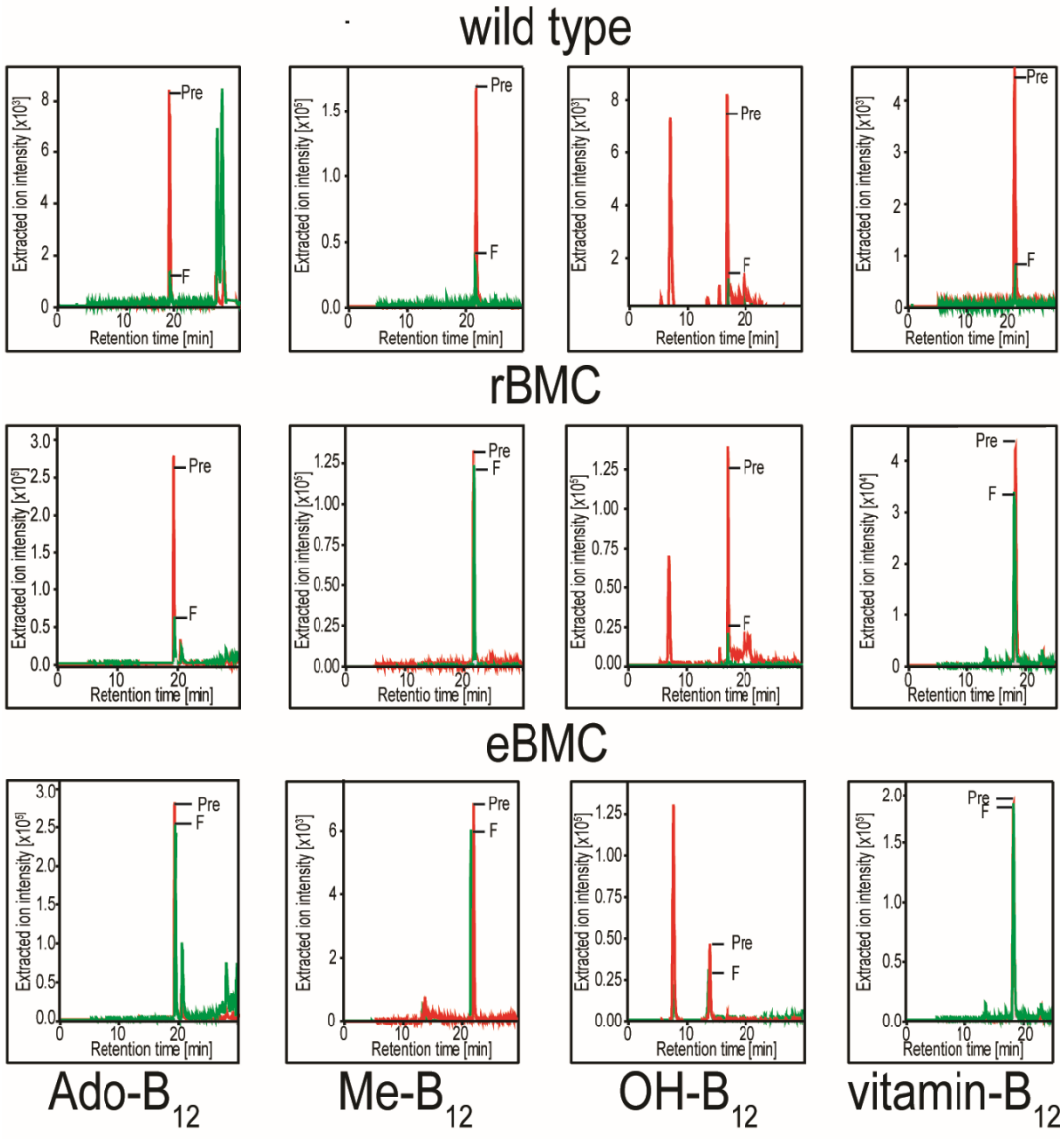

Figure 5.2. Co-precipitation of different cobalamins with Pdu microcompartments (eBMC, rBMC and wild type). The figure shows the extracted ion chromatograms of co-precipitated cobalamins. Labelled peaks correspond to different cobalamins (Ado-B_{12}, Me-B_{12}, OH-B_{12} and vitamin-B_{12}) that purified with wild type, rBMC and eBMC, purified fraction (F, green) and initial concentration (Pre, red). Extra peaks on the chromatogram likely correspond to sample impurities not related to cobalamin according to retention time and UV-Vis.

According to the retention time and the extracted ion chromatogram in Figure 5.2, wild type and rBMC structures co-precipitated with all tested cobalamins. The association of cobalamins with wild type and rBMC structures suggests an ability of the organelle to associate with cobalamins.

Similarly, according to the retention time and the extracted ion chromatograms of the eBMC structures, Ado-B_{12}, Me-B_{12}, OH-B_{12} and vitamin-B_{12} were all found to associate with this empty microcompartment structure.

The co-purification of cobalamins with the Pdu BMCs (wild type, rBMC and eBMC) was not due to the use of different protocols as both the B-PER™ and Y-PER™ protocols were employed. Similarly, the association of cobalamin was not dependent on the presence of internalised Ado-B_{12} dependent enzymes and reactivation factors. Instead, the association of cobalamins with the tested BMC structures (wild type, rBMC and eBMC) suggests an inherent ability of the BMC shell itself to bind cobalamins. To investigate this further, an *in vivo* system was developed to study the intracellular cobalamin pool in the presence of Pdu microcompartments.

5.4. Growth in minimal media results in enhanced uptake of vitamin-B_{12} in *C. freundii*

Detecting cobalamin is often limited by the low levels that are found associated in biological samples. LC-MS, for instance, has a detection limit of around 0.1 µM. Utilising biological systems that can accumulate cobalamin above this level are therefore desirable. In this section methods were applied that allowed for cells to accumulate more cobalamin.

Initially, both *E. coli* and *C. freundii* were grown in minimal medium (NCE) that contained 1 µM exogenous vitamin-B_{12} (Section 2.4.1 and Section 2.6.8). As shown in Figure 5.3, the *E. coli* cell pellet displayed no coloration that would indicate high cobalamin uptake.

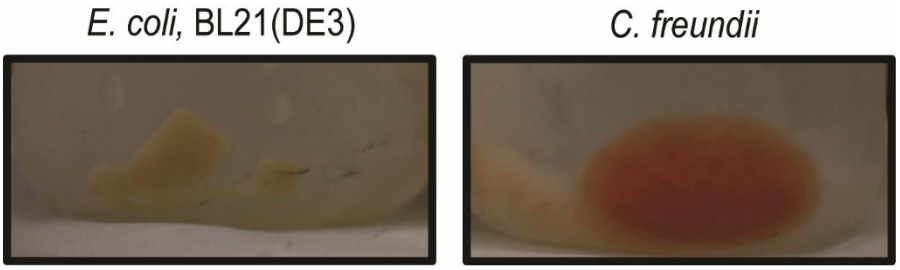

Figure 5.3. Evidence of increased cobalamin uptake in *C. freundii* when grown in minimal medium.

In contrast, the cell pellet of *C. freundii* grown in minimal medium was strongly orange / red coloured. The coloration of the pellet suggested uptake of vitamin-B_{12}. The presence of cobalamin was confirmed by LC-MS (Section 5.7 and 5.9). The differences in medium culture between C*. freundii* and *E. coli*, which are closely related phylogenetically, were not further investigated. Instead, methods were developed to improve cobalamin-uptake in *E. coli,* in order to allow a more direct comparison of recombinant Pdu microcompartment systems (rBMC and eBMC) to wild type.

5.5. Deregulation of vitamin-B_{12} uptake in *E. coli* by homologous overproduction of BtuB

Cobalamin-uptake in *Enterobacteriaceae* is regulated through a riboswitch control element of the outer membrane tranporter gene *btuB* (Gallo *et al.*, 2008). Dr. Evelyne Deery deregulated cobalamin uptake by the homologous overproduction of BtuB in *E. coli* (BL21(DE3), Figure 5.4, unpublished data). As observed with *C. freundii* grown in minimal medium, cell pellets of *E. coli* overproducing BtuB showed a strong coloration when fed with 1.0 µM vitamin-B_{12} in contrast to control samples. The presence of intracellular cobalamin was confirmed by LC-MS in Sections 5.7 and 5.9.

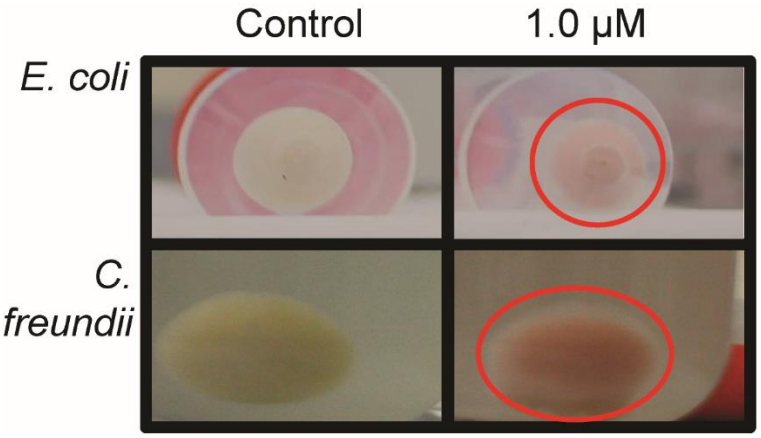

Figure 5.4. Deregulation of cobalamin uptake in *E. coli* by homologous overproduction of the outer membrane transporter protein BtuB. Uptake was compared to *C. freundii* grown in NCE minimal medium.

The increased uptake of cobalamin established an *in vivo* system to study the intracellular cobalamin pool of wild type *C. freundii* forming native BMCs and in *E. coli* forming rBMC and eBMC structures.

5.6. Effect of Pdu microcompartments on cobalamin uptake into the cell

Control strains (*C. freundii* (-1,2-PD) and *E. coli* (+BtuB)) and strains producing wild type Pdu BMCs (*C. freundii* (+1,2-PD)), rBMCs and eBMCs (A-U) were grown overnight, in the presence of low concentrations of vitamin-B_{12} [0.1 µM]. The cells were harvested by centrifugation. The cell pellet was washed twice with buffer A (Section 2.8.5 and Section 2.6.12) to separate extracellular cobalamin from the cell pellet. The cell pellet was resuspended in buffer A and lysed by heat (10 min at 95°C). Cell debris was pelleted by centrifugation (10 min at 13,000 rpm). The supernatant was acidified with TFA to a final concentration of 0.1% (v/v). Protein was pelleted by centrifugation. The final supernatant was analysed by LC-MS.

Analysis of the lysate of *C. freundii* grown in minimum medium and in the absence of 1,2-PD *i.e.* in the abscence of BMCs, resulted in the accumulation of Ado-B_{12}. This indicates that *C. freundii* has a good cobalamin uptake system and that it is able to convert cyanocobalamin efficiently into the coenzyme form. Similarly, deregulated *E. coli,* which do not produce BMCs, also efficiently accumulated vitamin-B_{12} and converted it into Ado-B_{12}.

In contrast to *C. freundii* and *E. coli* control strains that accumulated Ado-B_{12} in the absence of BMCs, both organisms accumulated vitamin-B_{12}, as the major form of cobalamin in the presence of the organelle. With *C. freundii* grown on 1,2-PD, vitamin-B_{12} was the major form although significant levels of OH-B_{12} were also observed. No Ado-B_{12} was detected. The accumulation of vitamin-B_{12} was more prominent in the *E. coli* strains producing rBMCs and eBMCs. These results were not expected as the BMC would be expected to accumulate Ado-B_{12}, which is the coenzyme form required by the diol dehydratase. In addition, fully functional BMCs contain reactivation factors, such as PduS and PduO, to help produce Ado-B_{12} (Section 1.5.3). It may be that vitamin-B_{12} is accumulated within the BMC, prior to the action of the cytoplasmic enzyme systems that are able to convert it into Ado-B_{12}. However, once in the BMC the organelle does not contain an effective decyanase to help remove the upper cyano ligand. Hence, vitamin-B_{12} accumulates within the BMC.

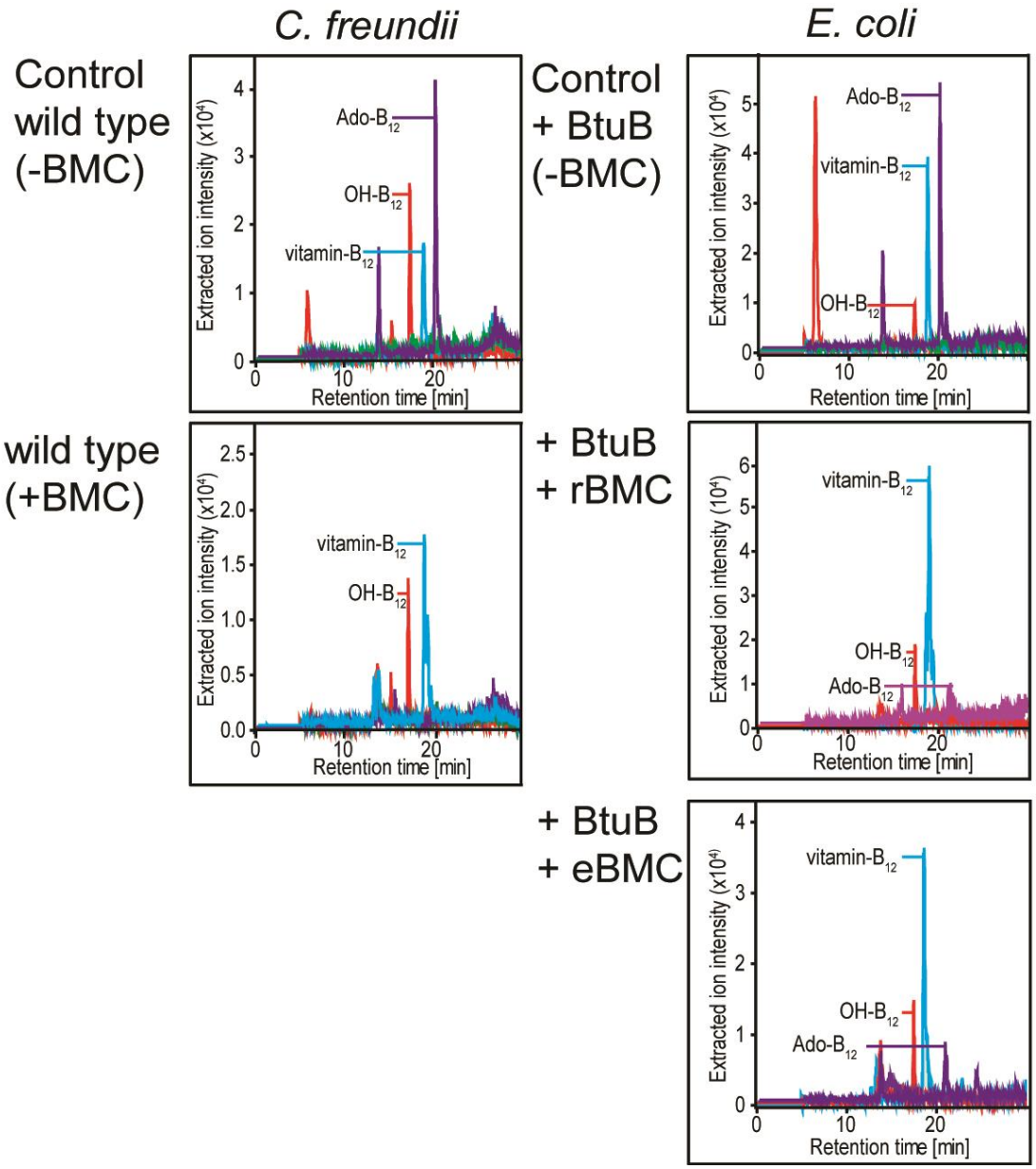

Figure 5.5. Pdu microcompartments alter the intracellular cobalamin pool. Extracted ion chromatogram of control samples without Pdu microcompartments from *C. freundii* (-1,2-PD, -BMC) and *E. coli* (+BtuB), *C. freundii* forming Pdu BMCs (+1,2-PD, +BMC) and *E. coli* forming rBMC (+BtuB, +rBMC) and eBMC (+BtuB, +eBMC) structures in presence of 0.1 µM vitamin-B_{12} in the growth medium. Extra peaks correspond to sample impurities unrelated to cobalamins.

5.7. Sub-cellular cobalamin pool in purified Pdu microcompartments

The previous section (5.7) revealed that cells that contain BMCs are able to accumulate exogenously-added cobalamin. However, the study did not look at the subcellular distribution of cobalamin. Consequently, the Pdu BMCs (wild type, rBMC and eBMC) were isolated and their B_{12} content analysed, from identical cultures as in the previous section. The isolated sub-cellular fraction containing BMCs were analysed by LC-MS (Figure 5.6).

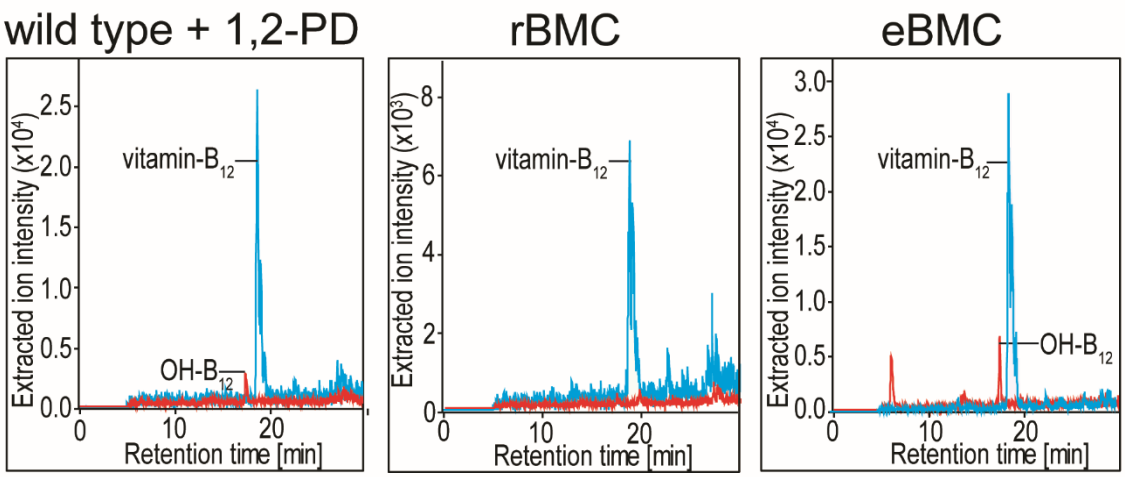

Figure 5.6. Extracted ion chromatogram of purified Pdu microcompartments. Vitamin-B_{12} (blue) and OH-B_{12} (red) traces of purified BMCs (wild type and rBMC) and eBMCs (A-U). Extra peaks correspond to unrelated *m/z* peaks.

The most abundant cobalamin in purified Pdu BMC (wild type and rBMC) was vitamin-B_{12}. Traces of OH-B_{12} were detected in wild type Pdu BMC samples. No traces of Ado-B_{12} were detected. In addition, isolated eBMCs (A-U) contained mostly vitamin-B_{12} and traces of OH-B_{12}. Ado-B_{12} was not detected in isolated eBMC samples. Together with the data presented in Section 5.7, these results indicate that BMCs have an inherent ability to bind cobalamins. Moreover, it suggests that they accumulate vitamin-B_{12}.

5.8. Concentration dependent accumulation of vitamin-B_{12} with Pdu microcompartments

The previous sections provided qualitative evidences for the uptake and accumulation of vitamin-B_{12}. In order to quantitate this, vitamin-B_{12} levels of crude lysate samples were compared to samples of purified Pdu microcompartments after growth and purification of BMCs at different vitamin-B_{12} concentrations in the growth medium.

A range of vitamin-B_{12} concentrations (control, 0.1 µM, 1.0 µM and 10 µM) were fed to *C. freundii* in the presence of 1,2-PD and to *E. coli* strains producing BtuB with rBMC or eBMC (A-U) structures. To quantify any concentration dependent accumulation of vitamin-B_{12} in Pdu microcompartments, crude lysates and purified fractions were sampled. Protein levels (Bradford assay, Section 2.8.1) and volume were taken into account to calculate a ratio of the vitamin-B_{12} levels from purified BMC fractions to crude lysate samples (Section 2.8.1, Figure 5.8). LC-MS samples of crude lysate and purified fraction were prepared and analysed. Vitamin-B_{12} levels were quantified by either UV-Vis absorption maximum at 360 nm or by extracted ion chromatogram (Table 5.1).

Initially the cell pellet of *C. freundii* was compared visually to the purified pellet of wild type Pdu BMCs. Cell pellets of *C. freundii* and *E. coli* show cobalamin coloration at 1 µM and higher (Figure 5.7). Actually, the wild type BMC pellet shows this characteristic coloration even with 0.1 µM vitamin-B_{12} in the growth medium, which is not seen in the bacterial pellet. This visual approach suggests that BMCs are able to accumulate vitamin-B_{12} at a higher rate than the bacterial cell. This observation was quantified by comparing the concentration of cobalamin in cell lysates to purified BMCs (Table 5.1).

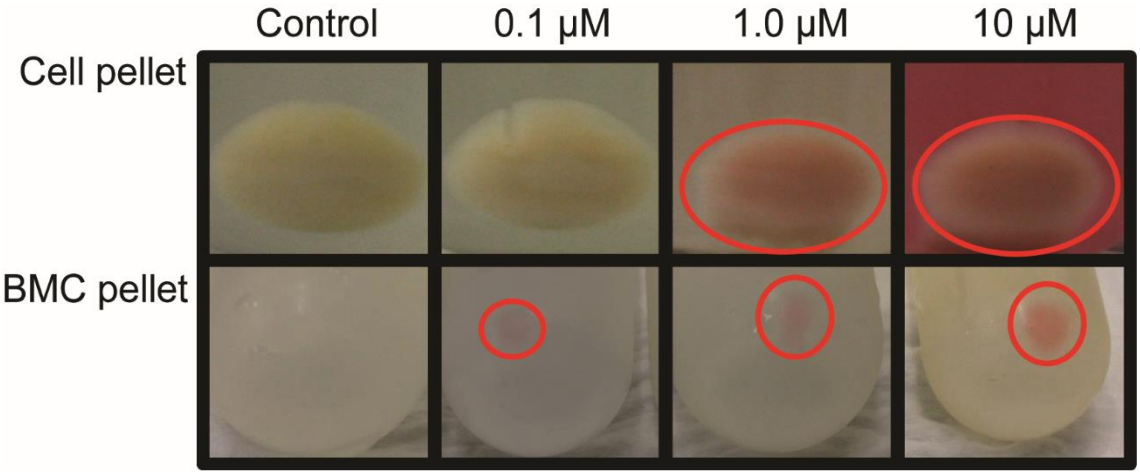

Figure 5.7. Concentration dependent accumulation of cobalamin in BMCs. A visual approach suggests the concentration dependent accumulation of cobalamin in wild type Pdu BMCs. Cell pellets of C. freundii grown in presence of exogeneous vitamin-B_{12} show coloration at 1 µM and higher concentrations of exogeneous vitamin-B_{12} in the growth medium. BMC pellets show coloration at 0.1 µM and higher. Colored pellets are outlined in red.

Wild type Pdu BMCs showed the highest accumulation ratio of 186 (see supplementary and Table 5.1), in comparison to rBMC (57) and eBMC (51), when an external concentration of 0.1 µM vitamin-B_{12} was added to the growth medium. Thus, at low exogeneous concentrations of vitamin-B_{12}, a relatively high proportion of the cobalamin is present in the BMC. As the external concentration of vitamin-B_{12} in the growth medium was increased, so the internal distribution of cobalamin within the cell dropped, presumably as the BMC becomes saturated with cobalamin. This indicates for the specific localisation of cobalamin to the BMC.

Table 5.1. Accumulation studies of vitamin-B_{12} in Pdu microcompartments. Average values and standard error of mean are given (N=2).

Accumulation of vitamin-B_{12}			
	Ratios of [vitamin-B_{12}] in BMC to lysate		
	0.1 µM	**1.0 µM**	**10 µM**
eBMC (A-U)	51 ± 0.1	14 ± 1.6	4 ± 0.6
rBMC (A-X)	57 ± 4.3	27 ± 3.1	10 ± 5.9
wild type	186 ± 47.9	77 ± 1.3	40 ± 2.4

5.9. Fluorescent B_{12}-analogues for fluorescence imaging

In order to follow the partitioning of vitamin-B_{12} into BMCs, attempts were made to generate fluorescent derivatives of cobalamin. Such analogues could potentially be used to follow cobalamin acquisition in real time.

Therefore, fluorescent cobalamin analogues were synthesised, purified and characterised for applications in wide field fluorescence microscopy to follow the regio-specific localisation of cobalamin.

5.9.1. Synthesis of fluorescent B_{12}-analogues

Two different strategies for cobalamin labelling were attempted (Section 2.5). The first strategy involved the replacement of the upper ligand attached to the central cobalt with a short (β-aminopropyl, provided by Dr. Andrew Lawrence) linker. Texas-Red-X succinimidyl ester was conjugated onto the β-aminopropyl upper linker of cobalamin (Figure 5.9). Such upper ligand modifications were chosen to preserve the recognition for cobalamin transporter proteins. The disadvantage of this modification is that the resulting Co-C bound is relatively unstable due to its structural light

sensitivity. Consequently, the synthesised compound was handled under low light conditions.

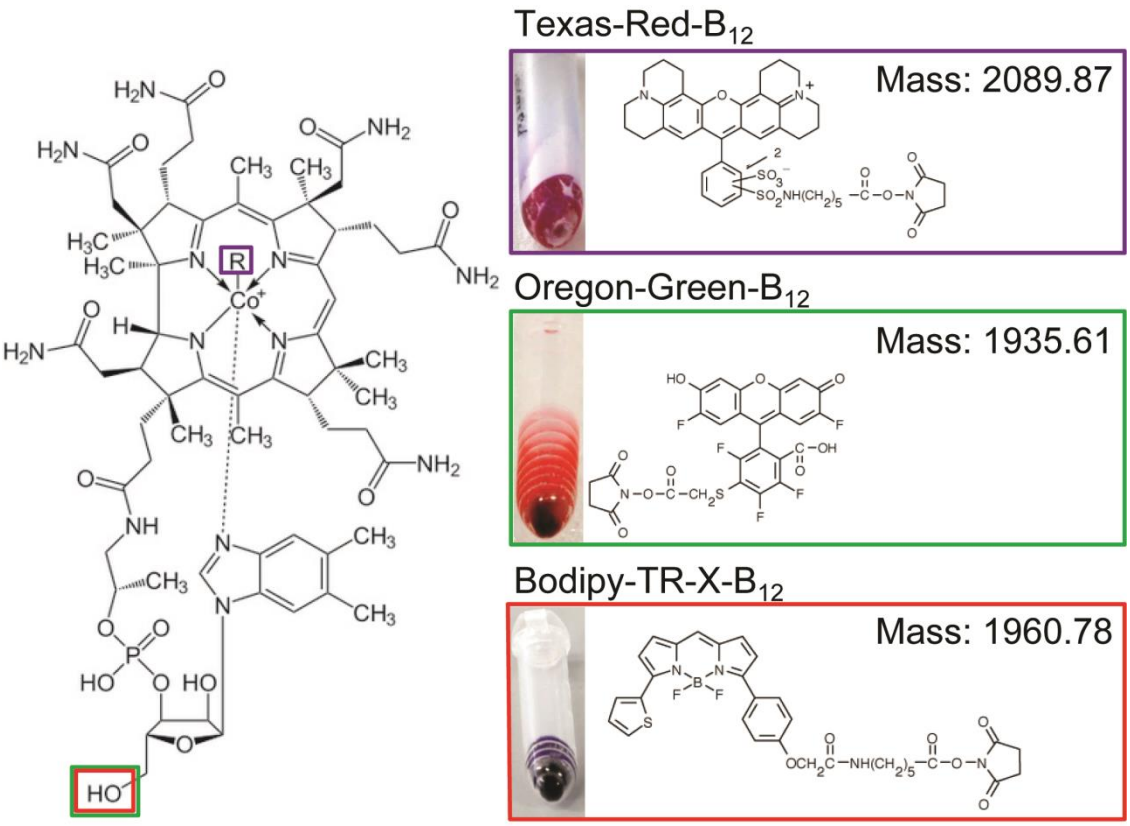

Figure 5.8. Structure of the fluorescent cobalamin analogues. Texas-Red was conjugated to the upper ligand (purple). Lower nucleotide loop analogues were raised by conjugating Oregon-Green (green) or Bodipy-TR-X (red) to Ethylene Diamine at the Ribose-5`hydroxyl position.

In a second approach ribose-5`-hydroxyl analogues were synthesised by activating the hydroxyl group of the ribose at the lower nucleotide loop with 1,1`-carbonyldiimidazole (CDI) (Figure 5.9; Section 2.5). Addition of Ethylene Diamine functionalised the ribose-5`-hydroxyl group of the lower nucleotide loop to allow the conjugation of a fluorescent group (Oregon-Green or Bodipy-TR-X) (Figure 5.10). Two different cobalamin analogues (Oregon-Green and Bodipy-TR-X-B_{12}) were synthesised. In contrast to Texas-Red-B_{12}, the ribose analogues form a non-light sensitive covalent bond between vitamin-B_{12} and the fluorophore (Figure 5.9). After synthesis derivatives were analysed by LC-MS (Section 2.8.5).

The synthesis of the upper ligand analogue, Texas-Red-B_{12}, was a low yielding reaction but resulted in sufficient quantities for purification, characterisation and imaging. Texas-Red-B_{12} was identified on the basis of the UV-Vis absorption peaks for cobalamin (350 nm) and the fluorophore (587 nm) and a mass to charge ratio (*m/z*) corresponding to the assigned mass of Texas-Red-B_{12} (Figure 5.8 and Figure 5.9). The synthesised compound was not further characterisated, *e.g.* by NMR.

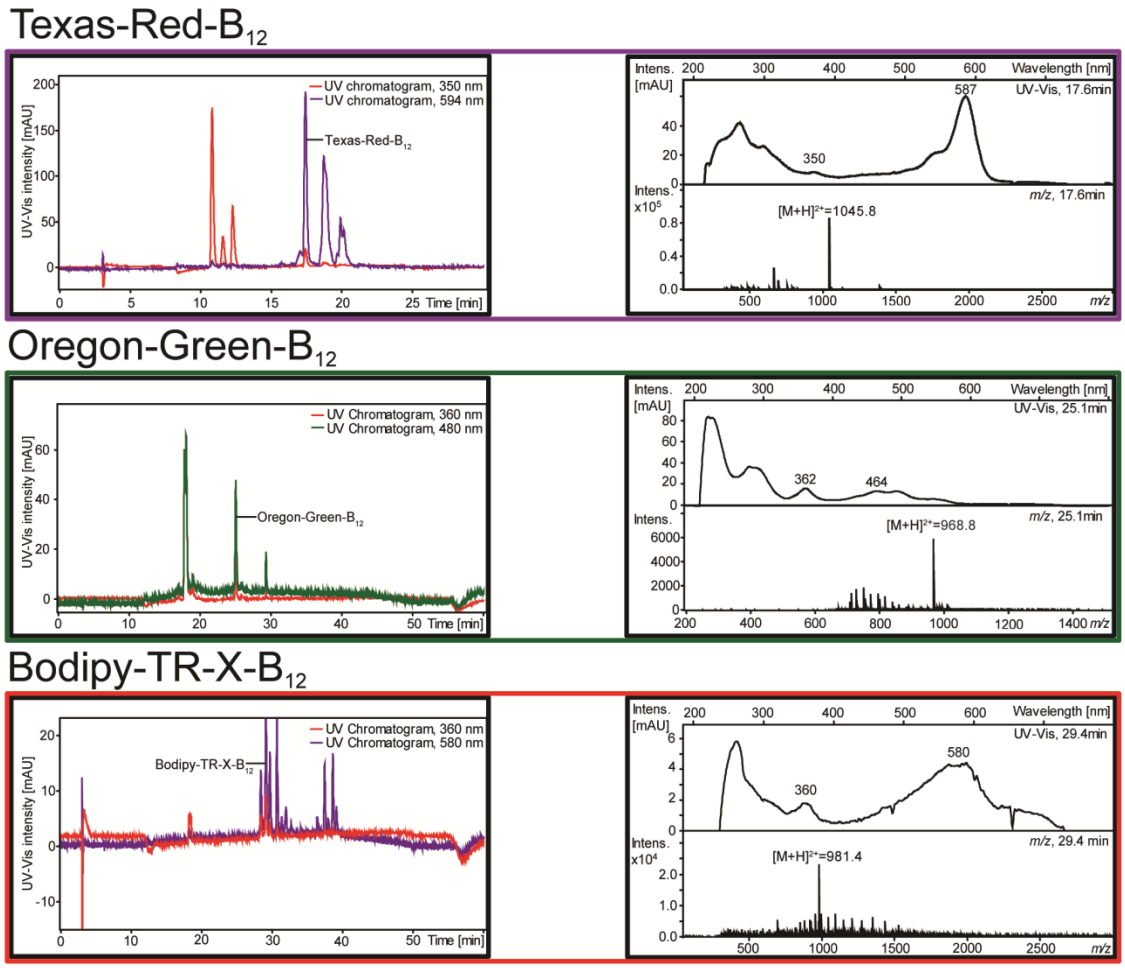

Figure 5.9. LC-MS analysis of the reaction mixtures for cobalamin analogue synthesis. **LEFT.** LC traces including UV chromatogram at 350 or 360 nm (red) for cobalamin specific absorption and absorption peak of the fluorophore group absorption (purple or green). The reaction product peak is labelled. Other peaks correspond to unreacted cobalamin, fluorophore or breakdown products. **RIGHT.** UV-Vis spectra and mass to charge (*m/z*) spectra of reaction products peaks.

As with the conjugation reaction to the upper ligand, so the lower loop analogue synthesis also resulted in low yielding reactions, which were sufficient for purification, characterisation and imaging applications (Section 2.5, Figure 5.9). Peaks not corresponding to reaction products of Oregon-Green-B_{12} and Bodipy-TR-X-B_{12} were not characterised further.

Oregon-Green-B_{12} was identified on the basis of its UV-Vis absorption peaks for both cobalamin (360 nm) and the fluorophore (464 nm), as well as its mass to charge ratio (*m/z*) that corresponds to the predicted mass of Oregon-Green-B_{12} (Figure 5.8 and 5.9).

Bodipy-TR-X-B_{12} was also identified on the basis of its UV-Vis absorption peaks for cobalamin (360 nm) and the fluorophore (580 nm) as well as its mass to charge ratio (*m/z*) corresponding to the predicted mass of Bodipy-TR-X-B_{12} (Figure 5.8 and 5.9).

5.9.2. Purification of fluorescent B_{12}-analogues

Reaction mixtures of Texas-Red-B_{12}, Oregon-Green-B_{12} and Bodipy-TR-X-B_{12} were purified from the reaction mixture by preparative LC (Section 2.5). The reaction product fraction was collected, dried *in vacuo* and analysed by LC-MS (Figure 5. 10, Section 2.8.5).

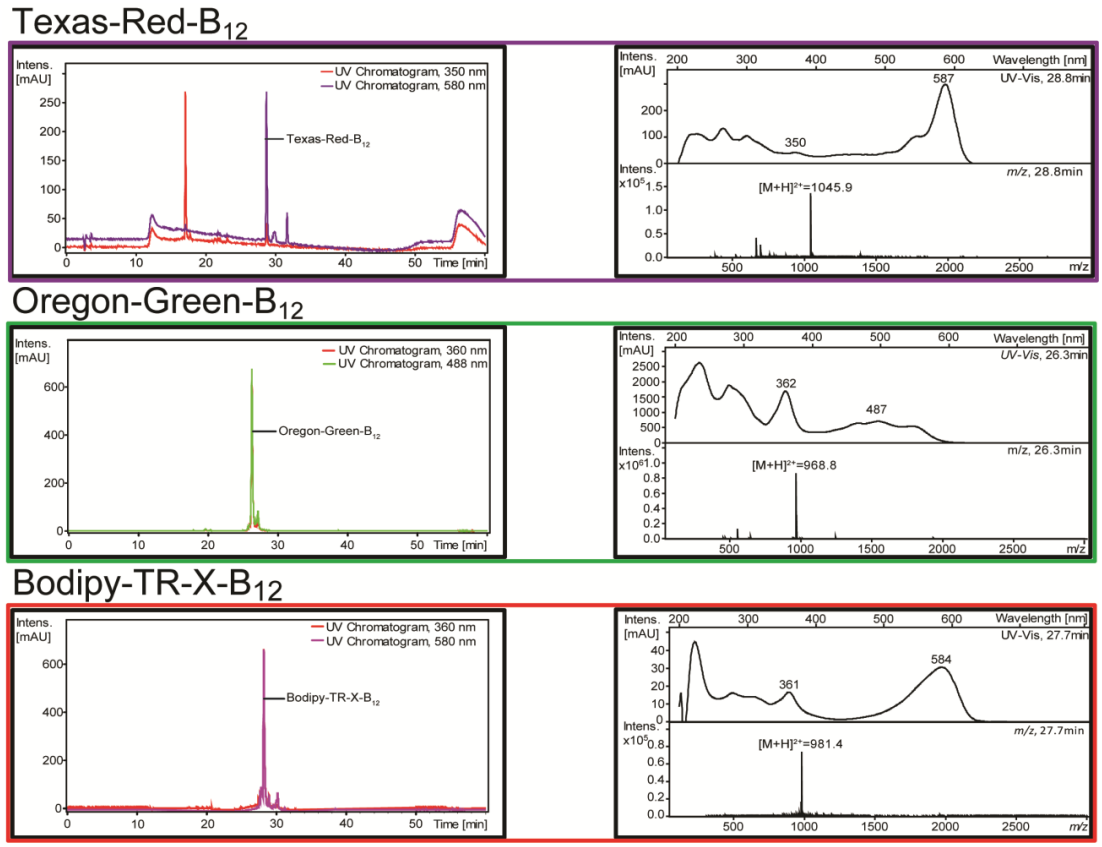

Figure 5.10. LC-MS analysis of purified cobalamin analogues **LEFT.** LC traces including UV chromatogram at 350 or 360 nm (red) for cobalamin specific absorption and absorption peak of the fluorophore group (purple or green) absorption. **RIGHT.** UV-Vis and mass to charge (*m/z*) spectra for each fluorescent cobalamin analogue are shown.

After LC purification, several peaks were still observed for the upper ligand analogue Texas-Red-B_{12}. These peaks corresponded to free OH-B_{12} and fluorophore. This demonstrated that Texas-Red-B_{12} was unstable.

The lower nucleotide loop analogues purified as single peaks by LC. UV-Vis and mass analysis were consistent with the assigned structure and had specific absorption maximum for vitamin-B_{12} at 360 nm and the fluorophore (Figure 5.11). This confirms the purity of both Oregon-Green-B_{12} and Bodipy-TR-X-B_{12} after purification. Next, the bioactivity of these cobalamin analogues was compared.

5.9.3. Fluorescent cobalamin analogues as active cofactors

HPLC-purified cobalamin analogues were tested in a bioassay to determine if they still retained cofactor activity for methionine synthase.

The bioassay is based on the fact that *metE* knock-out mutants of *S. typhimurium* (AR2680) cells are reliant upon their alternative cobalamin dependent methionine synthase, encoded by *metH*, for the biosynthesis of methionine and the presence of exogenous cobalamin (Section 2.6.10). Thus, the addition of a 10 µL drop of cobalamin to a bioassay plate stimulates growth, and size of the colony is dependent upon the amount of cobalamin within the droplet. Addition of known amounts of cobalamin can be used to generate a standard curve, which can then be used to estimate the concentration in unknown samples. Similarly, the bioassay can also be used to determine the cofactor activity of fluorescent cobalamin analogues of known concentrations. The activity of the fluorescent cobalamin analogues was compared to OH-B_{12}. Purified cobalamin analogues (2 pmol) and OH-B_{12} were spotted on the cobalamin bioassay plates and cells were grown overnight at 37°C. The colony size of OH-B_{12} was compared to those using fluorescent cobalamin analogues (Figure 5.11).

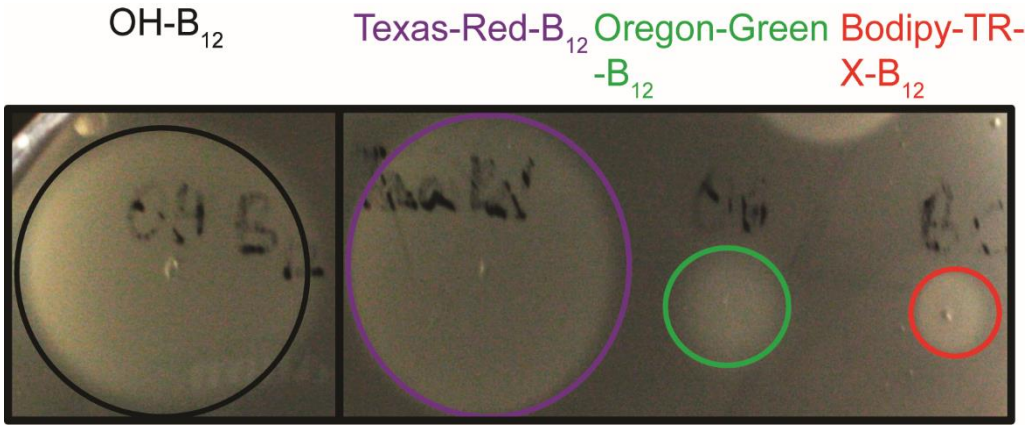

Figure 5.11. Activity of LC purified B_{12}-analogues on a cobalamin bioassay plate. 10 µL (2 pmol) of cobalamins were loaded in each case.

All three cobalamin analogues stimulated growth of the bioassay strain. This indicates that all three analogues are taken up into the bacterial cell. According to the observed growth on the bioassay plate, Texas-Red-B_{12} had the same activity as OH-B_{12}. This is perhaps not surprising because LC purified Texas-Red-B_{12} was already a mixture of OH-B_{12} and Texas-Red-B_{12}. Section 5.10.2 highlights the instability of the upper ligand, resulting in detection of OH-B_{12} and fluorescent cobalamin in LC-MS analysis.

In contrast, the lower loop nucleotide analogues Oregon-Green-B_{12} and Bodipy-TR-X-B_{12} produced a greatly reduced growth circle, indicating either hydrolysis of the lower loop analogues or a small level of conversion to a bioactive form. Neither of the cobalamin analogues was tested for limitations in uptake, assimilation and cofactor activity. The intracellular presence of either the complete analogues or derivates was not confirmed.

5.10. The spatial co-localisation of synthesised fluorescent cobalamin analogues with fluorescently labelled eBMCs

The fluorescent cobalamin analogues were used to investigate the association of cobalamin to the BMC *ex vivo*. This was attempted with labelled eBMC, where mCherry (m) or cyano fluorescent protein (CFP) were fused onto PduA. Isolated eBMCs (15 µL, CFPA-U and mA-U) were spotted onto glass cover slides and LC purified cobalamin fluorophores (Texas-Red-B_{12}, Oregon-Green-B_{12} and Bodipy-TR-X-B_{12}) were added (1 µL, Figure 5.12) and imaged using compatible fluorophore sets in wide field fluorescence microscopy (Section 2.9).

From this approach, wide field fluorescence microscopy was able to provide strong evidence for the spatial co-localisation of cobalamin analogues to the eBMC structures (Figure 5.12). Firstly, foci of the upper ligand derivative Texas-Red-B_{12} co-localised with fluorescently labelled eBMCs (CFPA-U, Panel A). Secondly, the lower loop analogue Oregon-Green-B_{12} co-localised with eBMC (mA-U, Panel B) foci, as did

the second lower loop derivative Bodipy-TR-X-B_{12} (CFPA-U, Panel C). However, due to resolution limitations, it was not determined if the cobalamin analogues are located to the lumen or just associated to the eBMC.

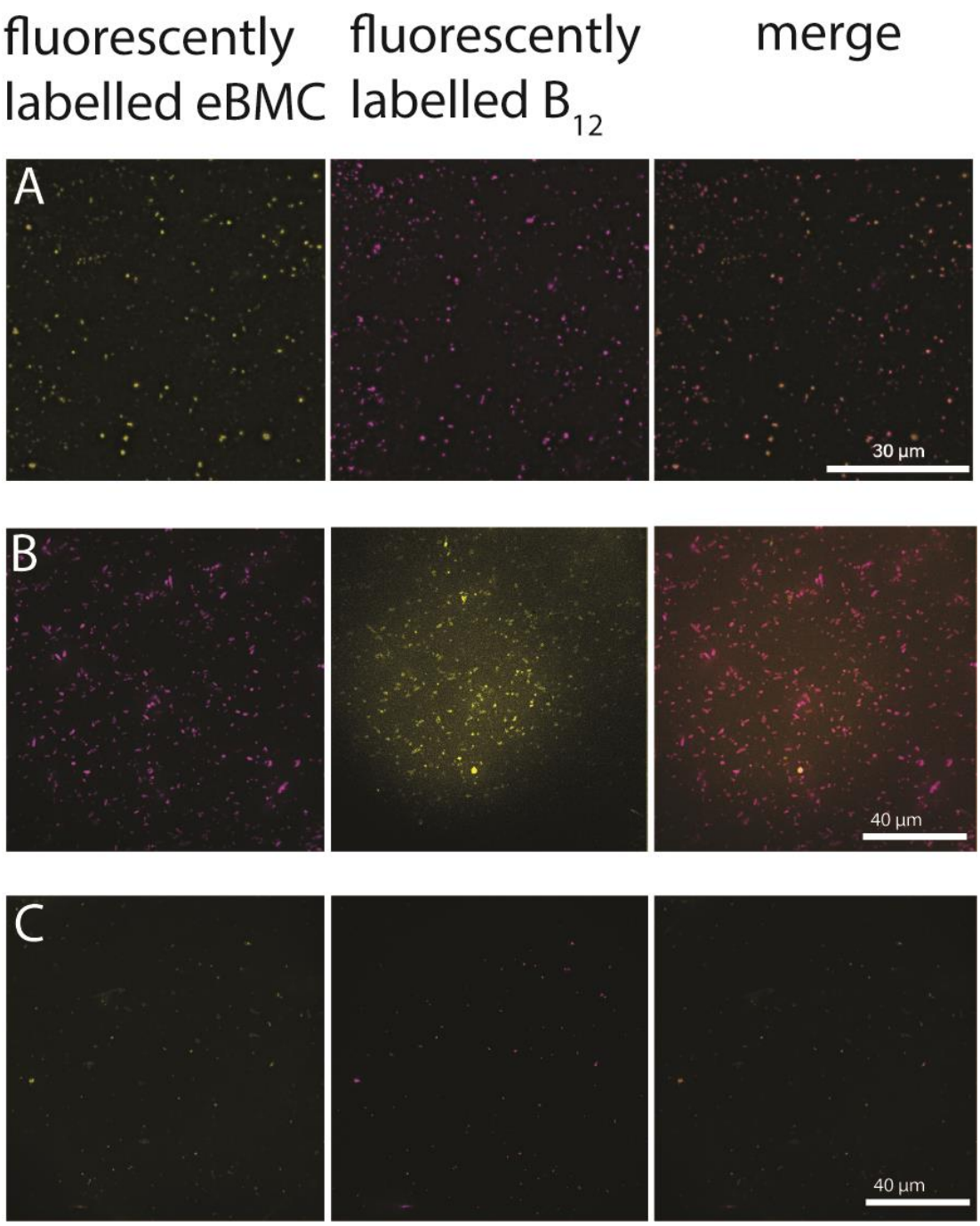

Figure 5.12. Partitioning of fluorescently labelled cobalamin with Pdu microcompartments (CFPA-U and mA-U). **Panel A** shows the effect of Texas-Red-B_{12} with CFPA-U. **Panel B** shows the effect of Oregon Green-B_{12} with mA-U. **Panel C** shows the effect of Bodipy-TR-X-B_{12} with CFPA-U.

5.11. Discussion

In this chapter the uptake and subcellular distribution of cobalamin with bacterial strains producing wild type BMCs, rBMCs and eBMCs was investigated.

Although cobalamin binding of individual BMC shell proteins was not studied systematically, cobalamin is clearly able to associate with intact BMCs, both *in vivo* and *in vitro*. The BMCs must therefore have a fairly high affinity for cobalamin. Thus, the presence of several different shell proteins or the conformation of the intact BMC, are suggested to generate an environment that favours cobalamin binding.

One of the most interesting findings in this chapter was the clear differential distribution of cobalamin within the cell. This is consistent with the increased sequestration of cobalamin within the BMC lumen. Furthermore, both wild type and rBMC were shown to be incapable of converting vitamin-B_{12} into Ado-B_{12} (Section 5.7). These observations were further attested by analysing the cobalamin pool of purified BMCs (wild type rBMC and eBMC). In addition to the qualitative analyses, a quantitative approach revealed a clear concentration dependent accumulation of vitamin-B_{12} with all tested BMCs (wild type, rBMC and eBMC). The lower accumulation in recombinant rBMC and eBMC in *E. coli* in comparison to wild type *C. freundii* can be explained by the increased number of BMC structures in the recombinant systems (rBMC and eBMC, Section 3.3). Although variation of BMC building blocks and structural differences between rBMC and eBMCs have been described earlier (Chapter 3 and Chapter 4), no differences in vitamin-B_{12} accumulation were observed for rBMCs and eBMCs (Table 5.2).

Moreover, three different fluorescent cobalamin analogues were found to partition with labelled Pdu microcompartments in wide field microscopy supporting previous biochemical observations.

E. coli and *C. freundii* can take up vitamin-B_{12} into the cell. Together, biochemical results point to the fact that vitamin-B_{12} partitions rapidly into the metabolosomes, prior to its conversion into Ado-B_{12}. The BMC is not able to decyanate vitamin-B_{12} but the BMC itself is likely to bind more cobalamin than the cytoplasm of the cell itself. This results in the accumulation of vitamin-B_{12} with the BMC becoming saturated at higher concentrations. This explains why the distribution of the cobalamin and the BMC appears to drop off as more cobalamin is added to the growth medium. More information is required as to how cobalamin binds to the BMC and whether it remains bound to the shell or is internalised into the lumen.

Chapter 6

Final discussion and conclusions

6.1. BMC formation, a modular, flexible and stable process

BMCs represent a modular and flexible system, which is evidenced by the ability to transfer BMC operons to allow the formation of organelles for carbon fixation and propanediol utilisation in *E. coli* (Parsons *et al.*, 2008; Bonacci *et al.*, 2012). Furthermore, BMCs can also self-assemble without any internal cargo as evidenced by the coordinated production of Pdu BMC shell proteins, which results in the formation of intracellular eBMCs (Parsons *et al.*, 2010).

The formation of such hollow but intact eBMC structures was confirmed and further characterised by the biophysical and proteomic approaches described in Chapter 3 and 4. A proteomic approach involving 2D-PAGE, MALDI TOF-TOF and densitometry was used to compare the shell composition of wild type BMCs, rBMCs and eBMCs (A-U, mA-U, A-T). This revealed subtle but notable variation in shell protein composition between the complete BMCs (wild type and rBMC), where PduB` is the major shell protein, and the eBMCs, in which a higher level of PduA is incorporated.

The effect of different shell protein compositions on the shape and physical properties of the BMC was further investigated by TEM and AFM, which revealed that this variation in shell protein composition does not disrupt BMC assembly. Single particle analysis was performed to quantify the irregular and heterogeneous nature of the various BMCs in terms of their size. No significant differences between AFM and TEM data sets were observed for the complete Pdu BMCs (wild type and rBMC) and the eBMC variants (A-U, mA-U and A-T). Thus, AFM allows for the direct measurement of BMC particles. With AFM, the wild type and rBMCs were found to have a similar size (122-133 nm in average diameter) and to form a defined structure independent of the host strain. As with Pdu BMCs, no significant differences were observed between the different eBMC variants, which varied in size between 56 to 77 nm in diameter. Therefore, there is a clear size difference between the complete Pdu BMCs (wild type and rBMCs) and the smaller eBMC variants (A-U, mA-U and A-T).

The direct measurement of biological samples by AFM allows for the simultaneous acquisition of topological features and the determination of nano-mechanical properties. Differences in reduced DMT modulus, describing the rigidity and elasticity of a biological sample and deformation were estimated for Pdu microcompartments. The smaller eBMC variants were found to form more rigid structures than their larger Pdu counterparts, which appeared to be more elastic (wild type and rBMC). No major differences were observed between wild type and rBMC structures. The different nano-mechanical properties of the Pdu BMCs (wild type and rBMCs) in comparison to the eBMC variants (A-U, mA-U and A-T) substantiate the idea that Pdu BMCs and eBMCs form distinct structures. Furthermore, the eBMCs lack electron density in their lumens, in contrast to the more densely packed Pdu microcompartments.

These observations provide new fundamental insights into the structural variation of BMCs and allow a number of conclusions to be drawn. Firstly, the host organism has little effect on the complete Pdu BMC in terms of the shell composition, size, nano-mechanical properties and packing. Secondly, reducing the set of building blocks of eBMCs from A-T to A-U does not alter the shell composition, size, nano-mechanical parameters or packing of the structure. In addition, the fusion of the fluorescent protein mCherry onto PduA has no consequences regarding the shell composition, size, nano-mechanical properties and packing of the structure. BMC shell assembly in Pdu BMCs (wild type and rBMC) and eBMC variants (A-U, mA-U and A-T) appears to have a degree of flexibility, allowing the formation of stable supramolecular assemblies within the cell. Internal cargo is not required for BMC assembly. The modularity of BMC formation is also seen in carboxysomes. For instance, the pore of the β-carboxysome shell protein CcmK2 was altered to mimic the pore environment of the BMC shell proteins CsoS1 or CcmK4 (Cai *et al.*, 2014), a modification, which did not disrupt the β-carboxysome assembly in *S. elongatus* PCC 7942. Similarly, swapping CcmK2 with the α-carboxysomal BMC shell protein CsoS1 did not disrupt carboxysome formation.

6.2. Towards an overall structure of Pdu BMCs

The imaging of the BMCs by AFM and TEM highlighted a general variation in shape and size, all of which complicates the determination of an overall structure for the Pdu microcompartments.

This dissertation describes the development of extraction and isolation protocols for Pdu microcompartments, methods that are a prerequisite for follow up structural analysis by AFM or EM. Furthermore, sample preparations for in-solution AFM, and cryo-EM are reported, which can both be employed to provide topographical information on the Pdu microcompartments in the longer term (Foster, 2012; Bai *et al.*, 2015). However, to determine the overall structure of Pdu microcompartments by AFM, in-solution technical challenges such as distortion of the structure during deposition and sample drift need to be addressed to take this research forward.

Alternatively, the overall structural properties of Pdu microcompartments could be examined by cryo-EM, as shown for the eBMC A-U in Section 4.7.2. Cryo-electron tomography provides a series of 2D images, which can be reconstructed into 3D structural models (Bai *et al.*, 2015). Modelled structures of Pdu microcompartment structures would then be clustered and characterised. The development of direct electron detector for cryo-EM represents a true alternative to the more standard structural biology tools such as NMR or X-ray crystallography. In contrast to other structural biology tools (crystallography and NMR), cryo-EM requires less sample as little as 0.1 mg may be enough and sample purity is less crucial for the acquisition of cryo-EM data. These developments can be seen in the increasing number of reports of structural cryo-EM data with resolutions higher than 5 Å between 2013 and 2015 (Bai *et al.*, 2015). Therefore, cryo-EM and AFM represent powerful tools to solve the overall structure of irregular Pdu microcompartments. Such a structural characterisation will help us to understand the functional role of the organelle in

more detail, by providing essential information on the orientation and positioning of shell proteins within the overall structure.

6.3. An additional functional role of the Pdu BMC

The central pores in the Pdu shell proteins are thought to be involved in the transport of a wide variety of molecules such as substrates, metabolites and cofactors (Frank *et al.*, 2013; Chowdhury *et al.*, 2014). The shell of the BMC forms a semi-permeable protein membrane, whereby the central pores offer selective movement into or out of the BMC (Frank *et al.*, 2013; Deery *et al.*, 2014; Chessher *et al.*, 2015).

In this study, an *in vitro* approach revealed that when BMCs (wild type, rBMC and eBMC (A-U)) were incubated with different cobalamins (Ado-B_{12}, Me-B_{12}, OH-B_{12} and vitamin-B_{12}), that the cobalamins localised to the organelles during purification. *In vivo*, a similar observation was made. When bacterial strains were grown with exogenous cobalamin, cobalamin was found to accumulate with the BMC. This was derived from the development of methods to quantitatively estimate the distribution of cobalamin within the cell. However, it was also shown that the accumulation of B_{12} in the BMC followed a saturation dependent uptake process. This uptake was found not only with the complete Pdu BMC but also with the eBMC (A-U). Therefore, the association of cobalamin with the BMC is independent of any incorporated Ado-B_{12} dependent enzymes (PduCDE) and reactivation factors (PduGH, PduO and PduS). To visualise the association of cobalamin with the BMC, various fluorescent B_{12}-analogues were generated, purified and characterised. Incubation of the fluorescent B_{12} molecules with purified eBMCs resulted in their co-localisation as determined by fluorescent microscopy. Surprisingly though, the BMCs do not house the ability to activate vitamin-B_{12}.

In terms of metabolic engineering, the ability to selectively take up cofactors such as cobalamin is a desired feature for the sequestration of biological processes and

supports an additional functional role of Pdu BMCs to optimise the availability of cobalamin.

6.4. BMCs in the context of metabolic engineering

We are in the era of synthetic biology, whereby our ability to perform large scale sequencing, coupled with the development of relatively cheap DNA synthesis, means that we can protein engineer and redesign major biological processes for useful purposes.

Major achievements in the field are exemplified by the recombinant biosynthesis of complex metabolic products such as cobalamin in *E. coli*, artemisinic acid in *S. cerevisiae* and opium in *Saccharomyces cerevisiae* (Ro *et al.*, 2006; Deery *et al.*, 2012; Fossati *et al.*, 2015).

However, metabolic engineering remains challenging (Chessher *et al.*, 2015). Transplanted metabolic pathways have to compete with other cellular processes for substrates and cofactors. Furthermore, intermediates can be toxic or diverted by competing processes. This can reduce the efficiency of the metabolic pathway, lead to the accumulation of intermediates, or cause toxicity issues. Consequently, bioengineers aim to reduce such detrimental effects by increasing the local concentration of pathway enzymes or by sequestering metabolic pathways. In this respect, several strategies have been reported in recent years including the use of cellular scaffolds to link consecutive metabolic enzymes via DNA, RNA or other proteins in order to increase the local concentration of consecutive enzymes (Frank *et al.*, 2013; Giessen; Silver, 2015; Siu *et al.*, 2015). The scaffolding of metabolic enzymes can increase the throughput of a metabolic pathway without sequestering the pathway from the cytoplasm (Chessher *et al.*, 2015; Siu *et al.*, 2015).

Alternatively, pathways can be sequestered to viral capsids or to BMCs in order to segregate metabolic pathways from the cytoplasm (Grasso; Santi, 2010). From a biological perspective, BMC based systems appear to be superior to other systems. For instance, scaffolding mechanisms are not spatially segregated from cellular processes and viral capsids evolved to maintain mainly genomic information, and therefore, are not designed for metabolism. In contrast, bacterial organelles evolved to optimise and sequester metabolic pathways. This suggests that BMC based systems offer an ideal platform for metabolic engineering, as shown in Figure 6.1.

To apply BMC based systems, it is crucial to understand the structure and function of the system. Thus, fundamental insights into the BMC shell composition, the biophysical properties of the compartment, as well as the knowledge of cofactor uptake and accumulation mechanisms will all assist the redesign of BMCs for new biotechnological applications.

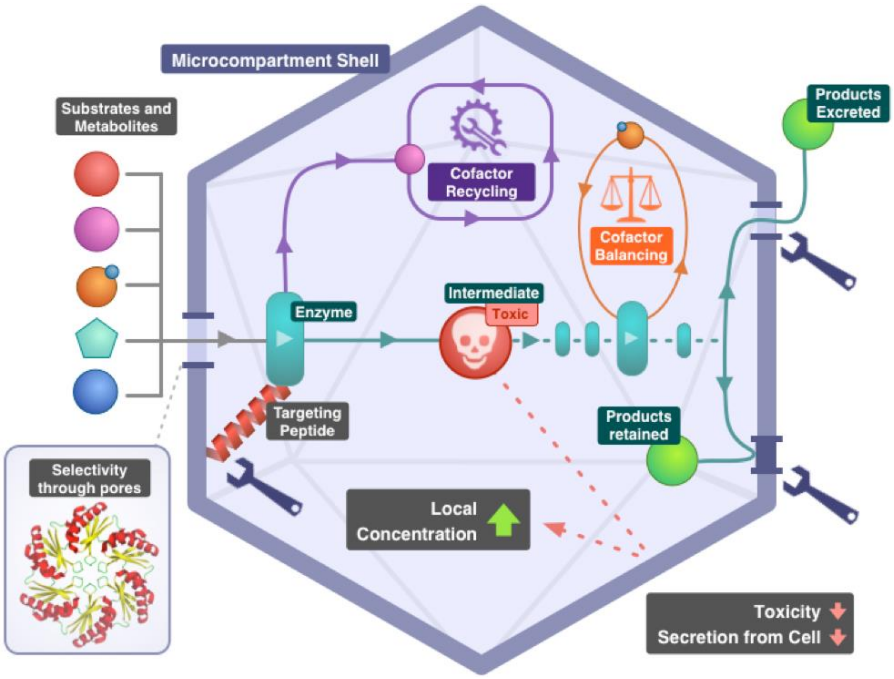

Figure 6.1. Advantages of BMC based systems in the context of synthetic biology (Deery *et al.*, 2014).

6.5. Conclusions

This study on wild type, rBMC and eBMC system provides fundamental insights into the BMC shell composition and its associated biophysical characteristics. The ability of BMCs to increase the local concentration of cobalamin has been uncovered. This was achieved by improving methods for BMC isolation, generating samples that show the intact nature of the isolated BMCs and resulting in the detailed proteomic and biophysical comparison of wild type and rBMCs to eBMC variants. Interestingly, Pdu BMCs (wild type and recombinant) showed no obvious proteomic differences, which is consistent with the formation of similar sized structures that have near identical nano-mechanical properties. It was shown that empty Pdu BMCs (eBMCs) are different from wild type and rBMCs in shell protein composition (shift to PduA), smaller size and more rigid assemblies (see Figure 6.2). Furthermore, eBMCs were shown to be hollow in contrast to their propanediol utilising counterparts. The research described in this thesis demonstrates that Pdu BMCs are able to accumulate B_{12} both *in vitro* and *in vivo*. The synthesis of fluorescently labelled B_{12}-analogues has allowed the development of a novel visualisation of the co-localisation of cobalamin to fluorescently labelled eBMC shells *ex vivo*.

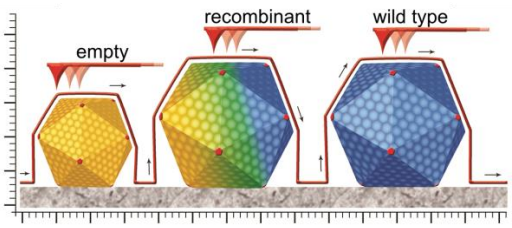

Figure 6.2. Graphical table of content, summarising the structural analysis of Pdu microcompartments

Chapter 7

Appendix

7.1. Tandem mass spectrometry

Table 7.1. In-detail analysis of single shell protein spots from 2D-PAGE. NCBI accession number, number of peptide matches, probability based Mowse score and sequence coverage [%] are given for each eBMC construct (A-U, mA-U and A-T) and BMC (rBMC and wild-type).

A-U			**Mascot search result**	
Identity assigned	**NCBI accession no**	**No. of peptides matched**	**Probability based Mowse score**	**% sequence coverage**
PduA	gi446152585	4(0)	141	54
PduB	gi489930809	4(1)	211	22
PduB`	gi507082779	5(1)	131	17
PduJ	gi668711810	3(2)	163	53
PduK	gi489930823	1(0)	46	14
PduN	gi507086135	1(1)	81	25
PduU	gi489940949	3(0)	94	32
mA-U			**Mascot search result**	
PduA	gi446152585	2(1)	101	25
mCherryPduA	gi55420613/ gi446152585	4(2)/1(1)	227/65	23/13
PduB	gi489930809	6(5)	582	45
PduB`	gi489930809	4(4)	395	20
PduJ	gi446980496	3 (2)	259	53
PduK	gi489930823	2(1)	112	20
PduN	gi507086135	1(1)	112	25
PduU	gi489940949	2(2)	265	25
A-T			**Mascot search result**	

PduA	gi446152585	3(0)	99	41
PduB	gi489930809	5(2)	274	32
PduB`	gi489930809	5(2)	256	32
PduJ	gi446980496	4(1)	216	78
PduK	gi489930823	1(1)	72	14
PduN	gi507086135	2(0)	75	36
PduU	gi489930848	2(2)	160	27
PduT	gi489940949	2(1)	95	18

rBMC construct: A-X			**Mascot search result**	
Identity assigned	**NCBI accession no.**	**No. of peptides matched**	**Probability based Mowse score**	**% sequence coverage**
PduA	gi446152585	3(1)	141	49
PduB	gi489930809	6(4)	427	40
PduB`	gi489930809	5(4)	424	28
PduJ	gi446980496	4(2)	267	59
PduK	gi489936823	1(1)	76	14
PduN	gi507086135	1(1)	88	25
PduT	gi489940949	4(0)	90	18
PduU	gi489940949	2(1)	133	27
wild type			**Mascot search result**	
PduA	gi446152585	4(2)	211	46
PduB	gi489930809	4(2)	236	24
PduB`	gi489930809	4(2)	240	20
PduJ	gi446980496	3(2)	133	35
PduK	gi489930823	1(1)	73	14

PduN	gi507086135	1(1)	114	25
PduT	gi489940949	1(1)	65	7
PduU	gi489940949	2(0)	102	16

7.2. Ratios B_{12} calculation

Table 7.2. Accumulation of vitamin-B_{12} in BMCs (eBMC, rBMC and wild type).

Accumulation of vitamin-B_{12}							
	vitamin-B_{12} [µM] per mg*mL^{-1} protein				**Ratios of [vitamin-B_{12}] in BMC to lysate**		
	Vitamin-B_{12} in media	**0.1 µM**	**1.0 µM**	**10 µM**	**0.1 µM**	**1.0 µM**	**10 0 µM**
eBMC (A-U)	**1. Lysate**	0.091	0.790	0.218	51 ± 0.1	14 ± 1.6	4 ± 0.6
	1. BMC	4.640	9.701	0.848			
	2. Lysate	0.047	0.102	0.11			
	2. BMC	2.385	1.572	0.56			
rBMC (A-X)	**1. Lysate**	0.002	0.005	0.063	57 ± 4.3	27 ± 3.1	10 ± 5.9
	1. BMC	0.123	0.121	0.234			
	1. Lysate	0.002	0.005	0.010			
	2. BMC	0.106	0.152	0.155			
wild type	**1. Lysate**	0.003	0.008	0.002	186 ± 47.9	77 ± 1.3	40 ± 2.4
	1. BMC	0.413	0.628	0.074			
	2. Lysate	0.002	0.002	0.004			
	2. BMC	0.467	0.152	0.167			

7.3. References

Abdul-Rahman, F., Petit, E., and Blanchard, J.L. (2013) The distribution of polyhedral bacterial microcompartments suggests frequent horizontal transfer and operon reassembly. *J Phylogenetics Evol Biol* **1:** e1000118.

Adrian, M., Dubochet, J., Lepault, J., and McDowall, A.W. (1984) Cryo-electron microscopy of viruses. *Nature* **308:** 32-36.

Alanen, H.I., Walker, K.L., Suberbie, M.L.V., Matos, C.F., Bönisch, S., Freedman, R.B*., et al.* (2014) Efficient export of human growth hormone, interferon α2b and antibody fragments to the periplasm by the *Escherichia coli* Tat pathway in the absence of prior disulfide bond formation. *Biochim Biophys Acta* **3:** 756-763.

Alberts, B. (1998) The cell as a collection of protein machines: preparing the next generation of molecular biologists. *Cell* **92:** 291-294.

Axen, S.D., Erbilgin, O., and Kerfeld, C.A. (2014) A Taxonomy of bacterial microcompartment loci constructed by a novel scoring method. *PLoS Comput Biol* **10:** e1003898.

Bai, X., McMullan, G., and Scheres, S.H. (2015) How cryo-EM is revolutionizing structural biology. *Trends Biochem Sci* **40:** 49-57.

Baker, S.H., Lorbach, S.C., Rodriguez-Buey, M., Williams, D.S., Aldrich, H.C., and Shively, J.M. (1999) The correlation of the gene csoS2 of the carboxysome operon with two polypeptides of the carboxysome in *Thiobacillus neapolitanus. Arch Microbiol* **172:** 233-239.

Baker, S.H., Jin, S., Aldrich, H.C., Howard, G.T., and Shively, J.M. (1998) Insertion mutation of the form I *cbbL* gene encoding ribulose bisphosphate carboxylase/oxygenase (RuBisCO) in *Thiobacillus neapolitanus* results in expression of form II RuBisCO, loss of carboxysomes, and an increased CO_2 requirement for growth. *J Bacteriol* **180:** 4133-4139.

Banerjee, R., and Ragsdale, S.W. (2003) The Many Faces of Vitamin B_{12}: Catalysis by Cobalamin-Dependent Enzymes 1. *Annu Rev Biochem* **72:** 209-247.

Beudeker, R., Cannon, G., Kuenen, J., and Shively, J. (1980) Relations between D-ribulose-1, 5-bisphosphate carboxylase, carboxysomes and CO_2 fixing capacity in the obligate chemolithotroph *Thiobacillus neapolitanus* grown under different limitations in the chemostat. *Arch Microbiol* **124:** 185-189.

Bobik, T.A., Ailion, M., and Roth, J.R. (1992) A single regulatory gene integrates control of vitamin B_{12} synthesis and propanediol degradation. *J Bacteriol* **174:** 2253-2266.

Bobik, T.A., Havemann, G.D., Busch, R.J., Williams, D.S., and Aldrich, H.C. (1999) The propanediol utilization (pdu) operon of *Salmonella enterica* serovar Typhimurium LT2 includes genes necessary for formation of polyhedral organelles involved in coenzyme B(12)-dependent 1, 2-propanediol degradation. *J Bacteriol* **181:** 5967-5975.

Bobik, T.A., Xu, Y., Jeter, R.M., Otto, K.E., and Roth, J.R. (1997) Propanediol utilization genes (pdu) of *Salmonella typhimurium*: three genes for the propanediol dehydratase. *J Bacteriol* **179:** 6633-6639.

Bock, E., Duvel, D., and Peters, K.R. (1974) Characterization of a phage-like particle from cells of *Nitrobacter*. I. Host-particle correlation and particle isolation (author's transl). *Arch Microbiol* **97:** 115-127.

Bonacci, W., Teng, P.K., Afonso, B., Niederholtmeyer, H., Grob, P., Silver, P.A., and Savage, D.F. (2012) Modularity of a carbon-fixing protein organelle. *Proc Natl Acad Sci U S A* **109:** 478-483.

Bradford, M.M. (1976) A rapid and sensitive method for the quantitation of microgram quantities of protein utilizing the principle of protein-dye binding. *Anal Biochem* **72:** 248-254.

Cai, F., Menon, B.B., Cannon, G.C., Curry, K.J., Shively, J.M., and Heinhorst, S. (2009) The pentameric vertex proteins are necessary for the icosahedral carboxysome shell to function as a CO_2 leakage barrier. *PloS One* **4:** e7521.

Cai, F., Sutter, M., Bernstein, S.L., Kinney, J.N., and Kerfeld, C.A. (2014) Engineering bacterial microcompartment shells: Chimeric shell proteins and chimeric carboxysome shells. *ACS Synth Biol* **4:** 444-453.

Cameron, J.C., Wilson, S.C., Bernstein, S.L., and Kerfeld, C.A. (2013) Biogenesis of a bacterial organelle: the carboxysome assembly pathway. *Cell* **155:** 1131-1140.

Cannon, G., and Shively, J. (1983) Characterization of a homogenous preparation of carboxysomes from *Thiobacillus neapolitanus. Arch Microbiol* **134:** 52-59.

Cannon, G.C., Baker, S.H., Soyer, F., Johnson, D.R., Bradburne, C.E., Mehlman, J.L., *et al.* (2003) Organization of carboxysome genes in the Thiobacilli. *Curr Microbiol* **46:** 0115-0119.

Cannon, G.C., English, R.S., and Shively, J.M. (1991) In situ assay of ribulose-1,5-bisphosphate carboxylase/oxygenase in *Thiobacillus neapolitanus. J Bacteriol* **173:** 1565-1568.

Caspar, D.L., and Klug, A. (1962) Physical principles in the construction of regular viruses. *Cold Spring Harb Symp Quant Biol* **27:** 1-24.

Chen, A.H., Robinson-Mosher, A., Savage, D.F., Silver, P.A., and Polka, J.K. (2013) The bacterial carbon-fixing organelle is formed by shell envelopment of preassembled cargo. *PloS One* **8:** e76127.

Chen, P., Andersson, D.I., and Roth, J.R. (1994) The control region of the *pdu/cob* regulon in *Salmonella typhimurium. J Bacteriol* **176:** 5474-5482.

Cheng, S., and Bobik, T.A. (2010) Characterization of the PduS cobalamin reductase of Salmonella enterica and its role in the Pdu microcompartment. *J Bacteriol* **192:** 5071-5080.

Cheng, S., Fan, C., Sinha, S., and Bobik, T.A. (2012) The PduQ enzyme is an alcohol dehydrogenase used to recycle NAD+ internally within the Pdu microcompartment of *Salmonella enterica. PLoS One* **7:** e47144.

Cheng, S., Liu, Y., Crowley, C.S., Yeates, T.O., and Bobik, T.A. (2008) Bacterial microcompartments: their properties and paradoxes. *Bioessays* **30:** 1084-1095.

Cheng, S., Sinha, S., Fan, C., Liu, Y., and Bobik, T.A. (2011) Genetic analysis of the protein shell of the microcompartments involved in coenzyme B_{12}-dependent 1,2-propanediol degradation by *Salmonella. J Bacteriol* **193:** 1385-1392.

Chessher, A., Breitling, R., and Takano, E. (2015) Bacterial microcompartments: biomaterials for synthetic biology-based compartmentalization strategies. *ACS Biomater Sci Eng* **1:** 345-351.

Choudhary, S., Quin, M.B., Sanders, M.A., Johnson, E.T., and Schmidt-Dannert, C. (2012) Engineered protein nano-compartments for targeted enzyme localization. *PLoS One* **7:** e33342.

Chowdhury, C., Chun, S., Pang, A., Sawaya, M.R., Sinha, S., Yeates, T.O., and Bobik, T.A. (2015) Selective molecular transport through the protein shell of a bacterial microcompartment organelle. *Proc Natl Acad Sci U S A* **112:** 2990-2995.

Chowdhury, C., Sinha, S., Chun, S., Yeates, T.O., and Bobik, T.A. (2014) Diverse bacterial microcompartment organelles. *Microbiol Mol Biol Rev* **78:** 438-468.

Conner, C.P., Heithoff, D.M., Julio, S.M., Sinsheimer, R.L., and Mahan, M.J. (1998) Differential patterns of acquired virulence genes distinguish *Salmonella* strains. *Proc Natl Acad Sci U S A* **95:** 4641-4645.

Corchero, J.L., and Cedano, J. (2011) Self-assembling, protein-based intracellular bacterial organelles: emerging vehicles for encapsulating, targeting and delivering therapeutical cargoes. *Microb Cell Fact* **10:** 92.

Crowley, C.S., Cascio, D., Sawaya, M.R., Kopstein, J.S., Bobik, T.A., and Yeates, T.O. (2010) Structural insight into the mechanisms of transport across the *Salmonella enterica* Pdu microcompartment shell. *J Biol Chem* **285:** 37838-37846.

Crowley, C.S., Sawaya, M.R., Bobik, T.A., and Yeates, T.O. (2008) Structure of the PduU shell protein from the Pdu microcompartment of *Salmonella. Structure* **16:** 1324-1332.

Deery, E., Frank, S., Lawrence, A., Moore, S., Schroeder, S., and Warren, M.J. (2014) Synthetic Biology in Metabolic Engineering: From Complex Biochemical Pathways to Compartmentalized Metabolic Processes–a Vitamin Connection. In *Reviews in Cell Biology and Molecular Medicine,* 1-47.

Deery, E., Schroeder, S., Lawrence, A.D., Taylor, S.L., Seyedarabi, A., Waterman, J.*, et al.* (2012) An enzyme-trap approach allows isolation of intermediates in cobalamin biosynthesis. *Nat Chem Biol* **8:** 933-940.

Drews, G., and Niklowitz, W. (1956) Beiträge zur Cytologie der Blaualgen. *Arch Microbiol* **24:** 147-162.

English, R.S., Lorbach, S.C., Qin, X., and Shively, J.M. (1994) Isolation and characterization of a carboxysome shell gene from *Thiobacillus neapolitanus. Mol Microbiol* **12:** 647-654.

English, R.S., Jin, S., and Shively, J.M. (1995) Use of Electroporation To Generate a *Thiobacillus neapolitanus* Carboxysome Mutant. *Appl Environ Microbiol* **61:** 3256-3260.

Escalante-Semerena, J.C., Suh, S.J., and Roth, J.R. (1990) *cobA* function is required for both *de novo* cobalamin biosynthesis and assimilation of exogenous corrinoids in *Salmonella typhimurium. J Bacteriol* **172:** 273-280.

Fan, C., and Bobik, T.A. (2008) The PduX enzyme of *Salmonella enterica* is an L-threonine kinase used for coenzyme B_{12} synthesis. *J Biol Chem* **283:** 11322-11329.

Fan, C., and Bobik, T.A. (2011) The N-terminal region of the medium subunit (PduD) packages adenosylcobalamin-dependent diol dehydratase (PduCDE) into the Pdu microcompartment. *J Bacteriol* **193:** 5623-5628.

Fan, C., Cheng, S., Liu, Y., Escobar, C.M., Crowley, C.S., Jefferson, R.E., *et al.* (2010) Short N-terminal sequences package proteins into bacterial microcompartments. *Proc Natl Acad Sci U S A* **107:** 7509-7514.

Fan, C., Cheng, S., Sinha, S., and Bobik, T.A. (2012) Interactions between the termini of lumen enzymes and shell proteins mediate enzyme encapsulation into bacterial microcompartments. *Proc Natl Acad Sci U S A* **109:** 14995-15000.

Fletcher, J.M., Harniman, R.L., Barnes, F.R., Boyle, A.L., Collins, A., Mantell, J., *et al.* (2013) Self-assembling cages from coiled-coil peptide modules. *Science* **340:** 595-599.

Fonseca, M.V., and Escalante-Semerena, J.C. (2000) Reduction of Cob(III)alamin to Cob(II)alamin in *Salmonella enterica* serovar typhimurium LT2. *J Bacteriol* **182:** 4304-4309.

Fonseca, M.V., and Escalante-Semerena, J.C. (2001) An *in vitro* reducing system for the enzymic conversion of cobalamin to adenosylcobalamin. *J Biol Chem* **276:** 32101-32108.

Fossati, E., Narcross, L., Ekins, A., Falgueyret, J., and Martin, V.J. (2015) Synthesis of morphinan alkaloids in *Saccharomyces cerevisiae. PLoS One* **4:** e0124459.

Foster, B. (2012) New atomic force microscopy (AFM) approaches life sciences gently, quantitatively, and correlatively. *Am Lab* **44:** 24-28.

Frank, S., Lawrence, A.D., Prentice, M.B., and Warren, M.J. (2013) Bacterial microcompartments moving into a synthetic biological world. *J Biotechnol* **163:** 273-279.

Gallo, S., Oberhuber, M., Sigel, R.K., and Kräutler, B. (2008) The corrin moiety of coenzyme B_{12} is the determinant for switching the *btuB* riboswitch of *E. coli. ChemBioChem* **9:** 1408-1414.

Giessen, T.W., and Silver, P.A. (2015) Encapsulation as a strategy for the design of biological compartmentalization. *J Mol Biol* **15:** 00520-00523.

Gonzales, A.D., Light, Y.K., Zhang, Z., Iqbal, T., Lane, T.W., and Martino, A. (2005) Proteomic analysis of the CO_2-concentrating mechanism in the open-ocean cyanobacterium *Synechococcus WH8102. Can J Bot* **83:** 735-745.

Gradišar, H., Božič, S., Doles, T., Vengust, D., Hafner-Bratkovič, I., Mertelj, A*., et al.* (2013) Design of a single-chain polypeptide tetrahedron assembled from coiled-coil segments*. Nat Chem Biol* **9:** 362-366.

Grasso, S., and Santi, L. (2010) Viral nanoparticles as macromolecular devices for new therapeutic and pharmaceutical approaches*. Int J Physiol Pathophysiol Pharmacol* **2:** 161-178.

Green, M.R., and Sambrook, J. (2012, 4th Edition) *Molecular cloning: a laboratory manual*: Cold Spring Harbor Laboratory Press New York.

Havemann, G.D., and Bobik, T.A. (2003) Protein content of polyhedral organelles involved in coenzyme B_{12}-dependent degradation of 1,2-propanediol in *Salmonella enterica* serovar Typhimurium LT2*. J Bacteriol* **185:** 5086-5095.

Havemann, G.D., Sampson, E.M., and Bobik, T.A. (2002) PduA is a shell protein of polyhedral organelles involved in coenzyme B(12)-dependent degradation of 1,2-propanediol in *Salmonella enterica* serovar typhimurium LT2*. J Bacteriol* **184:** 1253-1261.

Heinhorst, S., Cannon, G.C., and Shively, J.M. (2006) Carboxysomes and carboxysome-like inclusions. In *Complex intracellular structures in prokaryotes* Carboxysomes and carboxysome-like inclusions: Springer, pp. 141-165.

Hoffmann, F., and Rinas, U. (2004) Stress induced by recombinant protein production in Escherichia coli. In *Physiological Stress Responses in Bioprocesses* Stress induced by recombinant protein production in *Escherichia coli*: Springer, pp. 73-92.

Horswill, A.R., and Escalante-Semerena, J.C. (1997) Propionate catabolism in *Salmonella typhimurium* LT2: two divergently transcribed units comprise the prp locus at 8.5 centisomes, *prpR* encodes a member of the sigma-54 family of activators, and the *prpBCDE* genes constitute an operon*. J Bacteriol* **179:** 928-940.

Horswill, A.R., and Escalante-Semerena, J.C. (1999) *Salmonella typhimurium* LT2 catabolizes propionate via the 2-methylcitric acid cycle*. J Bacteriol* **181:** 5615-5623.

Huseby, D.L., and Roth, J.R. (2013) Evidence that a Metabolic Microcompartment Contains and Recycles Private Cofactor Pools*. J Bacteriol* **195:** 2864-2879.

Iancu, C.V., Ding, H.J., Morris, D.M., Dias, D.P., Gonzales, A.D., Martino, A., and Jensen, G.J. (2007) The Structure of Isolated *Synechococcus* Strain WH8102 Carboxysomes as Revealed by Electron Cryotomography*. J Mol Biol* **372:** 764-773.

Jakobson, C.M., Kim, E.Y., Slininger, M.F., Chien, A., and Tullman-Ercek, D. (2015) Localization of Proteins to the 1,2-Propanediol Utilization Microcompartment by Non-native Signal Sequences Is Mediated by a Common Hydrophobic Motif*. J Biol Chem* **290:** 24519-24533.

Jalili, N., and Laxminarayana, K. (2004) A review of atomic force microscopy imaging systems: application to molecular metrology and biological sciences*. Mechatronics* **14:** 907-945.

Johnson, J.E., and Speir, J.A. (1997) Quasi-equivalent viruses: a paradigm for protein assemblies. *J Mol Biol* **269:** 665-675.

Kerfeld, C.A., Heinhorst, S., and Cannon, G.C. (2010) Bacterial microcompartments. *Annu Rev Microbiol* **64:** 391-408.

Kerfeld, C.A., Sawaya, M.R., Tanaka, S., Nguyen, C.V., Phillips, M., Beeby, M., and Yeates, T.O. (2005) Protein structures forming the shell of primitive bacterial organelles. *Science* **309:** 936-938.

Kim, E.Y., and Tullman-Ercek, D. (2014) A rapid flow cytometry assay for the relative quantification of protein encapsulation into bacterial microcompartments. *Biotechnol J* **9:** 348-354.

Kinney, J.N., Axen, S.D., and Kerfeld, C.A. (2011) Comparative analysis of carboxysome shell proteins. *Photosynthesis Res* **109:** 21-32.

Kinney, J.N., Salmeen, A., Cai, F., and Kerfeld, C.A. (2012) Elucidating essential role of conserved carboxysomal protein CcmN reveals common feature of bacterial microcompartment assembly. *J Biol Chem* **287:** 17729-17736.

Klein, M.G., Zwart, P., Bagby, S.C., Cai, F., Chisholm, S.W., Heinhorst, S*., et al.* (2009) Identification and structural analysis of a novel carboxysome shell protein with implications for metabolite transport. *J Mol Biol* **392:** 319-333.

Laemmli, U.K. (1970) Cleavage of structural proteins during the assembly of the head of bacteriophage T4. *Nature* **227:** 680-685.

Lawrence, A.D., Frank, S., Newnham, S., Lee, M.J., Brown, I.R., Xue, W*., et al.* (2014) Solution structure of a bacterial microcompartment targeting peptide and its application in the construction of an ethanol bioreactor. *ACS Synth Biol* **3:** 454-465.

Lawrence, J.G., and Roth, J.R. (1996) Selfish operons: horizontal transfer may drive the evolution of gene clusters. *Genetics* **143:** 1843-1860.

Leegood, R.C. (2007) A welcome diversion from photorespiration. *Nat Biotechnol* **25:** 539-540.

Liu, Y., Jorda, J., Yeates, T.O., and Bobik, T.A. (2015) The PduL phosphotransacylase is used to recycle coenzyme A within the Pdu microcompartment. *J Bacteriol* **14:** :23922-23928.

Liu, Y., Leal, N.A., Sampson, E.M., Johnson, C.L., Havemann, G.D., and Bobik, T.A. (2007) PduL is an evolutionarily distinct phosphotransacylase involved in B_{12}-dependent 1,2-propanediol degradation by *Salmonella enterica* serovar typhimurium LT2. *J Bacteriol* **189:** 1589-1596.

Long, B.M., Badger, M.R., Whitney, S.M., and Price, G.D. (2007) Analysis of carboxysomes from *Synechococcus* PCC7942 reveals multiple Rubisco complexes with carboxysomal proteins CcmM and CcaA. *J Biol Chem* **282:** 29323-29335.

McEwan, J., Veitch, H., and Russell-Jones, G. (1999) Synthesis and biological activity of ribose-5'-carbamate derivatives of vitamin B_{12}. *Bioconjug Chem* **10:** 1131-1136.

Menon, B.B., Dou, Z., Heinhorst, S., Shively, J.M., and Cannon, G.C. (2008) *Halothiobacillus neapolitanus* carboxysomes sequester heterologous and chimeric RubisCO species. *PloS One* **3:** :e3570.

Mori, K., Bando, R., Hieda, N., and Toraya, T. (2004) Identification of a reactivating factor for adenosylcobalamin-dependent ethanolamine ammonia lyase. *J Bacteriol* **186:** 6845-6854.

Obradors, N., Badia, J., Baldoma, L., and Aguilar, J. (1988) Anaerobic metabolism of the L-rhamnose fermentation product 1,2-propanediol in *Salmonella typhimurium. J Bacteriol* **170:** 2159-2162.

Palacios, S., Starai, V.J., and Escalante-Semerena, J.C. (2003) Propionyl coenzyme A is a common intermediate in the 1,2-propanediol and propionate catabolic pathways needed for expression of the *prpBCDE* operon during growth of *Salmonella enterica* on 1,2-propanediol. *J Bacteriol* **185:** 2802-2810.

Pang, A., Liang, M., Prentice, M.B., and Pickersgill, R.W. (2012) Substrate channels revealed in the trimeric *Lactobacillus reuteri* bacterial microcompartment shell protein PduB. *Acta Cryst D* **68:** 1642-1652.

Pang, A., Warren, M.J., and Pickersgill, R.W. (2011) Structure of PduT, a trimeric bacterial microcompartment protein with a 4Fe-4S cluster-binding site. *Acta Cryst D* **67:** 91-96.

Pang, A., Frank, S., Brown, I., Warren, M.J., and Pickersgill, R.W. (2014) Structural insights into higher order assembly and function of the bacterial microcompartment protein PduA. *J Biol Chem* **289:** 22377-22384.

Parsons, J.B., Frank, S., Bhella, D., Liang, M., Prentice, M.B., Mulvihill, D.P., and Warren, M.J. (2010a) Synthesis of empty bacterial microcompartments, directed organelle protein incorporation, and evidence of filament-associated organelle movement. *Mol Cell* **38:** 305-315.

Parsons, J.B., Dinesh, S.D., Deery, E., Leech, H.K., Brindley, A.A., Heldt, D.*, et al.* (2008) Biochemical and structural insights into bacterial organelle form and biogenesis. *J Biol Chem* **283:** 14366-14375.

Parsons, J.B., Lawrence, A.D., McLean, K.J., Munro, A.W., Rigby, S.E., and Warren, M.J. (2010b) Characterisation of PduS, the pdu metabolosome corrin reductase, and evidence of substructural organisation within the bacterial microcompartment. *PLoS One* **5:** e14009.

Payne, K.A., Quezada, C.P., Fisher, K., Dunstan, M.S., Collins, F.A., Sjuts, H.*, et al.* (2014) Reductive dehalogenase structure suggests a mechanism for B12-dependent dehalogenation. *Nature* **517:** 513-516.

Pena, K.L., Castel, S.E., de Araujo, C., Espie, G.S., and Kimber, M.S. (2010) Structural basis of the oxidative activation of the carboxysomal gamma-carbonic anhydrase, CcmM. *Proc Natl Acad Sci U S A* **107:** 2455-2460.

Penrod, J.T., and Roth, J.R. (2006) Conserving a volatile metabolite: a role for carboxysome-like organelles in *Salmonella enterica. J Bacteriol* **188:** 2865-2874.

Price, G.D., and Badger, M.R. (1991) Evidence for the role of carboxysomes in the cyanobacterial CO_2-concentrating mechanism*. Can J Bot* **69:** 963-973.

Price, G.D., and Badger, M.R. (1989a) Expression of Human Carbonic Anhydrase in the Cyanobacterium *Synechococcus* PCC7942 Creates a High CO(2)-Requiring Phenotype : Evidence for a Central Role for Carboxysomes in the CO(2) Concentrating Mechanism*. Plant Physiol* **91:** 505-513.

Price, G.D., and Badger, M.R. (1989b) Isolation and Characterization of High CO(2)-Requiring-Mutants of the Cyanobacterium *Synechococcus* PCC7942 : Two Phenotypes that Accumulate Inorganic Carbon but Are Apparently Unable to Generate CO(2) within the Carboxysome*. Plant Physiol* **91:** 514-525.

Price, G.D., Badger, M.R., Woodger, F.J., and Long, B.M. (2008) Advances in understanding the cyanobacterial CO_2-concentrating-mechanism (CCM): functional components, Ci transporters, diversity, genetic regulation and prospects for engineering into plants*. J Exp Bot* **59:** 1441-1461.

Price, G.D., Coleman, J.R., and Badger, M.R. (1992) Association of Carbonic Anhydrase Activity with Carboxysomes Isolated from the Cyanobacterium *Synechococcus* PCC7942*. Plant Physiol* **100:** 784-793.

Price-Carter, M., Tingey, J., Bobik, T.A., and Roth, J.R. (2001) The alternative electron acceptor tetrathionate supports B_{12}-dependent anaerobic growth of *Salmonella enterica* serovar typhimurium on ethanolamine or 1,2-propanediol*. J Bacteriol* **183:** 2463-2475.

Rae, B.D., Long, B.M., Badger, M.R., and Price, G.D. (2012) Structural determinants of the outer shell of β-carboxysomes in *Synechococcus elongatus* PCC 7942: roles for CcmK2, K3-K4, CcmO, and CcmL*. PloS One* **7:** e43871.

Rae, B.D., Long, B.M., Badger, M.R., and Price, G.D. (2013) Functions, compositions, and evolution of the two types of carboxysomes: polyhedral microcompartments that facilitate CO_2 fixation in cyanobacteria and some proteobacteria*. Microbiol Mol Biol Rev* **77:** 357-379.

Rasband, W. (1997) ImageJ. Bethesda, MD: US National Institutes of Health. http://rsb.info.nih.gov/ij/ (15.02.2016)

Raux, E., Lanois, A., Levillayer, F., Warren, M.J., Brody, E., Rambach, A., and Thermes, C. (1996) Salmonella typhimurium cobalamin (vitamin B_{12}) biosynthetic genes: functional studies in *S. typhimurium* and *Escherichia coli. J Bacteriol* **178:** 753-767.

Raux, E., Schubert, H.L., and Warren, M.J. (2000) Biosynthesis of cobalamin (vitamin B_{12}): a bacterial conundrum*. Cell Mol Life Sci* **57:** 1880-1893.

Ro, D., Paradise, E.M., Ouellet, M., Fisher, K.J., Newman, K.L., Ndungu, J.M.*, et al.* (2006) Production of the antimalarial drug precursor artemisinic acid in engineered yeast*. Nature* **440:** 940-943.

Roberts, E.W., Cai, F., Kerfeld, C.A., Cannon, G.C., and Heinhorst, S. (2012) Isolation and characterization of the *Prochlorococcus* carboxysome reveal the presence of the novel shell protein CsoS1D*. J Bacteriol* **194:** 787-795.

Rondon, M.R., and Escalante-Semerena, J.C. (1992) The *poc* locus is required for 1,2-propanediol-dependent transcription of the cobalamin biosynthetic (*cob*) and propanediol utilization (*pdu*) genes of *Salmonella typhimurium. J Bacteriol* **174:** 2267-2272.

Sagermann, M., Ohtaki, A., and Nikolakakis, K. (2009) Crystal structure of the EutL shell protein of the ethanolamine ammonia lyase microcompartment*. Proc Natl Acad Sci U S A* **106:** 8883-8887.

Samborska, B., and Kimber, M.S. (2012) A dodecameric CcmK2 structure suggests β-carboxysomal shell facets have a double-layered organization*. Structure* **20:** 1353-1362.

Sampson, E.M., and Bobik, T.A. (2008) Microcompartments for B_{12}-dependent 1,2-propanediol degradation provide protection from DNA and cellular damage by a reactive metabolic intermediate*. J Bacteriol* **190:** 2966-2971.

Sander, J.S., Steinacher, M., Loiseau, E., Demirörs, A.F., Zanini, M., Isa, L., and Studart, A.R. (2015) Robust Microcompartments with Hydrophobically Gated Shells*. Langmuir* **31:** 6965-6970.

Schmid, M.F., Paredes, A.M., Khant, H.A., Soyer, F., Aldrich, H.C., Chiu, W., and Shively, J.M. (2006) Structure of *Halothiobacillus neapolitanus* carboxysomes by cryo-electron tomography*. J Mol Biol* **364:** 526-535.

Shively, J.M., Ball, F., Brown, D.H., and Saunders, R.E. (1973) Functional organelles in prokaryotes: polyhedral inclusions (carboxysomes) of *Thiobacillus neapolitanus. Science* **182:** 584-586.

Shively, J.M., Bock, E., Westphal, K., and Cannon, G.C. (1977) Icosahedral inclusions (carboxysomes) of *Nitrobacter agilis. J Bacteriol* **132:** 673-675.

Sinha, S., Cheng, S., Fan, C., and Bobik, T.A. (2012) The PduM protein is a structural component of the microcompartments involved in coenzyme B(12)-dependent 1,2-propanediol degradation by *Salmonella enterica. J Bacteriol* **194:** 1912-1918.

Smeltzer Claudia C., Cannon Michelle J., Pinson Patrick R., Munger John D. Jr., West Frederick G. , and Grissom Charles B. (2001) Synthesis and Characterization of Fluorescent Cobalamin (CobalaFluor) Derivatives for Imaging*. Org Lett* **3:** 799-801.

So, A.K., Espie, G.S., Williams, E.B., Shively, J.M., Heinhorst, S., and Cannon, G.C. (2004) A novel evolutionary lineage of carbonic anhydrase (epsilon class) is a component of the carboxysome shell*. J Bacteriol* **186:** 623-630.

Sweers, K., van der Werf, K., Bennink, M., and Subramaniam, V. (2011) Nanomechanical properties of α-synuclein amyloid fibrils: a comparative study by nanoindentation, harmonic force microscopy, and Peakforce QNM*. Nanoscale Res Lett* **6:** 1-10.

Tanaka, S., Sawaya, M.R., Phillips, M., and Yeates, T.O. (2009) Insights from multiple structures of the shell proteins from the β-carboxysome. *Protein Sci* **18:** 108-120.

Tanaka, S., Kerfeld, C.A., Sawaya, M.R., Cai, F., Heinhorst, S., Cannon, G.C., and Yeates, T.O. (2008) Atomic-level models of the bacterial carboxysome shell. *Science* **319:** 1083-1086.

Tanaka, S., Sawaya, M.R., and Yeates, T.O. (2010) Structure and mechanisms of a protein-based organelle in *Escherichia coli. Science* **327:** 81-84.

Thiennimitr, P., Winter, S.E., Winter, M.G., Xavier, M.N., Tolstikov, V., Huseby, D.L., *et al.* (2011) Intestinal inflammation allows *Salmonella* to use ethanolamine to compete with the microbiota. *Proc Natl Acad Sci U S A* **108:** 17480-17485.

Thompson, M.C., Crowley, C.S., Kopstein, J., Bobik, T.A., and Yeates, T.O. (2014) Structure of a bacterial microcompartment shell protein bound to a cobalamin cofactor. *Acta Cryst F* **70:** 1584-1590.

Tocheva, E.I., Matson, E.G., Cheng, S.N., Chen, W.G., Leadbetter, J.R., and Jensen, G.J. (2014) Structure and expression of propanediol utilization microcompartments in *Acetonema longum. J Bacteriol* **196:** 1651-1658.

Toraya, T. (2000) Radical catalysis of B_{12} enzymes: structure, mechanism, inactivation, and reactivation of diol and glycerol dehydratases. *Cell Mol Life Sci* **57:** 106-127.

Toraya, T., Honda, S., and Fukui, S. (1979) Fermentation of 1,2-propanediol with 1,2-ethanediol by some genera of Enterobacteriaceae, involving coenzyme B_{12}-dependent diol dehydratase. *J Bacteriol* **139:** 39-47.

Towbin, H., Staehelin, T., and Gordon, J. (1979) Electrophoretic transfer of proteins from polyacrylamide gels to nitrocellulose sheets: procedure and some applications. *Proc Natl Acad Sci U S A* **76:** 4350-4354.

Tsoy, O., Ravcheev, D., and Mushegian, A. (2009) Comparative genomics of ethanolamine utilization. *J Bacteriol* **191:** 7157-7164.

Turpin, D.H., Miller, A., and Canvin, D.T. (1984) Carboxysome content of *Synechococcus leopoliensis* (Cyanophyta) in response to inorganic carbon. *J Phycol* **20:** 249-253.

Ushio Kazutoshi, Susumu Honda, Tetsuo Toraya, Saburo Fukui (1982) The mechanism of in situ reactivation of glycerol-inactivated coenzyme B_{12}-dependent enzymes, glycerol dehydratase and diol dehydratase. *J Nutr Sci Vitaminol* **28:** 225-236.

Van Eykelenburg, C. (1980) Ecophysiological studies on *Spirulina platensis* Effect of temperature, light intensity and nitrate concentration on growth and ultrastructure. *Antonie Van Leeuwenhoek* **46:** 113-127.

Wang, J.C., Chen, C., Rayaprolu, V., Mukhopadhyay, S., and Zlotnick, A. (2015) Self-Assembly of an Alphavirus Core-like Particle Is Distinguished by Strong Intersubunit Association Energy and Structural Defects. *Acs Nano* **9:** 8898-8906.

Wheatley, N.M., Gidaniyan, S.D., Liu, Y., Cascio, D., and Yeates, T.O. (2013) Bacterial microcompartment shells of diverse functional types possess pentameric vertex proteins. *Protein Science* **22:** 660-665.

Yeates, T.O., Jorda, J., and Bobik, T.A. (2013) The shells of BMC-type microcompartment organelles in bacteria. *J Mol Microbiol Biotechnol* **23:** 290-299.

Yeates, T.O., Kerfeld, C.A., Heinhorst, S., Cannon, G.C., and Shively, J.M. (2008) Protein-based organelles in bacteria: carboxysomes and related microcompartments. *Nat Rev Microbiol* **6:** 681-691.

Yeates, T.O., Thompson, M.C., and Bobik, T.A. (2011) The protein shells of bacterial microcompartment organelles. *Curr Opin Struct Biol* **21:** 223-231.